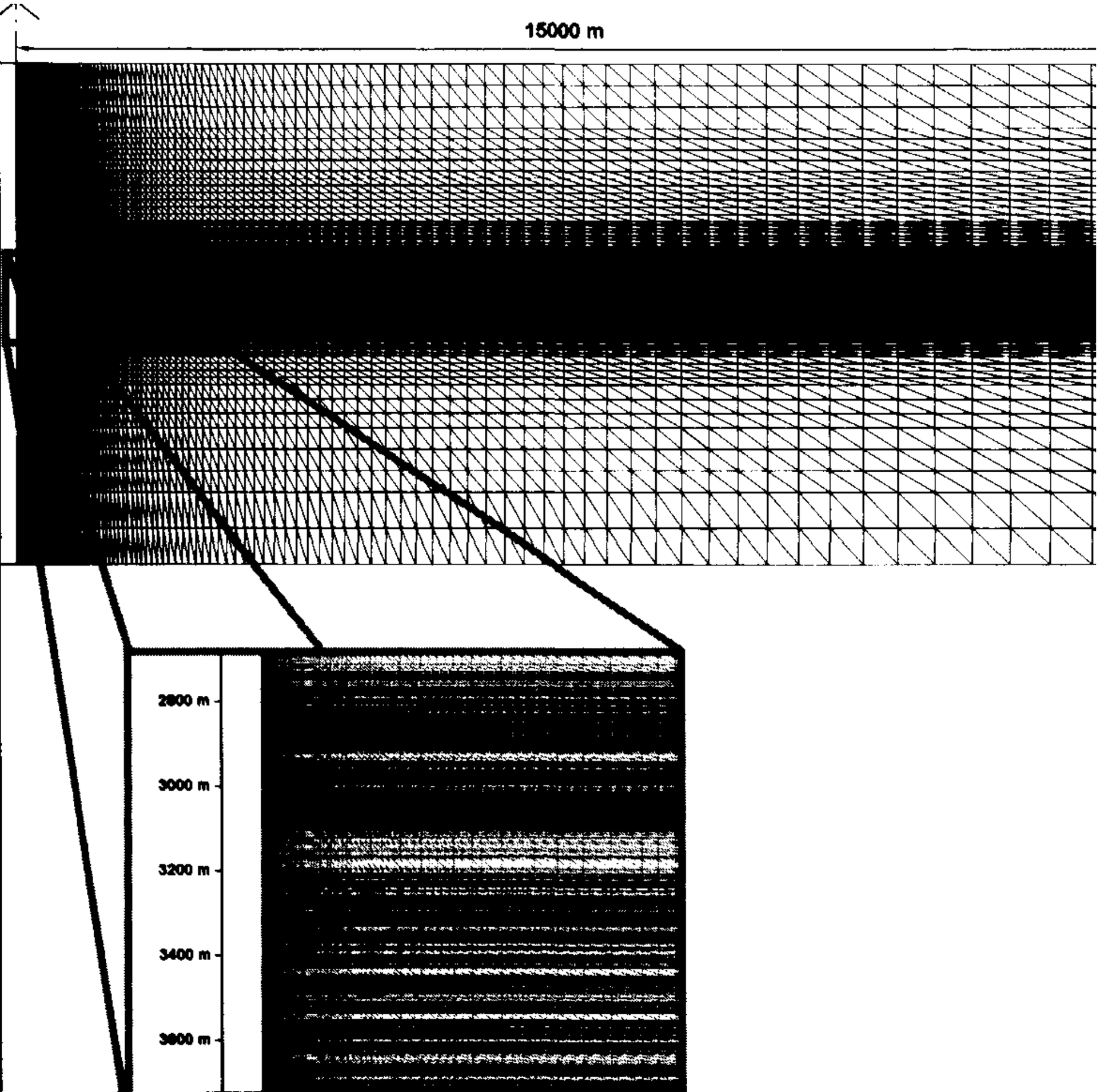
15000 m
2800 m
3000 m
3200 m
3400 m
3600 m

4029
788742
TR4029

ROCK EXPANSION AND COMPACTION AT THE MARKER SCALE IN GAS PRODUCING RESERVOIRS

ROCK EXPANSION AND COMPACTION AT THE MARKER SCALE IN GAS PRODUCING RESERVOIRS

Proefschrift

ter verkrijging van de graad van doctor
aan de Technische Universiteit Delft,
op gezag van de Rector Magnificus prof.dr.ir. J.T. Fokkema,
voorzitter van het College voor Promoties,
in het openbaar te verdedigen

op maandag 24 maart 2003 om 16:00 uur

door

Massimiliano FERRONATO
Dottore in Ingegneria Civile, Università degli Studi di Padova
geboren te Camposampiero, Italia

BIBLIOTHEEK TECHNISCHE UNIVERSITEIT
Promethousplein 1
2628 ZC
DELFT

Dit proefschrift is goedgekeurd door de promotoren:
Prof.dr.ir. A. Verruijt
Prof.dr.ir. G. Gambolati

Samenstelling promotiecommissie:

Rector Magnificus,	voorzitter
Prof.dr.ir. A. Verruijt,	Technische Universiteit Delft, promotor
Prof.dr.ir. G. Gambolati,	Università degli Studi di Padova, Italia, promotor
Prof.dr.ir. F.B.J. Barends,	Technische Universiteit Delft
Prof.dr.ir. S.M. Hassanizadeh,	Technische Universiteit Delft
Prof.ir. C.P.J.W. van Kruijsdijk,	Technische Universiteit Delft
Prof.dr.ir. F. Molenkamp,	Technische Universiteit Delft
Prof.dr. H.A. van der Vorst,	Universiteit Utrecht

Published and distributed by: DUP Science

DUP Science is an imprint of
Delft University Press
P.O. Box 98
2600 MG Delft
The Netherlands
Telephone: +31 15 27 85 678
Telefax: +31 15 27 85 706
E-mail: Info@Library.TUDelft.NL

ISBN 90-407-2392-3

Keywords : Reservoir Engineering, Finite Elements, Iterative Solvers

Copyright ©2003 by M. Ferronato

All rights reserved. No part of the material protected by this copyright notice may be reproduced or utilized in any form or by any means, electronic or mechanical, including photocopying, recording or by any information storage or retrieval system, without written permission from the publisher: Delft University Press.

Printed in The Netherlands

Acknowledgements

This research project has been carried out at the Department of Mathematical Methods and Models for Scientific Applications of the University of Padova with financial support from ENI-Divisione Agip and from the University of Padova project "CO_2 sequestration in geological formations: development of numerical models and simulations of subsurface resrvoirs of the Eastern Po plain".

The PhD thesis has been successfully completed with the constant presence and guidance of both my promotors, prof.dr.ir. Giuseppe Gambolati and prof.dr.ir. Arnold Verruijt. I cannot thank enough prof. Gambolati, who encouraged me, made it possible to pursue the doctoral studies, and helped me with his great scientific expertise. I am proud of working with prof. Verruijt, an eminent scientist and an excellent person. They contributed substantially to my scientific progress and also to my maturation as an individual: thank you very much!

I am very much indebted to all the people who worked with me in Padova during this project: prof.dr. Giorgio Pini, prof.dr.ir. Mario Putti, dr. Annamaria Mazzia, ir. Andrea Comerlati, Andrea Pellizzon, and above all ir. Pietro Teatini and ir. Domenico Baù. Thank you for the useful scientific discussions and for the pleasant time spent together.

I would like to express my gratitude to the Geotechnical Laboratory of Delft University of Technology for contributing to the printing of this thesis. I express also my deepest gratitude to the president and the members of the committe, for agreeing to judge my work and for their useful comments.

Last but absolutely not the least, I dedicate this work to my family, especially to my parents Carlo and Giuseppina, and to my (hopefully!) future wife Samantha. I cannot say anything else but "Grazie!" for unconditionally supporting and encouraging me with their love.

Massimiliano Ferronato

Summary

One of the main difficulties in the accurate prediction of land subsidence due to the exploitation of subsurface fluids is the quality and reliability of the geomechanical data used to represent the field. A most fundamental parameter for the simulation of the porous medium deformation is the vertical uniaxial rock compressibility, which can be determined by monitoring the on-going in situ compaction with the aid of the so-called radioactive marker technique. Successfully implemented in several gas fields all over the world, the radioactive marker technique has been recently used by ENI-Divisione Agip, the Italian national oil company, for a most reliable assessment of rock mechanical properties in the Northern Adriatic basin. However, the outcome of the Northern Adriatic surveys does not frequently allow for a straightforward interpretation because of the unexpected behavior of several markers, which provide expansion rather than compaction, or a deformation although no pore pressure change was measured.

The present work studies the rock deformations at the marker scale induced by the depletion of producing reservoirs in heterogeneous porous media, in order to provide suggestions as to the most correct marker measurement interpretation. The study is carried out with the aid of an original finite element coupled consolidation model.

Chapter 1 provides new results on the numerical issues involved for developing a fast, accurate, and robust mathematical tool. A particular attention is paid to the ill-conditioning caused by the integration in time of consolidation differential equations, and to the applicability of efficient iterative schemes to the problem solution.

The finite element model is used to simulate the expected marker response in the geological and geomechanical setting of the Northern Adriatic basin. The radioactive marker technology and the use of related deformation measurements are reviewed in detail in Chapter 2, which provides also some examples of unexpected data recorded in several Northen Adriatic boreholes. Analytical solutions are used at this stage to gain a first insight into the basic deformation mechanisms in producing reservoirs and in the surrounding medium. Chapter 3 gives a detailed and up-to-date description of the

main geological, mechanical, and hydraulic properties of the Northern Adriatic basin. In particular, an original constitutive model for uniaxial compressibility is derived at the basin scale both in virgin loading and in unloading-reloading conditions.

The numerical study is performed in Chapter 4 and 5. The finite element model is first used to simulate the vertical deformation recorded by an ideal marker tool in a realistic heterogeneous setting. This study gives indications as to the main factors influencing the marker response, the layering configurations which are most likely to provide useful data, and the theoretical marker reliability for the compressibility estimate. Then, the behavior recorded by radioactive markers in three deep boreholes of the Northern Adriatic is simulated numerically. It is shown that the model can reproduce satisfactorily several records, providing suggestions for a more efficient marker installation and supporting the reliability of the proposed basin-scale constitutive law derived in the study area.

M. Ferronato, Rock Expansion and Compaction at the Marker Scale in Gas Producing Reservoirs, PhD Thesis, Delft University of Technology, 2003.

Contents

Acknowledgements I

Summary III

Introduction 1

1 FE solution to coupled consolidation equations 7

1.1 Introduction 7

1.2 Theory overview 9

1.3 Ill-conditioning of the coupled system 13

1.3.1 Numerical examples 16

1.4 Solution by Conjugate Gradient like methods 20

1.4.1 Nodal ordering 22

1.4.2 Preconditioning techniques 23

1.4.3 Scaling algorithms 25

1.5 Conclusions 29

2 Deformation monitoring of productive gas/oil reservoirs 31

2.1 Introduction 31

2.2 The radioactive marker technique 33

2.2.1 Uniaxial compressibility from marker measurements 37

2.2.2 Deformation monitoring in the Northern Adriatic basin, Italy . . . 39

2.3 Productive reservoir compaction 44

2.4 Conclusions 47

3 The Northern Adriatic basin, Italy 51

3.1 Introduction 51

3.2 Geological setting and petroleum occurrence 54

3.2.1 Well litho-stratigraphic sequencing by electrofacies 56
3.3 Constitutive equations 59
3.3.1 Virgin load conditions 60
3.3.2 Unloading-reloading conditions 64
3.3.3 Biot coefficient 68
3.4 Hydraulic properties 68
3.5 Conclusions 72

4 Marker response in heterogeneous reservoirs **75**
4.1 Introduction 75
4.2 Finite Element numerical model 77
4.2.1 Axi-symmetric setting 78
4.2.2 Withdrawal distribution 83
4.2.3 FE mesh and boundary conditions 84
4.3 Flow, strain and stress fields 87
4.4 Simulated marker response 92
4.4.1 Critical situations for marker measurements 98
4.5 Conclusions 101

5 Marker interpretation in the Northern Adriatic **103**
5.1 Introduction 103
5.2 Application to the Northern Adriatic boreholes 105
5.2.1 Well 1 107
5.2.2 Well 2 114
5.2.3 Well 3 121
5.3 Conclusions 126

Bibliography **129**

Samenvatting (Summary in Dutch) **141**

Sommario (Summary in Italian) **143**

Curriculum Vitae **145**

List of Figures

1 Map of the Mediterranean Sea. The location of the Northern Adriatic basin is indicated by the panel. 3

1.1 Qualitative behavior of left-hand side R_l and right-hand side R_r of eq. (1.16) vs. Δt and $\psi = \phi\beta E$. 14

1.2 Schematic representation of the stratified porous medium used as test problem 16

1.3 (a) L vs Δt and (b) D vs Δt for $k_{\text{sand}} = 10^{-5}$ m/s, $k_{\text{clay}} = 10^{-8}$ m/s, $\Omega = 312.5$ m^2, and variable E. 17

1.4 (a) L vs Δt and (b) D vs Δt for $E = 8.16 \cdot 10^1$ MPa, $\Omega = 312.5$ m^2, and variable k_{sand} and k_{clay}. 18

1.5 L vs Δt for $E = 8.16 \cdot 10^1$ MPa, $k_{\text{sand}} = 10^{-5}$ m/s, $k_{\text{clay}} = 10^{-8}$ m/s, and variable Ω. 18

1.6 L vs Δt for $E = 8.16 \cdot 10^3$ MPa, $k_{\text{sand}} = 10^{-7}$ m/s, $k_{\text{clay}} = 10^{-10}$ m/s, $\Omega = 5000$ m^2 (dotted profile) and $E = 8.16 \cdot 10^1$ MPa, $k_{\text{sand}} = 10^{-5}$ m/s, $k_{\text{clay}} = 10^{-8}$ m/s, $\Omega = 5000$ m^2 (solid profile). 19

1.7 The Bi-CGSTAB algorithm. 21

1.8 Sparsity structure of the matrix $\mathbf{A}_{\Delta t}$ with (a) the ordering suggested by (1.15), and (b) the nested ordering $(\delta_{x_1}, \delta_{y_1}, \delta_{z_1}, p_1, \delta_{x_2}, \delta_{y_2}, \delta_{z_2}, p_2, \ldots)$. The grayscale indicates the magnitude of each element. 22

1.9 Bi-CGSTAB convergence profiles with different preconditioners for $\Omega = 312.5$ m^2, $k_{\text{sand}} = 10^{-5}$ m/s, $k_{\text{clay}} = 10^{-8}$ m/s, and (a) $E = 8.16 \cdot 10^2$ MPa, $\Delta t = 1$ s; (b) $E = 8.16 \cdot 10^1$ MPa, $\Delta t = 10^2$ s. 24

1.10 Bi-CGSTAB convergence profiles with different preconditioners for $\Omega = 5000$ m^2, $k_{\text{sand}} = 10^{-7}$ m/s, $k_{\text{clay}} = 10^{-10}$ m/s, $E = 8.16 \cdot 10^3$ MPa, and $\Delta t = 1$ s. 26

1.11 Bi-CGSTAB preconditioned by ILUT(25,10^{-3}) convergence profiles with different preliminary scalings for $\Omega = 312.5$ m^2, $k_{\text{sand}} = 10^{-5}$ m/s, $k_{\text{clay}} = 10^{-8}$ m/s, and (a) $E = 8.16 \cdot 10^2$ MPa, $\Delta t = 1$ s; (b) $E = 8.16 \cdot 10^1$ MPa, $\Delta t = 10^2$ s. 28

2.1 Schematic representation of the radioactive marker technique. 34
2.2 (a) Schematic representation of a 4-detector logging tool; (b) $\gamma-$ray signal recording by detectors 1, 2, 3, and 4; (c) tool dimensions. 36
2.3 Marker measurements referred to the midpoint of each interval for (a) well 1, 1992-1996; (b) well 2, 1994-1996; (c) well 3, 1996-1999. Gray shaded areas correspond to the productive units. 43
2.4 Double Geertsma solution for a compacting disc-shaped reservoir with $s/R \ll 1$ over the center of the field: (a) normalized vertical displacement; (b) normalized vertical strain outside the reservoir. 47
2.5 Vertical strain $\epsilon_z^{(o)}$ induced by a simultaneous unit pore pressure decline in two reservoirs located at $c = 980$ m and $c = 1020$ m, respectively. 48

3.1 Map of the Northen Adriatic basin, showing the trace of some major gas fields discovered in this area, together with the location of marker boreholes and the leveling and GPS networks established for land subsidence monitoring. 52
3.2 The Po River plain and Northern Adriatic basin with the location of gas/oil fields. 54
3.3 (a) Off-shore and (b) on-shore structural cross-section of the Northern Adriatic basin (after Anelli *et al.* [1996]). Section lines are shown in Figure 3.2. 55
3.4 Litho-stratigraphic sequencing by electrofacies of a representative portion of well 1 as obtained from SHDT well-logs. The length of bars in the far right-hand column is related to lithotype permeability. 57
3.5 Same as in Figure 3.4, for well 2. 58
3.6 Same as in Figures 3.4 and 3.5, for well 3. 59
3.7 Constitutive law of uniaxial compressibility c_M in virgin loading conditions selected for the Northern Adriatic sediments. Confidence intervals and c_M values used for regression are also shown. 63
3.8 Marker measurements referred to the midpoint of each interval for well 1, 1997-1999. 66
3.9 The same as Figure 3.7 for unloading-reloading conditions. 67

3.10 Ratio between virgin loading and unloading-reloading compressibility using the constitutive laws (3.13) and (3.14). 67
3.11 Biot coefficient α vs depth in undisturbed conditions. 69
3.12 Sample layered formation for the equivalent horizontal and vertical permeability estimate. 71

4.1 Pumping rate used in the numerical simulations. The value Q^* is calibrated in each scenario to obtain an average 10 MPa pore pressure decline in the depleted volume after n years of production. 84
4.2 Detailed litho-stratigraphy used in the SD and CL configurations in the 3200-3400 m depth range. The reservoir burial depth is approximately 3300 m. The cumulative thickness of the producing layers is 13 and 4 m, respectively. The estimated intrinsic permeability of each lithotype is indicated in the legend. 85
4.3 Vertical cross-section of the FE mesh used in the simulations. 86
4.4 Convergence profiles obtained with preconditioned Bi-CGSTAB and LSL preliminary scaling in a few representative simulations for different time steps. 87
4.5 Pore pressure variation relative to the maximum pore pressure decline after two years of pumping: (a) SD scenario with volume sink; (b) SD scenario with line sink; (c) CL scenario with volume sink; (d) CL scenario with line sink. Litho-stratigraphies (clays are shaded gray) and the depleted layers (hatched areas) are also shown. 88
4.6 Vertical strain relative to the maximum value after two years of pumping: (a) SD scenario with volume sink; (b) SD scenario with line sink; (c) CL scenario with volume sink; (d) CL scenario with line sink. Litho-stratigraphies (clays are shaded gray) and the depleted layers (hatched areas) are also shown. 90
4.7 (a) q and (b) ϵ vs p' for depleted rock layers; (c) q and (d) ϵ vs p' for porous medium surrounding the depleted layers. 91
4.8 Simulated marker response (from eq. (4.20)) vs depth at different times in the SD scenario with: (a) volume sink; (b) line sink. The litho-stratigraphy is also shown. Compactions and expansions are depicted using different scales. 93
4.9 The same as Figure 4.8 for the CL scenario. 94

4.10 Sensitivity analysis in relation to rock compressibility: (a) SD scenario with volume sink; (b) SD scenario with line sink; (c) CL scenario with volume sink; (d) CL scenario with line sink. Marker response is simulated two years after starting production. 95
4.11 The same as Figure 4.10 for shale permeability. 96
4.12 The same as Figures 4.10 and 4.11 for the Biot coefficient. 97
4.13 Simulated marker response vs depth in the CL scenario with line sink, $k_{cl} = k_{cl0}/10^4$, and: (a) 1 depleted layer; (b) 2 depleted layers. 99
4.14 "A posteriori" c_M estimate using the simulated marker response and pore pressure drawdown in: (a) SD scenario; (b) CL scenario. 100

5.1 Stratigraphic discretization used in the FE model with the class ID number given in Table 5.2. Productive units are indicated by the dashed layers. . . 108
5.2 Cross-section of the FE mesh used to reproduce the in-situ deformations in well 1. 109
5.3 Well 1: representative convergence profiles obtained for: (a) $\Delta t = 10$ days, 1992-1996 simulation, and different scenarios; (b) $\Delta t = 20$ days, 1997-1999 simulation, and different scenarios. 112
5.4 Well 1: comparison between the radioactive marker measurements and the model's results for the period 1992-1996. 113
5.5 Well 1: the same as Figure 5.4 for the period 1997-1999. 115
5.6 Stratigraphic discretization used in the FE model with the class ID number provided in Table 5.4. Productive units are indicated by the dashed layers. 116
5.7 Cross-section of the FE mesh used to reproduce the in-situ deformations in well 2. 117
5.8 Well 2: representative convergence profiles obtained for $\Delta t = 10$ days and different scenarios. 119
5.9 Well 2: comparison between radioactive marker measurements and the model's results computed using the compressibility law (3.13) for the period 1994-1996. 120
5.10 Well 2: the same as in Figure 5.9 locally doubling the compressibility provided by equation (3.13). 120
5.11 Stratigraphic discretization used in the FE model with the class ID number given in Table 5.6. Productive units are indicated by the dashed layers. . . 122

5.12 Cross-section of the FE mesh used to reproduce the in-situ deformations in well 3. 123
5.13 Well 3: representative convergence profiles obtained for $\Delta t = 20$ days and different scenarios. 124
5.14 Well 3: comparison between the radioactive marker measurements and the model's results for the period 1996-1999. 125
5.15 Well 3: the same as in Figure 5.14 with the model's results calculated with the effective spacing length. 126

List of Tables

1.1 CPU times (s) for computing the preconditioner (T_p) and achieving the convergence (T_c) in case (a) and (b). T_t is the total CPU time ($= T_p + T_c$). 25

1.2 CPU times (s) for computing the preconditioner (T_p) and achieving the convergence (T_c) in case (c). T_t is the total CPU time ($= T_p + T_c$). 26

1.3 CPU times (s) for the matrix scaling (T_s), computing the preconditioner ILUT(25,10^{-3}) (T_p), and achieving the convergence (T_c) in case (a) and (b). T_t is the total CPU time ($= T_s + T_p + T_c$). 28

2.1 Marker measurements and corresponding pore pressure variation in well 1 during the period 1992-1996. 40

2.2 Marker measurements and corresponding pore pressure variation in well 2 during the period 1994-1996. 41

2.3 Marker measurements and corresponding pore pressure variation in well 3 during the period 1996-1999. 42

3.1 Marker measurements and corresponding pore pressure variations in well 1 during 1997-1999. n.a. = not available. 65

3.2 Pore pressure change and marker measurements for the spacings in well 1 where a pore pressure recovery was observed after 1996. 66

5.1 Permeability and porosity of additional lithotypes used in the FE model of the litho-stratigraphic sequence above and below the depth interval monitored by electrofacies. 106

5.2 Lithotype permeability and porosity used in the FE model of the litho-stratigraphic sequence in well 1. The ID number is the same as in Figure 5.1. 107

5.3 Static reservoir pore pressure values in well 1 before starting production and at each marker logging time. The pore pressure variations over the monitored periods are given in the far right-hand columns. n.a. = not available. 110
5.4 Lithotype permeability and porosity used in the FE model of the litho-stratigraphic sequence in well 2. The ID number is the same as in Figure 5.6. 115
5.5 Static reservoir pore pressure values in well 2 at each marker logging time. The pore pressure variations in the monitored period are given in the far right-hand column. 118
5.6 Lithotype permeability and porosity used in the FE model of the litho-stratigraphic sequence in well 3. The ID number is the same as in Figure 5.11. 121
5.7 Static reservoir pore pressure values in well 3 at each marker logging time. The pore pressure variations in the monitored period are provided in the far right-hand column. 124

Introduction

It is well understood and universally recognized that the exploitation of subsurface fluids, such as water, oil, or natural gas, from basins filled with unconsolidated deposits, is a major cause for land subsidence of anthropogenic origin. The impact of this occurrence, on the environment and man-made structures as well, is a matter of great concern worldwide, irrespective of the fluid withdrawn. As an example, in lowlying coastal areas the loss in ground elevation can enhance sea water encroachment both occasionally during severe storm events and permanently, e.g. Colazas and Strehle [1995]; Finol and Sancevic [1995]; Gambolati *et al.* [1999a]; Baù *at al.* [2000a]; Larson *et al.* [2001], with an adverse impact on the environment associated with large economical and social costs. Furthermore, the subsurface fluid development may induce structural damages to off-shore platforms [Zaman *et al.*, 1995] and to shallow foundations, especially in case of a non-uniform lowering of the groundwater table and inhomogeneous soil properties [Verruijt and Brinkgreve, 2000]. Minor, but nevertheless important, operational problems related to the field deformation may also be concerned with the break of well casings [Fredrich *et al.*, 2000], the decrease of formation porosity and permeability [Ruistuen *et al.*, 1999], and the consequent reduction of the field production life [Macini and Mesini, 1998].

Since the field compaction does not simply migrate in its integrity to the ground surface, generally bi-dimensional or three-dimensional numerical models are needed to predict the porous medium deformation during the field production life and also after the field abandonment. The basis for the simulation of land subsidence due to fluid withdrawal is the theory of consolidation [Terzaghi, 1925], which describes the effect of pore water dissipation upon the deformations of a saturated soil. The extension towards the three-dimensional setting was given by Biot [1941], who assumed that the soil behaves as a perfectly elastic material. However, because of the mathematical complexity of Biot's poroelasticity theory, some simplifying assumptions were necessary to address real applications, leading to the so-called uncoupled approach in which Biot's theory basically reduces to Jacob's [1950] theory. The uncoupled poroelasticity equations were

solved by Geertsma [1966, 1973a,b] for the problem of a disc-shaped reservoir subject to a uniform pore pressure decline. Almost simultaneously, the development of the Finite Element method [Zienkiewicz, 1971] and the increasing availability of larger computational resources brought to the solution to poroelastic problems by numerical techniques and to pioneering applications of computer models to the real field, e.g. Gambolati and Freeze [1973]; Gambolati *et al.* [1974]. Since then, the use of finite elements in poroelasticity has become increasingly popular, such that nowadays it is considered to be a quite common procedure. At present the continuous improvement of computer technology allows for the solution to increasingly large size and very sophisticated mathematical models, requiring high computational effort and efficiency.

However, the success of a mathematical model in providing an accurate prediction of anthropogenic land settlement largely depends on the quality and reliability of the hydrogeological and geomechanical data used to represent the field and the surrounding porous medium. A most fundamental parameter for a reliable simulation is the vertical uniaxial rock compressibility c_M, which basically controls the amount of compaction caused by the pore pressure drawdown in the depleted formation [Johnson *et al.*, 1989; Ruddy *et al.*, 1989; Gambolati *et al.*, 1999b]. Parameter c_M can be determined in the laboratory on rock samples taken from exploratory boreholes drilled at the field burial depth and subjected to triaxial and/or oedometric tests. Some concern, however, may arise in upscaling over the field scale the data obtained from samples with a few centimeter size, especially in heterogenous sedimentary basins, in addition to possible errors due to the specimen disturbance during core sampling and in the preparation process [Jardine *et al.*, 1984; Van Hasselt, 1992; Kim *et al.*, 1994].

A promising technique for a most realistic evaluation of the rock compressibility c_M over the field scale relies on the monitoring of the on-going in situ compaction during the field production life, especially at the early stage of production. For shallow formations down to 500 m, as is typically the case of water table and confined aquifers used for groundwater pumping, the extensometers can contribute to effectively measure the porous system compaction [Heywood, 1995]. For deeper gas/oil reservoirs the radioactive marker technique can be used. Originally developed 30 years ago [De Loos, 1973], the marker records allow for a theoretically straightforward rock mechanical characterization by relating the depleted formation compaction to the corresponding pore pressure drawdown, thus providing an in situ evaluation of the elastic properties of the porous medium. Recently, the radioactive marker technique has been successfully implemented in several gas fields, such as for example in the North Sea [Menghini, 1989], the Netherlands [Mobach

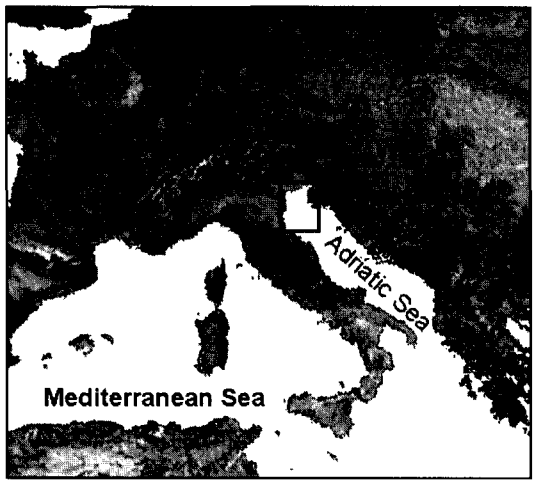

Figure 1: Map of the Mediterranean Sea. The location of the Northern Adriatic basin is indicated by the panel.

and Gussinklo, 1994], and the Gulf of Mexico [De Kock *et al.*, 1998]. A quite common result of these surveys is the discrepancy between laboratory and in situ c_M estimate, with the latter usually smaller (sometimes up to one order of magnitude) than the former. Several explanations have recently been advanced, for instance taking into account the original field stress path and the so-called aging effect [Clayton and Khatrush, 1986; Hueckel *et al.*, 2001], but the debate is still underway.

Since 1992, ENI-Divisione Agip, the Italian national oil company, has implemented the radioactive marker technique in several off-shore boreholes of the Northern Adriatic basin (Figure 1), in order to monitor the on-going compaction of producing gas reservoirs and derive a most reliable assessment of the rock geomechanical parameters at the field scale to be used by numerical models for land settlement prediction. However, the outcome of the Northern Adriatic surveys does nor frequently allow for a straightforward interpretation and derivation of the rock uniaxial compressibility. To some extent unexpectedly, several marker spacings exhibited expansion rather than compaction even though the pore pressure in the corresponding units has supposedly decreased, whereas other marker intervals indicate a deformation although no pore pressure change has been measured. Hence, a deeper investigation appears to be needed in order to better understand the origin and the significance of such measurements, as well as to provide indications as to their actual reliability.

The analysis of local rock deformations induced by reservoir compaction in an inhomogeneous porous medium can be performed with the aid of an appropriate numerical model based on Biot's three-dimensional consolidation theory. The use of a finite element coupled consolidation model, however, is not straightforward, especially in a complex geological setting with frequently alternating lithologies, and when the early transient solution may be very important. As experienced by several authors as well, e.g. Ghaboussi and Wilson [1973]; Reed [1984]; Sloan and Abbo [1999]; Ferronato *et al.* [2001], the coupled model can prove quite difficult to solve from a computational viewpoint since the numerical solution may suffer from instabilities [Booker and Small, 1975] and inaccuracies [Vermeer and Verruijt, 1981] depending on the porous system properties and the magnitude of the time step used in the time integration. Moreover, the large model size usually required by the detailed litho-stratigraphy suggests using efficient linear system solvers so as to improve, as much as possible, the computer code performance, without degrading the solution accuracy. The major classes of ad hoc solvers for coupled problems currently available are three: direct, partitioned, and projection solvers. Despite its relatively old age, the direct solution approach is still widely used for the solution to coupled consolidation, e.g. Lewis and Schrefler [1998]. For a thorough review of recent developments, see Duff *et al.* [1986]. The appeal of the direct approach stems from a number of factors, such as the nice property of requiring a preset number of operations which only depends on the matrix structure and the availability of public domain libraries, e.g. the Harwell Software Library [HSL, 2000], which offer robust and efficient routines designed to address practically any kind of problems. Disadvantages, however, may arise from the usually large core memory requirement, which makes the direct solver not so attractive for sparse linear systems. The partitioned approach is specifically designed for coupled problems and its basic idea relies on the uncoupling the overall model into smaller symmetric positive definite sub-models and (possibly, not necessarily) iterating between the decoupled solutions. The main contributions to this area are due to Park and Felippa [1983], with a recent cost-effective implementation of the partitioned scheme provided by Prevost [1998]. The partitioned solution allows for a significant core memory saving as compared to the direct methods, but the algorithm can be only conditionally stable, thus requiring an additional cost to perform appropriate stabilization procedures, e.g. Zienkiewicz *et al.* [1988]. Finally, the class of iterative solvers relying on accelerated conjugate gradients for unsymmetric indefinite equations is becoming increasingly popular, because of its computational efficiency and robustness. A comprehensive review of unsymmetric projection methods can be found in Saad [1996]. Recent analyses of conjugate gradient-like methods

in finite element consolidation models have been contributed by Gambolati *et al.* [2002], showing their overall superiority to the other mentioned approaches in several examples.

The main objective of the present work is to study the rock deformations at the marker scale induced by the depletion of producing reservoirs embedded in heterogeneous porous media, in order to provide suggestions as to the most correct marker measurement interpretation. The study is carried out with the aid of a finite element coupled consolidation model implemented at the Department of Mathematical Methods and Models for Scientific Applications of the University of Padova by the Author and the research group headed by Prof. Giuseppe Gambolati. Because of the difficulties in the solution to finite element consolidation models discussed above, the numerical issues for developing a robust, efficient, and accurate mathematical tool have played an important role in the present study. The finite element model is then used to simulate the expected marker response in the geological and geomechanical setting of the Northern Adriatic basin. The analysis addresses the porous medium deformation at the marker scale providing an insight into the layering configurations which are most likely to yield non-representative data. In particular, the possible marker expansions are investigated in relation to a stratified reservoir with interbedded low permeable confining formations. Finally, the finite element model is used to reproduce the marker measurements actually recorded by ENI-Divisione Agip in some Northern Adriatic monitoring boreholes. This allows for a set of remarks as to the measured deformation reliability for the evaluation of the rock uniaxial compressibility, and helps derive a number of indications for the most appropriate implementation of radioactive markersin the field.

The thesis is organized in five chapters, as follows:

chapter 1: the finite element approach to Biot's consolidation equations is reviewed and new results are provided in order to allow for a fast, accurate, and robust solution to the coupled system. An empirical criterion for the critical time step causing ill-conditioning is developed and an efficient solution strategy proposed, based on appropriate preliminary scaling and Bi-CGSTAB preconditioned with an incomplete partial factorization;

chapter 2: the radioactive marker technology and the use of marker data to estimate the rock uniaxial compressibility are reviewed in detail. The outcome of surveys performed by ENI-Divisione Agip in the Northern Adriatic boreholes are presented and discussed, emphasizing the difficult interpretation of several marker deformations. Analytical solutions are used to gain an insight into a few basic deformation

mechanisms in producing reservoirs;

chapter 3: the study area, i.e. the Northern Adriatic basin, is presented with a detailed and up-to-date description of its main geological, mechanical, and hydraulic properties. Several typical litho-stratigraphic sequences obtained from electrofacies are described and an original constitutive model, based on in situ amrker records, is derived at the basin scale both in virgin loading and unloading-reloading conditions. The available hydraulic properties are reviewed with the description of a homogenization procedure yielding equivalent hydraulic conductivities over units obtained from the clustering of very thin layers;

chapter 4: a numerical study is performed to simulate by a finite element coupled consolidation model the vertical deformation recorded by an ideal marker tool in heterogeneous producing reservoirs. The sensitivity of a marker response is investigated in relation to litho-stratigraphy, compressibility, permeability, Biot coefficient, and the respective position of monitoring and pumping wells. The results provide also some indications as to the theoretical marker reliability for the c_M estimate;

chapter 5: a set of radioactive marker measurements, made by ENI-Divisione Agip over the last decade in three deep boreholes of the Northern Adriatic basin, is simulated numerically. It is shown that the model can reproduce satisfactorily several records and can provide suggestions for a more efficient marker installation. Some indications are finally given on the reliability of the proposed basin-scale constitutive law derived for c_M in the study area.

Chapter 1

Finite element solution to coupled consolidation equations

Although nowadays the Finite Element (FE) implementation of coupled consolidation models can be considered a quite common practice, nevertheless the solution may still be difficult, because the global matrix generated in a coupled problem often suffers from ill-conditioning and has typically a large size. The present chapter provides a review of recent results obtained at the Department of Mathematical Models and Methods for Scientific Application (DMMMSA) of the University of Padova by the Author and the research team headed by Prof. Giuseppe Gambolati. These results concern the main causes of ill-conditioning, providing an empirical criterion for a lower bound Δt_{crit} of the time integration step below which ill-conditioning may occur. A solution strategy is presented and discussed, based on preconditioned conjugate gradient-like solvers and preliminary scaling algorithms, which allows for an accurate, robust, and efficient solution to large size coupled consolidation models. It is also shown that the symmetry of the system is not necessary to improve the computer code performance.

1.1 Introduction

The consolidation process is basically due to the pore water pressure dissipation in a saturated soil, which induces a deformation of the porous medium. The consolidation theory was first developed in a one-dimensional setting by Terzaghi [1925] and later extended to three-dimensional media by Biot [1941], giving rise to a system of PDEs that combines the elastic equilibrium of the porous body with the continuity of ground water flow.

Because of the mathematical complexity of Biot's consolidation theory, analytical solutions are possible only for simple problems with a symmetric configuration, e.g. Verruijt [1969], while for more complicated realistic situations numerical techniques must be used. Since the early '70s FE solutions to the coupled Biot's equations have been developed [Sandhu and Wilson, 1969; Christian and Boehmer, 1970; Hwang *et al.*, 1971; Desai, 1975; Verruijt, 1977] and at present the implementation of a FE model can be considered a quite common practice. Nevertheless, the solution to realistic FE consolidation models may still be very difficult, particularly because the resulting linear system can be ill-conditioned, especially for small time steps, and has typically a large size, thus requiring significant computational costs and efforts.

It is generally understood that in the early stage of consolidation, when excess pore water pressure gradients are usually high, small time integration steps are necessary in order to obtain an accurate solution. Vermeer and Verruijt [1981] derived a lower bound for the time step below which spatial oscillations in the numerical solution may occur, depending on the FE mesh resolution and on the consolidation coefficient. Ill-conditioning of the resulting system has been addressed by several other authors [Ghaboussi and Wilson, 1973; Reed, 1984; Sloan and Abbo, 1999; Chan *et al.*, 2001] and recently Ferronato *et al.* [2001] have shown that a critical time step yielding ill-conditioning can be defined, which is very similar, although with different meaning, to Vermeer and Verruijt's [1981] time step limit. Under such critical conditions, an accurate FE solution to the coupled consolidation problem may prove difficult to achieve, independent of the solution strategy used.

A major computational effort in the FE integration of a realistic model is related to the large size of the discrete system, e.g. Gambolati *et al.* [2000]; Baù *et al.* [2001]. Direct solvers are still widely used and sophisticated variants [Duff *et al.*, 1986] may prove efficient for sparse indefinite matrices, although the core memory requirement remains large. Other much studied methods are based on a staggered implementation wherein the overall coupled model is partitioned into two smaller symmetric positive definite systems, with the pore pressure projected from time t to time $t + \Delta t$ by the use of an ad hoc predictor, and the problem solved separately for the nodal displacements [Park and Felippa, 1983]. Unfortunately, depending on the nature of the predictor the staggered algorithm can be conditionally stable, and stabilization procedures, e.g. Park [1983]; Zienkiewicz *et al.* [1988], must be developed to obtain unconditional stability, thus requiring an additional computational cost. Recently, a growing attention has been devoted to a new class of iterative solvers based on preconditioned conjugate gradients (CG) for the solu-

tion of unsymmetric indefinite equations (for a thorough review, see Saad [1996]). The main advantages of the CG approach stem from the high computational efficiency, the much reduced core memory requirement, and the ease of implementation in a parallel environment, which represent very important issues for the solution to large size problems. One of the most popular CG-like algorithms is the bi-conjugate gradient stabilized (Bi-CGSTAB [Van der Vorst, 1992]), the performance of which in FE consolidation models has been demonstrated and extensively experimented by Gambolati *et al.* [2001b, 2002].

The present chapter reviews some of the issues related to the FE solution to the coupled consolidation equations and shows possible remediations for difficult problems. The FE integration of Biot's equations is briefly recalled and the main causes of possible ill-conditioning analyzed. The empirical criterion for the critical time step derived by Ferronato *et al.* [2001] is discussed and compared with the accuracy condition by Vermeer and Verruijt [1981]. Then the use of CG-like projection solvers in consolidation models is investigated, with a special attention to the numbering of the unknowns, preconditioning, and scaling strategies which can strongly impact on the solver convergence. Finally a set of conclusive remarks and recommendations is provided.

1.2 Theory overview

The distribution of stresses and pore pressures in a saturated porous body during consolidation is governed by the principle of effective stress, equilibrium and the continuity of flow. If $\hat{\boldsymbol{\sigma}}^T = [\hat{\sigma}_{xx}, \hat{\sigma}_{yy}, \hat{\sigma}_{zz}, \hat{\sigma}_{xy}, \hat{\sigma}_{yz}, \hat{\sigma}_{zx}]$ and p denote the vector of total stress components and pore pressure, respectively, Terzaghi's effective stress principle [Terzaghi and Peck, 1967] reads:

$$\hat{\boldsymbol{\sigma}} = \boldsymbol{\sigma} - \mathbf{i}p \tag{1.1}$$

where $\boldsymbol{\sigma}^T = [\sigma_{xx}, \sigma_{yy}, \sigma_{zz}, \sigma_{xy}, \sigma_{yz}, \sigma_{zx}]$ is the vector of effective stresses, $\mathbf{i}^T = [1, 1, 1, 0, 0, 0]$ is the Kronecker δ in vectorial form, and tensile stresses and pore pressures are taken as positive.

Since the medium is in equilibrium, the virtual work principle applies to the whole system:

$$\int_V \boldsymbol{\epsilon}^T \hat{\boldsymbol{\sigma}} dV = \int_\Sigma \mathbf{u}^T \hat{\mathbf{t}} d\Sigma \tag{1.2}$$

with $\boldsymbol{\epsilon}^T = [\epsilon_x, \epsilon_y, \epsilon_z, \gamma_{xy}, \gamma_{yz}, \gamma_{zx}]$ the strain component vector, $\mathbf{u}^T = [u_x, u_y, u_z]$ the displacements and $\hat{\mathbf{t}}$ the total external forces acting per unit surface. V represents the body

volume with Σ its boundary. Using equation (1.1), equation (1.2) becomes:

$$\int_V \boldsymbol{\epsilon}^T \boldsymbol{\sigma} dV - \int_V \boldsymbol{\epsilon}^T \mathbf{i} p dV = \int_\Sigma \mathbf{u}^T \hat{\mathbf{t}} d\Sigma \tag{1.3}$$

For a generic n-node element discretization, displacements and pore pressures can be written as [Zienkiewicz, 1991]:

$$\mathbf{u} = \mathbf{N}_u \boldsymbol{\delta} \tag{1.4}$$

$$p = \mathbf{N}_p \mathbf{p} \tag{1.5}$$

where $\boldsymbol{\delta}$ and $\mathbf{p}$ are the nodal component vectors, and

$$\mathbf{N}_u = [N_i \mathbf{I}_3] \qquad i = 1, \ldots, n$$

$$\mathbf{N}_p = [N_i \mathbf{I}_1] \qquad i = 1, \ldots, n$$

are the matrices of shape functions N_i, with $\mathbf{I}_m$ the m^{th} order identity matrix. The effective stress is related to the strain vector through the elastic matrix $\mathbf{D}$:

$$\boldsymbol{\sigma} = \mathbf{D}\boldsymbol{\epsilon} \tag{1.6}$$

and strains depend upon the nodal displacements according to:

$$\boldsymbol{\epsilon} = \mathbf{L}\mathbf{u} = \mathbf{L}\mathbf{N}_u \boldsymbol{\delta} = \mathbf{B}\boldsymbol{\delta} \tag{1.7}$$

with $\mathbf{L}$ an appropriate first-order differential operator. Replacing equations (1.4) through (1.7) into equation (1.3), and canceling the virtual displacements, yield the FE formulation of the elastic equilibrium for a saturated porous body:

$$\left(\int_V \mathbf{B}^T \mathbf{D} \mathbf{B} dV \right) \boldsymbol{\delta} - \left(\int_V \mathbf{B}^T \mathbf{i} \mathbf{N}_p dV \right) \mathbf{p} = \int_\Sigma \mathbf{N}_u \hat{\mathbf{t}} d\Sigma$$

which can be written in a more compact form as:

$$\mathbf{K}\boldsymbol{\delta} - \mathbf{Q}\mathbf{p} = \mathbf{f}^u \tag{1.8}$$

Note that $\mathbf{K}$ is a symmetric positive definite matrix.

The continuity of flow due to ground water movements is governed by the classical storage equation [Verruijt, 1969]:

$$\frac{1}{\gamma} \nabla (k \nabla p) = \phi \beta \frac{\partial p}{\partial t} + \frac{\partial \epsilon}{\partial t} + f \tag{1.9}$$

where γ and β are the specific weight and compressibility of water, respectively, ϕ is the porosity, k the hydraulic conductivity, ϵ the medium volumetric dilatation, f a forcing function including possible flow sources or sinks, ∇ the gradient operator, and t the time. Eq. (1.9) can be simply generalized to the case of deformable solid grains with compressibility c_{br} by:

$$\frac{1}{\gamma}\nabla\left(k\nabla p\right) = \left[\phi\beta + c_{br}\left(\alpha - \phi\right)\right]\frac{\partial p}{\partial t} + \alpha\frac{\partial \epsilon}{\partial t} + f \tag{1.10}$$

α being the Biot coefficient. For the purpose of the present chapter, the compressibility of the grains will be at the moment disregarded, thus assuming $\alpha = 1$. In the chapters that follow, however, also an appropriate value for c_{br} will be used.

Integration of (1.9) is obtained by applying the Galerkin method of weighted residuals:

$$\int_V \mathbf{N}_p^T\left[\frac{1}{\gamma}\nabla\left(k\nabla p\right) - \phi\beta\frac{\partial p}{\partial t} - \frac{\partial \epsilon}{\partial t} - f\right]dV = 0$$

Note that at least a parabolic approximation for p is necessary over each finite element, while for the displacements linear shape functions can be used. To avoid this discrepancy we use a weak formulation by applying the Green's identity to the first part of the above integral, thus obtaining:

$$\int_V \left(\nabla \mathbf{N}_p\right)^T\frac{k}{\gamma}\nabla p dV + \int_V \phi\beta\mathbf{N}_p^T\frac{\partial p}{\partial t}dV + \int_V \mathbf{N}_p^T\frac{\partial \epsilon}{\partial t}dV = \int_\Sigma \mathbf{N}_p^T\frac{k}{\gamma}\mathbf{n}^T\nabla p d\Sigma - \int_V \mathbf{N}_p^T f dV \tag{1.11}$$

with $\mathbf{n}$ normal vector to the surface Σ. Remembering that $\epsilon = \mathbf{i}^T\boldsymbol{\epsilon}$ and replacing the FE approximation of $\mathbf{u}$ and p into equation (1.11) yield:

$$\left(\int_V \frac{k}{\gamma}\left(\nabla \mathbf{N}_p\right)^T\nabla \mathbf{N}_p dV\right)\mathbf{p} + \left(\int_V \phi\beta\mathbf{N}_p^T\mathbf{N}_p dV\right)\dot{\mathbf{p}} + \left(\int_V \mathbf{N}_p^T\mathbf{i}^T\mathbf{B}dV\right)\dot{\boldsymbol{\delta}} =$$

$$\int_\Sigma \mathbf{N}_p^T\frac{k}{\gamma}\mathbf{n}^T\nabla p d\Sigma - \int_V \mathbf{N}_p^T f dV$$

that is:

$$\mathbf{H}\mathbf{p} + \mathbf{P}\dot{\mathbf{p}} + \mathbf{Q}^T\dot{\boldsymbol{\delta}} = \mathbf{f}^p \tag{1.12}$$

With an analogous procedure also equation (1.10) can be integrated. Observe that $\mathbf{H}$ and $\mathbf{P}$ are both symmetric and positive definite matrices.

Equations (1.8) and (1.12) are solved simultaneously for the unknown $\boldsymbol{\delta}$ and $\mathbf{p}$:

$$\begin{bmatrix} \mathbf{K} & -\mathbf{Q} \\ 0 & \mathbf{H} \end{bmatrix}\begin{Bmatrix} \boldsymbol{\delta} \\ \mathbf{p} \end{Bmatrix} + \begin{bmatrix} 0 & 0 \\ \mathbf{Q}^T & \mathbf{P} \end{bmatrix}\begin{Bmatrix} \dot{\boldsymbol{\delta}} \\ \dot{\mathbf{p}} \end{Bmatrix} = \begin{Bmatrix} \mathbf{f}^u \\ \mathbf{f}^p \end{Bmatrix}$$

The above system can be written in a compact form as the following first-order differential equation:

$$\mathbf{K}_1\mathbf{x} + \mathbf{K}_2\dot{\mathbf{x}} + \mathbf{f} = \mathbf{0}$$

and solved in time by applying an appropriate marching scheme. One of the most popular is the so-called θ-method. In this method the system of equations is solved in a time step of magnitude Δt by writing:

$$\dot{\mathbf{x}} = \frac{1}{\Delta t}\left(\mathbf{x}_{t+\Delta t} - \mathbf{x}_t\right)$$

and evaluating the other terms at an intermediate value of time such that:

$$\mathbf{x} = (1-\theta)\,\mathbf{x}_t + \theta\mathbf{x}_{t+\Delta t} \qquad \mathbf{f} = (1-\theta)\,\mathbf{f}_t + \theta\mathbf{f}_{t+\Delta t}$$

thus obtaining:

$$\left[\theta\mathbf{K}_1 + \frac{1}{\Delta t}\mathbf{K}_2\right]\mathbf{x}_{t+\Delta t} = \left[\frac{1}{\Delta t}\mathbf{K}_2 - (1-\theta)\,\mathbf{K}_1\right]\mathbf{x}_t - \left[\theta\mathbf{f}_{t+\Delta t} + (1-\theta)\,\mathbf{f}_t\right] \tag{1.13}$$

It has been shown that this method is stable for $\theta \geq 1/2$ [Booker and Small, 1975] also for a sequence of increasing Δt, as is typically the case in consolidation problems.

Equation (1.13) constitutes the linear system which is solved to find displacements and pore pressures in time domain:

$$\mathbf{A}_{\Delta t}\mathbf{x}_{t+\Delta t} = \mathbf{b}_t \tag{1.14}$$

The matrix arising from the coupled consolidation model is:

$$\mathbf{A}_{\Delta t} = \left[\theta\mathbf{K}_1 + \frac{1}{\Delta t}\mathbf{K}_2\right] = \begin{bmatrix} \theta\mathbf{K} & -\theta\mathbf{Q} \\ \dfrac{\mathbf{Q}^T}{\Delta t} & \theta\mathbf{H} + \dfrac{\mathbf{P}}{\Delta t} \end{bmatrix} \tag{1.15}$$

which is non-symmetric and needs to be factorized at each time step because of the variability of Δt during the simulation if a direct solution method is used. It can be observed that $\mathbf{A}_{\Delta t}$ could be simply symmetrized by premultiplying the second set of equations by $-\theta\Delta t$. However, this gives no practical advantage in the numerical solution to (1.14) since the resulting matrix has negative eigenvalues, as shown by Gambolati *et al.* [2001b]. In this case, stability of solution may become an issue for some values of the time step [Lewis and Schrefler, 1998] and the classical Conjugate Gradient method cannot be used. For these reasons, in the following the solution to equations (1.14) will be analyzed using the matrix $\mathbf{A}_{\Delta t}$ in the unsymmetric form expressed by (1.15).

1.3 Ill-conditioning of the coupled system

The possible ill-conditioning arising from the FE integration of coupled consolidation equations, especially in the early stages of the simulation, can be considered a quite common experience [Ferronato *et al.*, 2001]. In a generic ill-conditioned linear system, two or more rows are nearly parallel. This condition applied to rows i and m of the consolidation matrix (1.15) leads to:

$$\frac{\theta K_{ij}}{Q^T_{mj}/\Delta t} \simeq \frac{-\theta Q_{ik}}{\theta H_{mk} + P_{mk}/\Delta t} \qquad j = 1, \ldots, n_u \qquad k = 1, \ldots, n_p \tag{1.16}$$

where n_u and n_p are the number of unknowns for nodal displacement and pore pressure, respectively. The value of Δt satisfying equation (1.16) causes ill-conditioning of $\mathbf{A}_{\Delta t}$ and so it will be denoted as the critical time step Δt_{crit} for the problem.

Equation (1.16) can be solved by substituting the terms that belong to the blocks forming the global matrix $\mathbf{A}_{\Delta t}$ with a rough estimate of their magnitude. Let us assume to use tetrahedral elements for 3-D problems and annular elements with a triangular cross-section for axi-symmetric problems. This choice allows for a large number of elements in the porous medium discretization, which enables a more realistic representation of the natural significant variability in the lithologic sequence, especially in problems related to the development of deep gas/oil fields (see for instance Baù *et al.* [2000b], Teatini *et al.* [2000], Baù *et al.* [2001]).

The coefficient K_{ij} is proportional to the elements of the elastic stress strain matrix $\mathbf{D}$, and hence has the order of magnitude of the Young modulus E. Similarly, H_{mk} and P_{mk} are approximately proportional to k/γ and $\Omega\phi\beta$, respectively, where Ω represents a characteristic dimension of the FE grid. In the case of an axisymmetric problem Ω is the triangle area. The $\mathbf{Q}$ terms correspond to the projections of the element boundary along the coordinate directions [Gambolati *et al.*, 2001a], and so they can be approximated by $\sqrt{\Omega}$. Replacing the above approximations into equation (1.16) and solving for Δt we obtain:

$$\Delta t_{crit} \simeq \left(\frac{1-\psi}{\theta}\right)\frac{\Omega\gamma}{kE} \tag{1.17}$$

with:

$$\psi = \phi\beta E \tag{1.18}$$

Note that in the previous procedure the influence of the mesh geometry has been completely neglected, so equation (1.17) must be viewed only as the basic relation between Δt_{crit} and the physical parameters of the porous medium through a characteristic measure

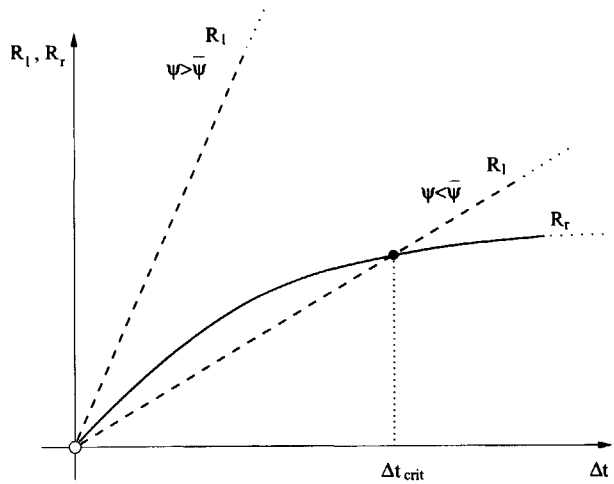

Figure 1.1: Qualitative behavior of left-hand side R_l and right-hand side R_r of eq. (1.16) vs. Δt and $\psi = \phi\beta E$.

of triangulation. More generally, we can write Δt_{crit} as [Ferronato *et al.*, 2001]:

$$\Delta t_{crit} = \chi(\psi, \theta) \frac{\Omega\gamma}{kE} \tag{1.19}$$

where χ is an unknown dimensionless factor depending upon ψ, θ, and the shape and resolution of the mesh.

Equation (1.16) allows for an interesting geometric interpretation. Write equation (1.16) as follows:

$$\Delta t \frac{\theta K_{ij}}{Q^T_{mj}} \simeq \frac{-\Delta t \theta Q_{ik}}{\Delta t \theta H_{mk} + P_{mk}} \quad \Rightarrow \quad R_l(\Delta t) \simeq R_r(\Delta t)$$

and compare graphically, as shown in Figure 1.1, the functions R_l and R_r.

It can be noted that for $\Delta t > \Delta t_{crit}$ the difference between R_l and R_r grows with the time step size, so the matrix parallelism reduces and the system is well-conditioned. By contrast, for $\Delta t \leq \Delta t_{crit}$ R_l remains close to R_r, and consequently the system is expected to be ill-conditioned also below the critical condition.

Observe in Figure 1.1 that an intersection between R_l and R_r exists only if:

$$\left[\frac{dR_l}{d\Delta t}\right]_{\Delta t=0^+} < \left[\frac{dR_r}{d\Delta t}\right]_{\Delta t=0^+} \tag{1.20}$$

which represents a necessary condition for the existence of Δt_{crit}. Equation (1.20), with

the aforementioned approximations for the matrix coefficients, gives:

$$\frac{E}{\sqrt{\Omega}} < \bar{\psi}\frac{\sqrt{\Omega}}{\Omega\phi\beta} \quad \Rightarrow \quad \psi < \bar{\psi} \tag{1.21}$$

where $\bar{\psi}$ is a factor which accounts for the quantities neglected in our estimates, i.e. basically the mesh geometry. Thus, it can be argued from equation (1.21) that a bound value $\bar{\psi}$ exists for ψ above which $\mathbf{A}_{\Delta t}$ will be well-conditioned independently on the time step size.

A different lower limit for Δt was derived by Vermeer and Verruijt [1981] depending on the accuracy of the pore pressure solution in a consolidating porous column. This bound was explicitly calculated for 1-D problems as:

$$\Delta t \geq \frac{1}{6}\frac{(\Delta h)^2}{\theta c} \tag{1.22}$$

with c the consolidation coefficient and Δh a characteristic size of the FE grid. The authors claim that a similar expression holds true for 2-D and 3-D problems as well. Replacing into equation (1.22) the expressions

$$c = \frac{k}{\gamma\left(\mu/E + \phi\beta\right)}$$

$$\mu = \frac{(1+\nu)(1-2\nu)}{1-\nu}$$

$$(\Delta h)^2 \simeq \Omega$$

with ν the Poisson ratio, we obtain:

$$\Delta t_{crit} = \left(\frac{\mu + \psi}{6\theta}\right)\frac{\Omega\gamma}{kE} = \chi'(\psi, \theta)\frac{\Omega\gamma}{kE} \tag{1.23}$$

Note that equation (1.23) is very similar to equation (1.19), although the implications of the two time step limits are different. This shows that ill-conditioning of the problem and accuracy of solution are basically connected one to another since they depend on the same combination of physical parameters. It is also interesting to observe that the parameter $kE\Delta t/(\Omega\gamma)$ corresponds to Terzaghi's [1925] dimensionless time factor:

$$T = \frac{ct}{H^2}$$

with H the height of the consolidating column. Hence both analyses can be regarded as a generalization to finite elements of the early work by Terzaghi for the 1-D problem. The main difference between the critical time steps arising from equations (1.19) and (1.23) stems from the weighting factors χ and χ'. In fact, while for the ill-conditioning problem a $\bar{\psi}$ value may be found for ψ above which no Δt_{crit} exists, in the accuracy condition χ' is never zero or negative, and hence a lower bound for the time step size always exists.

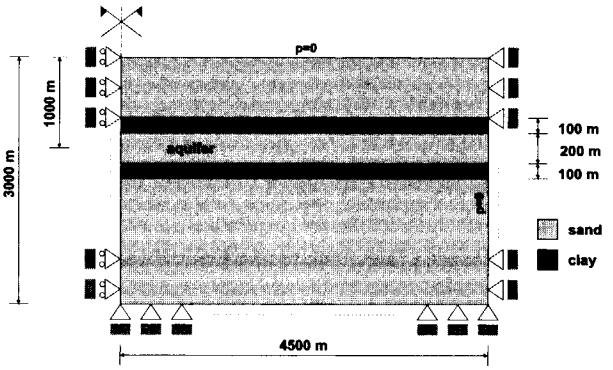

Figure 1.2: Schematic representation of the stratified porous medium used as test problem

1.3.1 Numerical examples

An axisymmetric porous body with a volume distributed sink from an aquifer located at a depth of 1000 m is considered as a test problem (Figure 1.2). The medium consists of a sequence of alternating sandy and clayey layers with a Poisson ratio $\nu = 0.25$ and variable permeability, stiffness and discretization. Standard Dirichlet conditions are prescribed, with fixed outer and bottom boundaries, and zero pore pressure variation on the top and outer surfaces (see Figure 1.2). A first order finite difference backward scheme is used ($\theta = 1$).

The matrix conditioning for different time steps can be measured by the indexes [Westlake, 1968]:

$$L = \frac{|\lambda_1|}{|\lambda_N|} \qquad D = \frac{\prod_{i=1}^{N} \left(\sum_{j=1}^{N} a_{ij}^2\right)^{1/2}}{|\det \mathbf{A}_{\Delta t}|}$$

where λ_1 and λ_N are the maximum and minimum eigenvalue of $\mathbf{A}_{\Delta t}$, N is the size, and a_{ij} the $\mathbf{A}_{\Delta t}$ coefficients. Ill-conditioning is indicated by an increase of both L and D values as Δt varies.

Let us consider a regular discretization for the test problem of Figure 1.2, with the radial spacing Δr and the vertical spacing Δz equal to 25 m ($\Omega = 312.5$ m^2), $k_{\text{sand}} = 10^{-5}$ m/s and $k_{\text{clay}} = 10^{-8}$ m/s. The medium is homogeneous from a mechanical point of view and the Young's modulus ranges between $8.16 \cdot 10^2$ MPa and $8.16 \cdot 10^0$ MPa in three test cases. Ill-conditioning of the coupled matrix generated by the problems is estimated by L and D for a time step Δt varying from 10^6 to 1 s, and the results are shown in Figure 1.3. The critical time step is easily identified by the sudden growth of L. Note that Δt_{crit} increases as E decreases, as predicted by equation (1.19), but the relationship

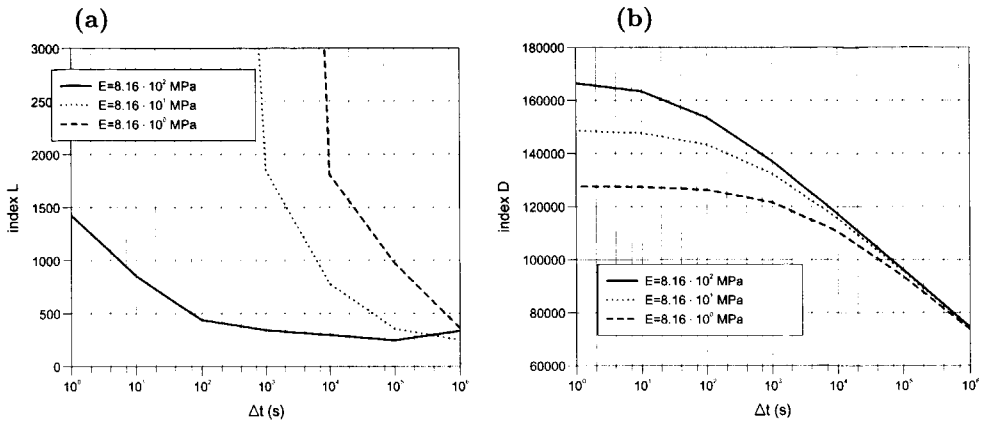

Figure 1.3: (a) L vs Δt and (b) D vs Δt for $k_{\text{sand}} = 10^{-5}$ m/s, $k_{\text{clay}} = 10^{-8}$ m/s, $\Omega = 312.5$ m^2, and variable E.

is not exactly linear since χ depends on ψ, and hence on E too, because of (1.18). The nonlinearity introduced by χ becomes more evident as ψ increases. It is interesting to observe also the behavior of index D in Figure 1.3b, since it gives a measure of the parallelism of matrix rows (when they are exactly parallel, $\det \mathbf{A}_{\Delta t} = 0$ and $D \to \infty$). D achieves its maximum value in the vicinity of Δt_{crit} and then it remains constant as Δt decreases, thus providing evidence that some rows are almost parallel also below the critical time step. In particular, note from comparison of Figure 1.3a and Figure 1.3b that a sudden increase of L coincides with a slope change in D, which indicates that the problem is near to the critical condition. Since the computation of D is quite inexpensive, the preliminary analysis of D vs Δt may be a practical way to estimate a priori the interval where Δt_{crit} may fall in a coupled poroelastic problem.

We now use an intermediate value for E, i.e. $8.16 \cdot 10^1$ MPa, and vary k_{sand} from 10^{-5} to 10^{-7} m/s, and k_{clay} from 10^{-8} to 10^{-10} m/s. The behavior of L and D vs Δt is reported in Figure 1.4. The critical time step can be identified from the increasing of L and the slope change of D, as shown before. Note that in this case the Δt_{crit} increase is proportional to the k decrease. This is consistent with equation (1.19) since the factor χ does not depend on permeability.

Finally the influence of grid refinement is investigated by considering the problem with $E = 8.16 \cdot 10^1$ MPa, $k_{\text{sand}} = 10^{-5}$ m/s, $k_{\text{clay}} = 10^{-8}$ m/s, and Δr and Δz varying from 25 to 100 m (i.e. Ω ranging between 312.5 and 5000 m^2). The results for L are shown in Figure 1.5, where a different scale for the two test cases has been used to account for

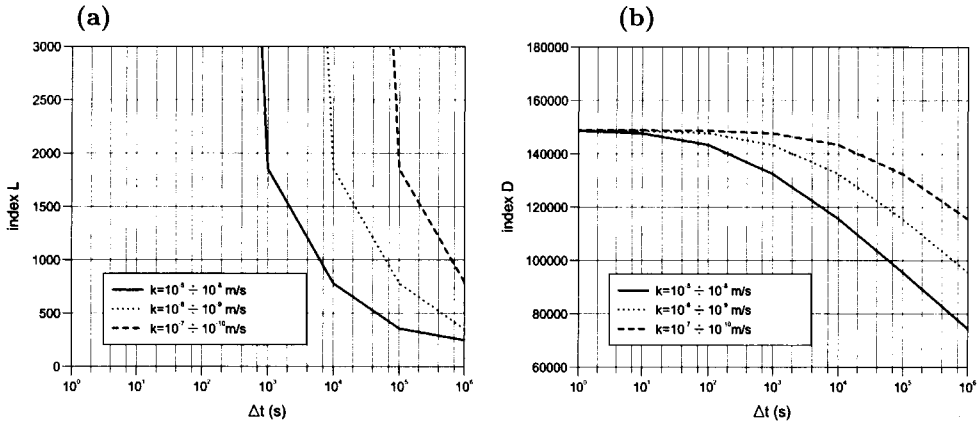

Figure 1.4: (a) L vs Δt and (b) D vs Δt for $E = 8.16 \cdot 10^1$ MPa, $\Omega = 312.5$ m^2, and variable k_{sand} and k_{clay}.

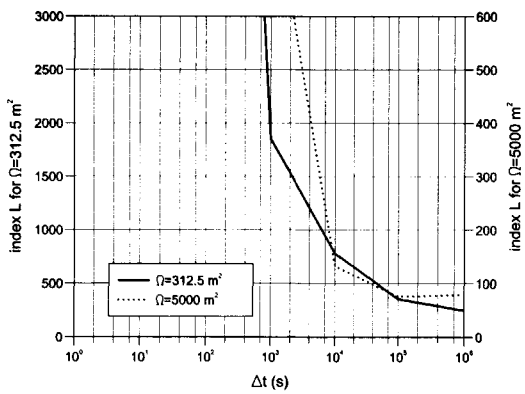

Figure 1.5: L vs Δt for $E = 8.16 \cdot 10^1$ MPa, $k_{\text{sand}} = 10^{-5}$ m/s, $k_{\text{clay}} = 10^{-8}$ m/s, and variable Ω.

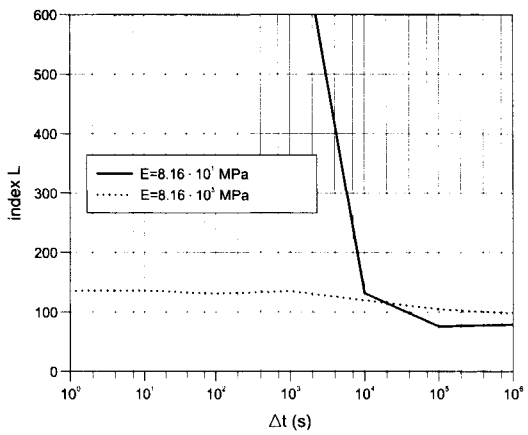

Figure 1.6: L vs Δt for $E = 8.16 \cdot 10^3$ MPa, $k_{\text{sand}} = 10^{-7}$ m/s, $k_{\text{clay}} = 10^{-10}$ m/s, $\Omega = 5000$ m^2 (dotted profile) and $E = 8.16 \cdot 10^1$ MPa, $k_{\text{sand}} = 10^{-5}$ m/s, $k_{\text{clay}} = 10^{-8}$ m/s, $\Omega = 5000$ m^2 (solid profile).

the different size of $\mathbf{A}_{\Delta t}$ with the new discretization. Observe that the problem with the higher mesh resolution exhibits the smallest Δt_{crit} although the size is much larger (65703 unknowns vs 4278), and hence it can be solved without ill-conditioning problems for a wider range of time steps. This is in agreement with equation (1.19), which also shows that the variation of Δt_{crit} is nonlinear with Δ since χ is dependent on both the shape and the resolution of the mesh. It must be realized, however, that for a finer mesh the computational effort increases with the number of unknowns, and that takung smaller steps further increases the computational time.

Equation (1.21) gives a necessary condition for the existence of Δt_{crit} dependent on the value of ψ, and hence ultimately on E. According to this result, we should be able to find a stiffness value generating a matrix $\mathbf{A}_{\Delta t}$ which is well-conditioned for any Δt however small, independently on the permeability and mesh used. Let us consider a problem with $k_{\text{sand}} = 10^{-7}$ m/s, $k_{\text{clay}} = 10^{-10}$ m/s, and $\Omega = 5000$ m^2, which yield the largest Δt_{crit} in the previous examples, and assume $E = 8.16 \cdot 10^3$ MPa. The behavior of L vs Δt, compared to the same test case as in Figure 1.5 for the coarser mesh, is shown in Figure 1.6. It can be observed that $\mathbf{A}_{\Delta t}$ does not exhibit a critical time step and the conditioning is good independently on k and Ω, thus confirming the validity of condition (1.21).

1.4 Solution by Conjugate Gradient like methods

Conjugate gradient (CG)-like solvers appear to be very attractive for the solution to large size sparse sets of indefinite equations, since they involve only matrix-vector and vector-vector products, and hence require a relatively limited core memory and can be easily implemented on parallel computers. The solution to equation (1.14) is obtained by projecting the system onto Krylov subspaces of increasing dimension ℓ and solving the projected system. Denoting by $\mathbf{r}_0$ the residual corresponding to an initial guessed solution, the Krylov subspace with size ℓ is generated by the vectors:

$$\left\{\mathbf{r}_0, \mathbf{A}_{\Delta t}\mathbf{r}_0, \mathbf{A}_{\Delta t}^2\mathbf{r}_0, \ldots, \mathbf{A}_{\Delta t}^{\ell-1}\mathbf{r}_0\right\}$$

and will be indicated in the following as $\mathcal{K}_\ell\left(\mathbf{A}_{\Delta t}, \mathbf{r}_0\right)$. The approximate ℓ-size solution in the current subspace is achieved by prescribing the orthogonality of the current residual $\mathbf{r}_\ell$ to an auxiliary subspace $\mathcal{L}_\ell$ via the Petrov-Galerkin condition [Gambolati *et al.*, 1995]. The most common choices for $\mathcal{L}_\ell$ are the following:

1. $\mathcal{L}_\ell \equiv \mathcal{K}_\ell$
2. $\mathcal{L}_\ell \equiv \mathcal{K}_\ell\left(\mathbf{A}_{\Delta t}, \mathbf{A}_{\Delta t}\mathbf{r}_0\right)$
3. $\mathcal{L}_\ell \equiv \mathcal{K}_\ell\left(\mathbf{A}_{\Delta t}^{\mathrm{T}}, \mathbf{r}_0\right)$

It can be demonstrated [Saad, 1996] that the Petrov-Galerkin condition applied to $\mathcal{L}_\ell$ defined as in point 2 corresponds to the minimization of $\mathbf{r}_\ell$ in the current subspace. However, the most recent evolutions of CG-like solvers for unsymmetric indefinite equations have been developed defining $\mathcal{L}_\ell$ as in point 3. One of the most popular and efficient algorithms belonging to this class is the bi-conjugate gradient stabilized (Bi-CGSTAB [Van der Vorst, 1992]), which has proved to be a robust and cost-effective solver for different problems, e.g. Gambolati *et al.* [1995, 1996].

The original scheme of bi-conjugate gradient (BCG) algorithms was developed by Lanczos [1952] by generating a bi-orthogonal vector basis for $\mathcal{K}_\ell$ and $\mathcal{L}_\ell$ using two elegant and cost-effective three-term recurrent relations. To avoid the explicit multiplication between the transposed matrix and a vector, the residual $\mathbf{r}_\ell$ can be computed as:

$$\mathbf{r}_\ell = \Phi_\ell^2\left(\mathbf{A}_{\Delta t}\right)\mathbf{r}_0$$

where Φ_ℓ is an appropriate ℓ-degree polynomial function of $\mathbf{A}_{\Delta t}$, thus giving rise to the conjugate gradient squared algorithm (CGS [Sonneveld, 1989]). Bi-CGSTAB is a stabilized evolution of CGS in which the erratic residual behavior induced by Φ_ℓ^2 is effectively

Calculate $\mathbf{r}_0 = \mathbf{b} - \mathbf{A}\mathbf{x}_0$ from the initial guess $\mathbf{x}_0$
Choose $\tilde{\mathbf{r}}_0$ such that $\tilde{\mathbf{r}}_0^T \tilde{\mathbf{r}}_0 \neq 0$ (e.g. $\tilde{\mathbf{r}}_0 = \mathbf{r}_0$)
Initialize the constants:
$\rho_{-1} = \alpha_{-1} = \eta_0 = 1$
$\mathbf{p}_{-1} = \mathbf{v}_{-1} = \mathbf{0}$

For $j = 0, 1, 2, \ldots$ until convergence do:
$\rho_j = \tilde{\mathbf{r}}_0^T \tilde{\mathbf{r}}_j$
$\beta_j = (\rho_j / \rho_{j-1})\,(\alpha_{j-1} / \eta_j)$
$\mathbf{p}_j = \mathbf{r}_j + \beta_j\,(\mathbf{p}_{j-1} - \eta_j \mathbf{v}_{j-1})$
$\mathbf{v}_j = \mathbf{A}\mathbf{p}_j$
$\alpha_j = \rho_j / \tilde{\mathbf{r}}_0^T \mathbf{v}_j$
$\mathbf{s} = \mathbf{r}_j - \alpha_j \mathbf{v}_j$
$\mathbf{t} = \mathbf{A}\mathbf{s}$
$\eta_{j+1} = \mathbf{s}^T\mathbf{t} / \mathbf{t}^T\mathbf{t}$
$\mathbf{x}_{j+1} = \mathbf{x}_j + \alpha_j \mathbf{p}_j + \eta_{j+1}\mathbf{s}$
$\mathbf{r}_{j+1} = \mathbf{s} - \eta_{j+1}\mathbf{t}$
End For

Figure 1.7: The Bi-CGSTAB algorithm.

smoothed computing $\mathbf{r}_\ell$ as:

$$\mathbf{r}_\ell = \Psi_\ell\,(\mathbf{A}_{\Delta t})\,\Phi_\ell\,(\mathbf{A}_{\Delta t})\,\mathbf{r}_0$$

where the polynomial function Ψ_ℓ is updated at each iteration with a steepest-descent procedure. The resulting algorithm appears to be very similar to the classical conjugate gradient and easy to implement both in scalar and in parallel computers (Figure 1.7). Bi-CGSTAB typically exhibits an erratic convergence, yet it is much more stable than CGS [Van der Vorst, 1992].

Projection or CG-like methods should be classified in exact arithmetic as direct solvers, since the solution is theoretically obtained at least after N iterations, denoting with N the system size. However, convergence can be practically achieved much before N, even though in some cases round-off errors can prevent from obtaining the solution, so that CG-like algorithms can be viewed on the overall as fully iterative methods. In particular, the residual orthogonalization procedure used by Bi-CGSTAB does not correspond to any global minimization of $\mathbf{r}_\ell$, so convergence is not theoretically guaranteed and the solver can break down. Nevertheless, Bi-CGSTAB has proved to be one of the most robust and efficient algorithms in the class of projection solvers.

In the following sections the use of Bi-CGSTAB in consolidation models is investigated. It will be shown that such method possesses a great potential for the global solution to this problem, especially if appropriate preliminary numerical strategies are adopted in order to

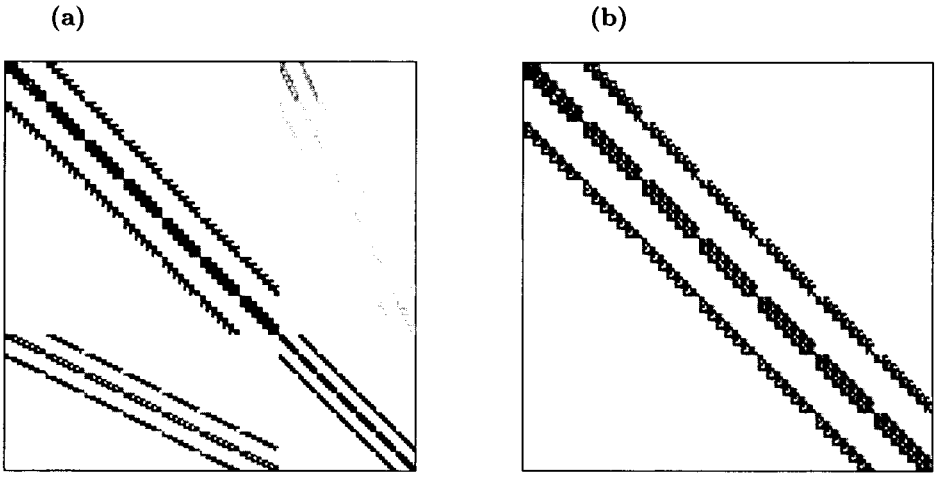

Figure 1.8: Sparsity structure of the matrix $\mathbf{A}_{\Delta t}$ with (a) the ordering suggested by (1.15), and (b) the nested ordering $(\delta_{x_1}, \delta_{y_1}, \delta_{z_1}, p_1, \delta_{x_2}, \delta_{y_2}, \delta_{z_2}, p_2, \ldots)$. The grayscale indicates the magnitude of each element.

mitigate, as far as possible, the intrinsic ill-conditioning of the FE coupled consolidation equations.

1.4.1 Nodal ordering

The convergence of a CG-like solver, especially if preconditioned with an incomplete matrix factorization, is related to the nodal ordering of the unknowns, which can drastically modify the sparsity pattern of matrix $\mathbf{A}_{\Delta t}$ [Duff and Meurant, 1989]. The natural way of numbering the variables with the displacements coming first and pore pressures coming next, as suggested by the notation used in (1.15), gives rise to a very large bandwidth, as shown in Figure 1.8a. Note that, although the sparsity pattern is symmetric, the rectangular blocks have different coefficients, so that the matrix is unsymmetric. A large bandwidth is a disadvantage especially for the generation of an effective preconditioner based on the incomplete triangular factorization of the system matrix. In this case, a very large fill-in degree should be necessary to obtain a sufficiently good approximation of the triangular factors of $\mathbf{A}_{\Delta t}$, thus increasing the core memory requirement, and the computational cost.

A simple, intuitive, and inexpensive way of ordering the unknowns is to nest displacements and pore pressures, so that the vector $\mathbf{x}_{t+\Delta t}$ of equation (1.14) is made of the components $(\delta_{x_1}, \delta_{y_1}, \delta_{z_1}, p_1, \delta_{x_2}, \delta_{y_2}, \delta_{z_2}, p_2, \ldots)$. The sparsity pattern of $\mathbf{A}_{\Delta t}$ generated by such ordering is illustrated in Figure 1.8b. Note that by this simple permutation a much

reduced bandwidth turns out, which may help the construction of a more effective and lower-cost preconditioner. We recall on passing that only the non-zero elements of $\mathbf{A}_{\Delta t}$ are actually stored, with their original location indicated by appropriate pointing vectors. This is a quite common technique which allows for an effective saving in the core memory requirement.

1.4.2 Preconditioning techniques

One of the key factors for the success of any CG-like solver is the use of an effective and relatively inexpensive preconditioning technique. The basic idea of preconditioning is to find a non-singular matrix $\mathbf{M}$ which approximates in some measure $\mathbf{A}_{\Delta t}$ of equation (1.14). Assuming that $\mathbf{M}$ can be factorized as the product $\mathbf{M}_1\mathbf{M}_2$, the original system (1.14) can be replaced by:

$$\mathbf{M}_1^{-1}\mathbf{A}_{\Delta t}\mathbf{M}_2^{-1}\mathbf{M}_2\mathbf{x}_{t+\Delta t} = \mathbf{M}_1^{-1}\mathbf{b}_t$$

that is:

$$\mathbf{A}'_{\Delta t}\mathbf{x}'_{t+\Delta t} = \mathbf{b}'_t \tag{1.24}$$

Bi-CGSTAB is used for solving the preconditioned system (1.24). To avoid the explicit computation of the primed variables, the native algorithm of Figure 1.7 is rewritten with the following corrispondence with the original variables:

$$\mathbf{x}_{t+\Delta t} = \mathbf{M}_2^{-1}\mathbf{x}'_{t+\Delta t} \qquad \mathbf{r}_\ell = \mathbf{M}_1\mathbf{r}'_\ell \tag{1.25}$$

As can be easily deduced from equations (1.24) and (1.25), to be of some advantage the preconditioned system must converge faster than the original one, and the matrix-vector products by $\mathbf{M}^{-1}$, $\mathbf{M}_1$, and $\mathbf{M}_2^{-1}$, which are additionally required at each iteration, must be performed almost inexpensively. Consequently, a suitable preconditioner must be a sufficiently good approximation of $\mathbf{A}_{\Delta t}$ without allowing for a too large fill-in. One of the most popular and efficient preconditioning techniques is derived from the class of the incomplete triangular factorization of $\mathbf{A}_{\Delta t}$.

The simplest preconditioner belonging to this class is ILU(0) (Incomplete LU factorization with zero fill-in [Meijerink and van der Vorst, 1977; Kershaw, 1978]):

$$\mathbf{M}^{-1} = \tilde{\mathbf{U}}^{-1}\tilde{\mathbf{L}}^{-1}$$

where $\tilde{\mathbf{U}}$ and $\tilde{\mathbf{L}}$ are the upper and lower triangular factors of $\mathbf{A}_{\Delta t}$ computed so as to preserve the sparsity pattern of the original matrix, and hence dropping all new fill-in elements generated during the process. ILU(0) is the most inexpensive incomplete

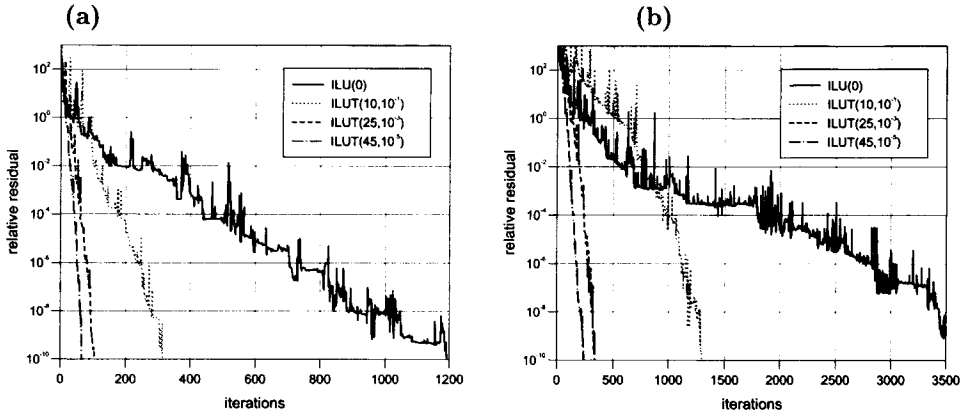

Figure 1.9: Bi-CGSTAB convergence profiles with different preconditioners for $\Omega = 312.5$ m^2, $k_{\text{sand}} = 10^{-5}$ m/s, $k_{\text{clay}} = 10^{-8}$ m/s, and (a) $E = 8.16 \cdot 10^2$ MPa, $\Delta t = 1$ s; (b) $E = 8.16 \cdot 10^1$ MPa, $\Delta t = 10^2$ s.

factorization, but it may turn out to be a poor approximation of $\mathbf{A}_{\Delta t}$, especially in ill-conditioned problems. A recent evolution of ILU(0) is ILUT(ρ, τ) (Incomplete LU factorization with Threshold strategies [Saad, 1994]), which allows for a partial fill-in of $\tilde{\mathbf{L}}$ and $\tilde{\mathbf{U}}$ controlled by the parameters ρ and τ as follows:

- ρ (fill-in level) specifies the maximum number of newly created elements to be preserved in each $\tilde{\mathbf{L}}$ and $\tilde{\mathbf{U}}$ row;
- τ (tolerance) sets a limit to the magnitude of $\tilde{\mathbf{L}}$ and $\tilde{\mathbf{U}}$ elements such that the element is dropped if smaller than $\tau \|\mathbf{a}_i\|_2$, with $\|\mathbf{a}_i\|_2$ the Euclidean norm of the corrispondent $\mathbf{A}_{\Delta t}$ row.

The quality and efficiency of ILUT depend on the choice for ρ and τ.

The performance of ILU(0) and ILUT in coupled consolidation models is analyzed in some numerical examples. Let us consider the problem described is Section 1.3.1 with $\Delta r = \Delta z = 25$ m ($N = 65703$), $k_{\text{sand}} = 10^{-5}$ m/s, $k_{\text{clay}} = 10^{-8}$ m/s, and $E = 8.16 \cdot 10^2$ MPa (case (a)) and $E = 8.16 \cdot 10^1$ MPa (case (b)). In the two test-cases the time step Δt has been chosen in the vicinity of the critical condition, so as to simulate a severely ill-conditioned problem. We use $\Delta t = 1$ s in case (a) and $\Delta t = 10^2$ s in case (b), which are slightly larger and smaller than Δt_{crit}, respectively (see Figure 1.3). The convergence profiles obtained using Bi-CGSTAB preconditioned with ILU(0) and ILUT(ρ, τ) are shown for the two problems in Figure 1.9a and 1.9b. The required real relative residual for convergence is set to 10^{-10}. Note that, increasing ρ and decreasing τ, ILUT proves more

and more efficient, with a significant acceleration of the convergence rate of about one order of magnitude. This is due to the fact that, for example, with $\rho = 45$ and $\tau = 10^{-5}$, a better approximation of $\mathbf{A}_{\Delta t}^{-1}$ is obtained since fewer important elements are neglected in the incomplete factorization procedure.

	case (a)			case (b)		
	T_p	T_c	T_t	T_p	T_c	T_t
ILU(0)	0.7	208.8	209.5	0.6	504.0	504.6
ILUT(10,10^{-1})	1.8	63.4	65.2	1.7	218.5	220.2
ILUT(25,10^{-3})	7.0	31.2	38.2	6.7	78.1	84.8
ILUT(45,10^{-5})	18.5	20.6	39.1	18.5	76.7	95.2

Table 1.1: CPU times (s) for computing the preconditioner (T_p) and achieving the convergence (T_c) in case (a) and (b). T_t is the total CPU time ($= T_p + T_c$).

However, the computational cost spent for computing the preconditioner and the matrix-vector products at each iteration may increase, so a complete comparison must also include a CPU time analysis in order to assess the most convenient choice. Table 1.1 reports the CPU times for the calculation of preconditioner and for convergence in the two problems. Observe that in both cases ILUT(25,10^{-3}) provides the smallest total computational time T_t, while ILUT(45,10^{-5}) yields the fastest convergence. Thus ILUT(25,10^{-3}) appears to be in these cases the most effective preconditioner since it involves the best trade-off between improving the preconditioner quality and lowering the cost of computation.

ILU(0) may become competitive with ILUT(ρ, τ) for relatively small and well-conditioned problems. Let us consider the porous volume of Figure 1.2 with $\Delta r = \Delta z = 100$ m ($N = 4278$), $k_{\text{sand}} = 10^{-7}$ m/s, $k_{\text{clay}} = 10^{-10}$ m/s, and $E = 8.16 \cdot 10^3$ MPa. As shown in Figure 1.6, this problem (case (c)) is well-conditioned for any Δt however small. We choose $\Delta t = 1$ s. The convergence profiles and CPU times for case (c) are reported in Figure 1.10 and Table 1.2, respectively. As expected, the preconditioner improvement provided by ILUT yields a faster convergence, but the smallest computational cost is obtained with ILU(0).

1.4.3 Scaling algorithms

One of the main sources of ill-conditioning of FE coupled consolidation equations stems from the large difference in size between the terms belonging to the structural equations (matrices $\mathbf{K}$ and $\mathbf{Q}$ of eq. (1.8)) and to the flow equation (matrices $\mathbf{H}$ and $\mathbf{P}$ of eq. (1.12)).

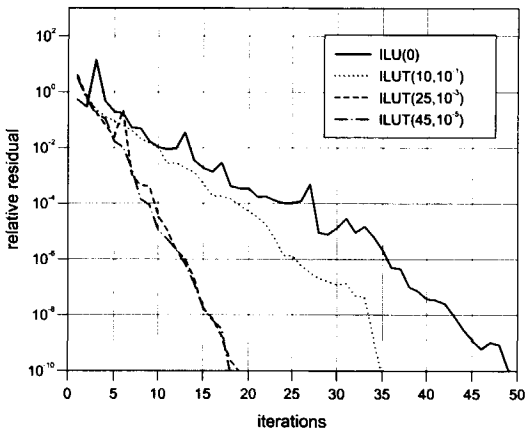

Figure 1.10: Bi-CGSTAB convergence profiles with different preconditioners for $\Omega = 5000$ m^2, $k_{\text{sand}} = 10^{-7}$ m/s, $k_{\text{clay}} = 10^{-10}$ m/s, $E = 8.16 \cdot 10^3$ MPa, and $\Delta t = 1$ s.

	case (c)		
	T_p	T_c	T_t
ILU(0)	0.03	0.37	0.40
ILUT(10,10^{-1})	0.10	0.31	0.41
ILUT(25,10^{-3})	0.35	0.22	0.57
ILUT(45,10^{-5})	0.76	0.34	1.10

Table 1.2: CPU times (s) for computing the preconditioner (T_p) and achieving the convergence (T_c) in case (c). T_t is the total CPU time ($= T_p + T_c$).

For such a reason, the use of appropriate row or column scaling strategies may prove an important operation to improve the global matrix conditioning and accelerate the convergence rate of Bi-CGSTAB. In fact, scaling of rows and/or columns can be viewed as a preconditioning technique in which $\mathbf{M}_1$ and/or $\mathbf{M}_2$ of equation (1.24) are diagonal matrices. Row, column, and global scalings correspond to left, right, and split preconditionings, respectively. However, since the product $\mathbf{M}_1\mathbf{M}_2$ often results in a very poor approximation of $\mathbf{A}_{\Delta t}$, the system (1.14) may be first scaled, and then preconditioned by the most convenient ILUT factorization.

The most intuitive and simple scaling strategy is the well-known standard Jacobi algorithm, in which each row (column) is scaled by the diagonal term. As has recently been observed [Chan *et al.*, 2001], the FE equations (1.12) derived from the flow model usually possess very small diagonal terms compared to the off-diagonal ones, and hence the Standard Jacobi algorithm may generate very large off-diagonal entries. Chan *et al.* [2001]

suggest to scale the $\mathbf{A}_{\Delta t}$ rows (columns) corresponding to the pore pressure equations by the largest absolute value of the off-diagonal terms belonging to the same row (column), thus avoiding the presence of large off-diagonal entries. This strategy will be denoted in the sequel as Modified Jacobi algorithm.

A more complex scaling method is proposed by Curtis and Reid [1972], who suggest having the entries of the scaled matrix as near to unity as possible. This is accomplished by minimizing the sum of the squares of the logarithms of the scaled coefficients. The scaling factors r_i for row i and c_j for column j are chosen so as to minimize the function:

$$\Gamma = \sum_{i,j} (\ln |a_{ij}| - r_i - c_j)^2 \tag{1.26}$$

where $\sum$ is taken over all i and j such that $a_{ij} \neq 0$. The solution to the least square problem (1.26) is obtained by solving the equations:

$$\frac{\partial \Gamma}{\partial r_i} = 0 \qquad \frac{\partial \Gamma}{\partial c_j} = 0 \qquad i,j = 1,\ldots,N$$

i.e.:

$$\begin{cases} \sum_j \ln |a_{ij}| - m_i r_i - \sum_j c_j = 0 & i = 1,\ldots,N \\ \sum_i \ln |a_{ij}| - \sum_i r_i - n_j c_j = 0 & j = 1,\ldots,N \end{cases} \tag{1.27}$$

where the sums are taken over all i and j such that $a_{ij} \neq 0$, m_i is the number of the non-zero entries in row i, and n_j the number of non-zero entries in column j. The factors r_i and c_j obtained from the solution to (1.27) are used for scaling the matrix row i by $\exp(r_i)$ and the column j by $\exp(c_j)$, so that the new entries a'_{ij} are:

$$a'_{ij} = a_{ij} \exp(r_i + c_j)$$

The above least square scaling algorithm is implemented in the routine MC29AD of the Harwell Software Library [HSL, 2000], and in the following it will be referred to as the Least Square Log scaling.

A comparison between the performances of the aforementioned algorithms is made by scaling the $\mathbf{A}_{\Delta t}$ matrices generated from the consolidation problems discussed in the previous section as case (a) and case (b). In both problems Bi-CGSTAB is preconditioned with ILUT(25,10^{-3}), which has proved the most cost-effective preconditioner (see Table 1.1). The convergence profiles obtained in case (a) and (b) with different preliminary scalings are shown in Figure 1.11. Note that generally a preliminary scaling contributes to improve conditioning, and hence the convergence. In particular, Standard and Modified Jacobi algorithms exhibit similar performances, while the Least Square Log method appears to converge faster.

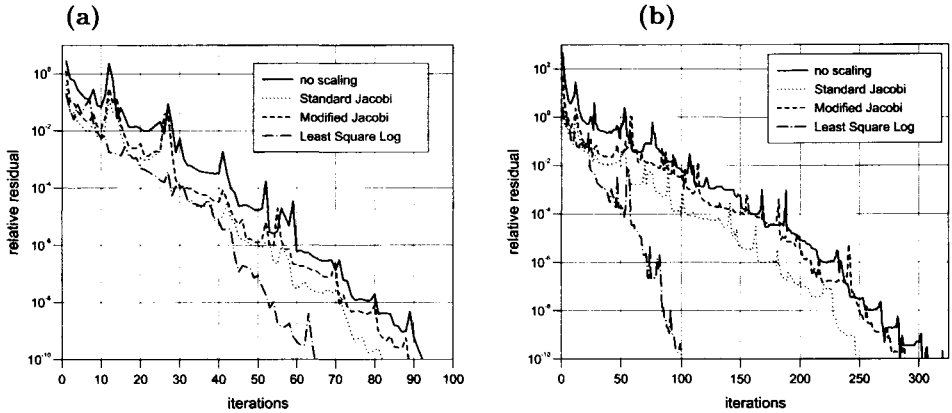

Figure 1.11: Bi-CGSTAB preconditioned by ILUT(25,10^{-3}) convergence profiles with different preliminary scalings for $\Omega = 312.5$ m^2, $k_{\text{sand}} = 10^{-5}$ m/s, $k_{\text{clay}} = 10^{-8}$ m/s, and (a) $E = 8.16 \cdot 10^2$ MPa, $\Delta t = 1$ s; (b) $E = 8.16 \cdot 10^1$ MPa, $\Delta t = 10^2$ s.

	case (a)				case (b)			
	T_s	T_p	T_c	T_t	T_s	T_p	T_c	T_t
No scaling	–	7.03	21.18	28.21	–	6.66	78.14	83.80
Standard Jacobi	0.02	6.68	19.22	25.92	0.02	6.69	65.57	72.28
Modified Jacobi	0.09	6.72	20.68	27.49	0.09	6.70	74.43	81.22
Least Square Log	0.59	9.53	16.14	26.27	0.59	10.33	27.80	38.73

Table 1.3: CPU times (s) for the matrix scaling (T_s), computing the preconditioner ILUT(25,10^{-3}) (T_p), and achieving the convergence (T_c) in case (a) and (b). T_t is the total CPU time ($= T_s + T_p + T_c$).

Table 1.3 summarizes the total computational times required by each problem solution. It can be noted that the Least Square Log scaling is the most costly scaling operation, and also needs the largest CPU time T_p for the preconditioner computation. On balance it may require a total larger computational cost, as in case (a) where the Standard Jacobi algorithm is slightly superior. However, in more difficult problems, such as case (b), the Least Square Log scaling is likely to exhibit a better performance overall.

It should be observed that the use of the Least Square Log preliminary scaling strategy allows for a very efficient solution to an originally severely ill-conditioned large size problem as case (b). The total computational time with the most efficient scaling strategy decreases about 15 times as compared to the total time required by the poorest option, i.e. Bi-CGSTAB preconditioned by ILU(0) with no scaling (38.7 s vs 504.6 s). Finally, observe that the preliminary scaling is in any case a cheap operation, which may provide a significant improvement of the matrix conditioning with an additional computational

cost T_s that is negligible compared to T_p or T_c.

1.5 Conclusions

The FE solution to coupled consolidation equations may be difficult because of the ill-conditioning of the coupled system and the large size typically required by realistic models. The present chapter reviews and discusses the relation between the hydrogeological parameters of the problem and the time step Δt yielding ill-conditioning through a characteristic measure of the FE grid. The empirical criterion for the critical time step is compared with the accuracy condition by Vermeer and Verruijt [1981], and then verified by a number of numerical experiments. An accurate, robust, and efficient solution strategy, based on preconditioned conjugate gradient-like methods applied on preliminarily scaled equations, is used to solve large size ill-conditioned realistic coupled consolidation models.

The following points are worth summarizing:

- a lower bound for the time step Δt exists below which the problem may become ill-conditioned. The critical time step is found to be larger for compressible and low permeable porous media discretized with coarse grids;
- a limiting stiffness for each porous medium exists such that for stiffer systems there is no critical time step, irrespective of the permeability values and the mesh resolution;
- ill-conditioning can be avoided by using a mesh shape and size that yields a Δt_{crit} smaller than the minimum Δt required by the simulation. A useful and practically inexpensive way to guess a priori Δt_{crit} is to use the condition number D. The critical time step is roughly denoted by a change in the derivative of D with respect to Δt;
- CG-like or projection methods appear to be quite attractive for the solution to large size indefinite unsymmetric systems generated by realistic FE coupled consolidation models. The main advantages stem from the high convergence rate, the limited core memory requirement, and the ease of parallelization. Among CG-like solvers, Bi-CGSTAB [Van der Vorst, 1992] effectively preconditioned has proved to be in most problems the most robust and efficient algorithm;
- nodal ordering affects the computational cost to generate the preconditioner and to achieve convergence since it may modify significantly the sparsity pattern of the

coefficient matrix. A numeration which reduces the bandwidth with no additional cost is obtained by nesting displacements and pore pressures so that the vector of the unknowns is made of the components $(\delta_{x_1}, \delta_{y_1}, \delta_{z_1}, p_1, \delta_{x_2}, \delta_{y_2}, \delta_{z_2}, p_2, \ldots)$;

- the incomplete LU factorization with a partial controlled fill-in (ILUT [Saad, 1994]) is an effective preconditioner for Bi-CGSTAB which allows for a significant acceleration of convergence, especially in difficult ill-conditioned problems;

- a preliminary scaling may be an efficient operation in order to improve the matrix conditioning and to accelerate convergence. The least square scaling algorithm applied on the logarithms of the matrix coefficients [Curtis and Reid, 1972] proves quite promising especially in large size problems.

Finally, the performance of the solution strategy reviewed in the present chapter in a large severely ill-conditioned problem is worth underlining. In case (b), the use of the nested numeration of the unknowns, the Least Square Log scaling algorithm, and Bi-CGSTAB preconditioned with ILUT allows for a very fast (101 iterations), efficient ($T_t = 38.7$ s), and robust solution (relative residual set to 10^{-10}) in a problem with 65703 unknowns and $\Delta t < \Delta t_{crit}$. This is far superior to the computational performance of the most recent and efficient direct and partitioned solvers experimented with on the same problems [Pini *et al.*, 2002; Gambolati *et al.*, 2002].

Chapter 2

Deformation monitoring of productive gas/oil reservoirs

In situ compaction measurements by radioactive markers represent a promising technique for a most realistic evaluation of the actual mechanical properties of producing gas/oil fields. As is at present implemented by Schlumberger and Western Atlas, the marker technique is reported to have a nominal accuracy equal to 1 mm for the compaction measurement of a 10.5 m wide interval. Some recent surveys in the Northern Adriatic wellbores equipped with radioactive markers exhibit unexpected expansion results, which do not allow for a straightforward interpretation and use of marker data in order to estimate the vertical uniaxial compressibility of the monitored strata. The present chapter provides a review of the radioactive marker technology and its use for the derivation of a rock constitutive law. Some results obtained by the marker surveys performed on three wellbores in the Northern Adriatic Sea are presented and discussed, emphasizing the difficulties arising in the datum interpretation. Finally the basic deformation mechanisms in producing reservoirs are investigated by means of analytical models, showing that stratified geological structures, as is typically the case in sedimentary basins, may naturally involve rock expansions during production.

2.1 Introduction

A realistic evaluation of the actual mechanical properties of soils and rocks under variable stress conditions is of paramount importance in order to provide a reliable prediction of the corresponding deformation. This is particularly relevant in problems where numerical

modeling appears to be the basic tool for providing answers in terms of future developments, as in estimating the potential impact that fluid (gas, oil or water) extraction from deep reservoirs may exert on land stability. In particular, knowing the mechanical parameters of rock for use in subsidence models is one of the key factors both in controlling the phenomenon and in planning gas/oil field production.

The deformation characteristics of soils and rocks can be evaluated by two different procedures. The first is based on laboratory experiments performed on representative soil samples undergoing particular stress and strain paths. The second relies on in situ measurements of reservoir compaction due to fluid extraction and hence related to the corresponding decline in pore pressure. However, the measurements recorded at the Groningen gas reservoir [Pottgens and Browner, 1991; NAM, 1995] and at several Northern Adriatic fields [Cassiani and Zoccatelli, 2000] suggest that subsurface mechanical properties obtained by in situ compaction monitoring may differ substantially from the outcome of lab tests. The rock compressibility estimated by in situ techniques is generally smaller, even by one order of magnitude [Cassiani and Zoccatelli, 2000], than the laboratory results.

Although possible reasons for error with in situ deformation monitoring, based on currently-adopted technology, are still a matter of debate [Brighenti *et al.*, 2000], some recent studies [Cassiani and Zoccatelli, 2000; Palozzo *et al.*, 2000] seem to confirm that in situ experiments offer the most reliable estimate available at present of actual rock compressibility. This is mainly due to the preservation of the in situ stress field, from which the lab sample has been removed, and the elimination of any disturbance during coring operations and possible damage due to handling, storage, transportation, and laboratory preparation. It should be realized, however, that in situ measurements of deformation can not be a substitute for laboratory measurements on core material in all circumstances. For instance, in the exploration and design stage of an oil or gas field, in situ measurements are not possible.

One of the most promising techniques for in situ reservoir compaction monitoring relies on the use of weakly radioactive markers [De Loos, 1973; Mobach and Gussinklo, 1994]. The radioactive marker technique is based on the regular monitoring of the distances between a number of low-emission isotopes (usually ^{137}Cs or ^{60}Co) shot at fixed intervals along the wall of a generally non-productive vertical well. The location of each bullet after the porous medium has deformed is obtained by drawing a specific tool provided with gamma-ray detectors up through the well from the bottom. As currently implemented by Schlumberger and Western Atlas, the vertical deformation measurements have a nominal accuracy of 1 mm per 10.5 m, which is the initial interval between two consecutive

radioactive sources. The marker technique has been used successfully, for instance, in the Ekofisk field, North Sea [Menghini, 1989], in the Groningen gas field [Mobach and Gussinklo, 1994], in the Champion oil field off Brunei [Schmitt, 1996], and in several wells in the Northern Adriatic Sea [Cassiani and Zoccatelli, 2000; Baù *et al.*, 2002].

In some cases, unexpected results seem to emerge from the marker measurements, however, such as rock expansions with an overall decline in pore pressure within the monitored intervals [Baù *et al.*, 2001], which can prevent these data from being used to obtain a realistic evaluation of subsurface mechanical properties. A detailed investigation of the factors giving rise to such results, such as instrument inaccuracy, procedural errors, or a genuinely extensive behavior of the rock, is of paramount importance for the proper interpretation of marker measurements and a reliable modeling of future land subsidence.

The present chapter gives a detailed description of the radioactive marker technique and the use of reservoir compaction measurements for estimating subsurface mechanical properties. Some sets of measurements recently obtained in three wellbores in the Northern Adriatic basin are analyzed and the unexpected expansion data are emphasized. The simplified poro-elastic model developed by Geertsma [1966, 1973a] is then used to grasp the basic mechanisms characterizing reservoir behavior during fluid extraction. Finally, there is a conclusive discussion on the application of the marker technique to in situ reservoir compaction monitoring.

2.2 The radioactive marker technique

The radioactive markers are usually located at fixed intervals along a vertical non-productive well in the vicinity of one or more compacting units (Figure 2.1). The spacing between two consecutive markers is approximately 10.5 m and is dictated by the geometry of the logging tool, as explained later on. The radioactive sources are incorporated into bullet-shaped leak-proof steel containers in order to avoid environmental contamination problems. The strength of the source (^{137}Cs or ^{60}Co) ranges between 150 and 300 μCurie, depending on the diameter of the hole. The bullets are shot along the well wall by means of a perforator gun, using an explosive charge that varies according to the stiffness of the formation and conditions of the borehole. It is very important to select the right charge because the marker must lie neither too deep in the rock (to avoid detection problems), nor too shallow (to avoid possible disturbances due to the casing set).

We indicate the $i-$spacing between two consecutive markers as h_i. Once the markers have been installed, the initial $h_{i,0}$ values are measured. At time t, the $h_{i,t}$ values are

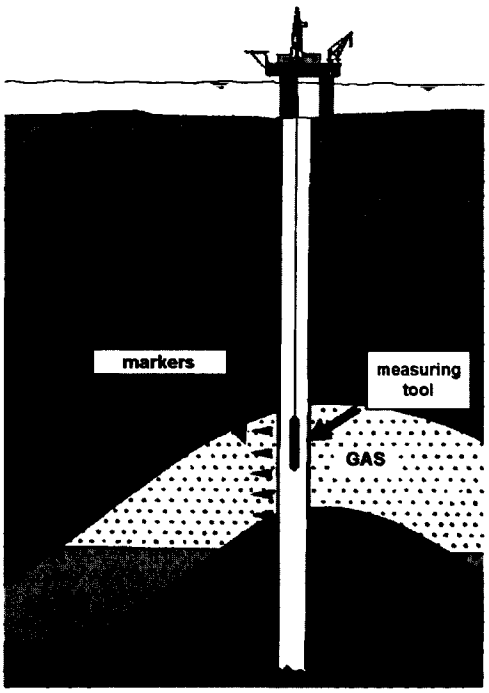

Figure 2.1: Schematic representation of the radioactive marker technique.

recorded and compared with the initial values, so that:

$$\Delta h_{i,t} = h_{i,t} - h_{i,0}$$

is the compaction/expansion of the $i-$spacing. The markers' position is detected by specific logging tools developed by Schlumberger (Formation Subsidence Monitoring Tool, FSMT) and Western Atlas (Compaction Monitoring Instrument, CMI).

The logging tool is schematically illustrated in Figure 2.2a. It is equipped with 4 $\gamma-$ray detectors, a vertical accelerometer to adjust for irregular movements, and a robust stainless steel housing specifically designed to make the tool insensitive to pressure and temperature variations. The tool moves from the bottom of the well upwards at a constant velocity and the maximum signal from each detector is recorded when the detector is right opposite the marker (Figure 2.2b). Note that the signal is recorded vs time, but its conversion into a spatial value, i.e. distance from the lowest detector, is straightforward due to the tool's constant speed. The logging speed usually ranges between 1.5 and 3 m/min, and data are collected at 0.1 inch intervals.

The $\gamma-$ray detectors are numbered 1, 2, 3 and 4 from top to bottom, as shown in Figure 2.2a, while their relative distances l_{jk} are summarized in Figure 2.2c. Consider a generic pair of markers. Since the expected compaction is of the order of a few millimeters, the first peak is usually recorded by detector 1 and relates to the upper marker, while the second peak is recorded by detector 3 and relates to the lower marker. Denoting the difference in depth between the peaks recorded by detector 1 and 3 for spacing i as $d_{13,i}$, the h_i value is calculated as (Figure 2.2):

$$h_i = l_{13} - d_{13,i} \tag{2.1}$$

Equation (2.1) is simply generalized as follows:

$$h_i = l_{jk} - d_{jk,i} \qquad j = 1,2 \quad k = 3,4$$

Note that four h_i values per interval are obtained, so the final h_i is computed as an arithmetic average. In general, more than one logging pass is performed, so the average length of the $i-$spacing evaluated in run r is:

$$h_i^{(r)} = \frac{1}{n_i^{(r)}} \sum_j \sum_k \left(l_{jk} - d_{jk,i}^{(r)} \right) \qquad j = 1,2 \quad k = 3,4 \tag{2.2}$$

where $n_i^{(r)}$ is the number of estimates accepted in each run, varying between 1 and 4 according to the reliability of $d_{jk,i}^{(r)}$ measurements. The final marker spacing length at time t is obtained as the average $\overline{h_{i,t}}$ of R different runs, with the corresponding standard deviation $\sigma_{i,t}$ calculated as:

$$\sigma_{i,t} = \sqrt{\frac{\sum_{r=1}^{R} \left(h_{i,t}^{(r)} - \overline{h_{i,t}} \right)^2}{R-1}} \tag{2.3}$$

The key factor for achieving the target accuracy of 1 mm per 10 m is the correct determination of marker position from the signal profile (Figure 2.2b). Several numerical techniques are currently available for interpreting the recorded signal, such as the "peak method", which locates the marker at the peak $\gamma-$ray value, the "midpoint method", where the bullet's location is defined as the midpoint of a depth interval between two $\gamma-$ray threshold values, the "area method", which determines the marker position as the point which halves the area under the signal curve, and several others. For a thorough review, see Macini and Mesini [2000]. An increasingly popular technique is based on determining the peak point by means of an appropriate curve fitting. A good choice may be to use a modified Gaussian function such as:

$$G(y) = b + he^{-y^2} \left[1 + sH_3(y) \right] \tag{2.4}$$

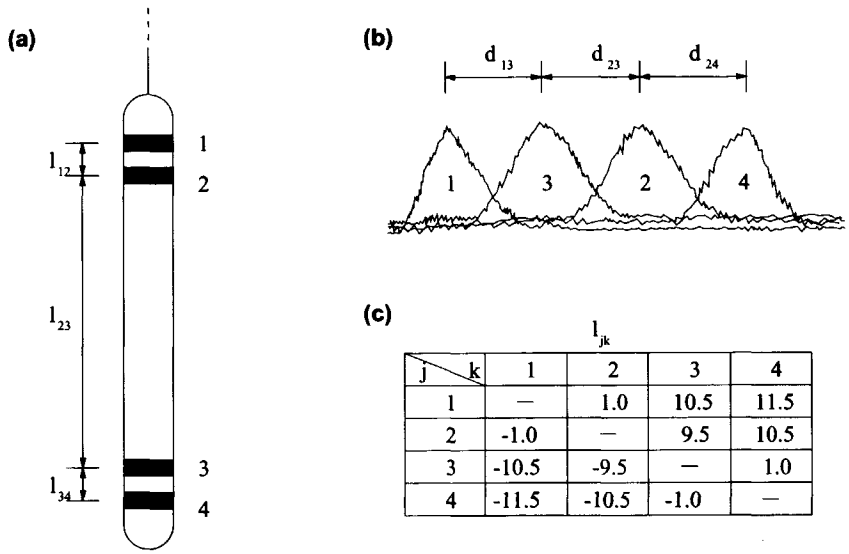

l_{jk}

j \ k	1	2	3	4
1	—	1.0	10.5	11.5
2	-1.0	—	9.5	10.5
3	-10.5	-9.5	—	1.0
4	-11.5	-10.5	-1.0	—

Figure 2.2: (a) Schematic representation of a 4-detector logging tool; (b) γ−ray signal recording by detectors 1, 2, 3, and 4; (c) tool dimensions.

where b is the background formation radioactivity, h is the level of the radioactive marker source, s is the amount of asymmetry (skewness) of the real signal profile, which is modeled by means of the 3rd Hermite polynomial H_3, and y determines the marker's depth. The advantages of curve fitting using equation (2.4) are that it uses all the data points, not only a subset, and that it accounts for skewness.

A number of errors may affect $h_i^{(r)}$ determination, including systematic and random errors. The most common systematic error is the incorrect determination of the distances l_{jk} between the detectors. To avoid this, the tool must be accurately calibrated at the baseline so as to keep the l_{jk} uncertainty below 1 mm. Systematic errors can simply be recognized, however, as they affect all the measurements in the same way. Random errors occasionally occur during the logging pass and include irregular tool movements, cable stretch, anomalous speed variations, friction between cable and casing. Sometimes, the main source of error lies in the determination of the signal profile peak, which may be somewhat difficult to identify because of the low radioactive emission of certain kinds of marker. A simple way to estimate possible random errors during the $h_i^{(r)}$ measurement is to calculate:

$$\epsilon_{12,i}^{(r)} = d_{12,i}^{(r)} - l_{12}$$

$$\epsilon_{34,i}^{(r)} = d_{34,i}^{(r)} - l_{34}$$

Theoretically, $\epsilon_{12,i}^{(r)}$ and $\epsilon_{34,i}^{(r)}$ should be zero. In practice, $d_{jk,i}^{(r)}$ measurements leading to $\epsilon_{12,i}^{(r)}$ or $\epsilon_{34,i}^{(r)}$ larger than 1 mm are empirically corrected by the factor:

$$f_i^{(r)} = \frac{l_{12} + l_{34}}{d_{12,i}^{(r)} + d_{34,i}^{(r)}}$$

or excluded from the computation.

2.2.1 Uniaxial compressibility from marker measurements

Thin gas/oil reservoirs mainly compact in the vertical direction with a negligible lateral deformation [Gambolati *et al.*, 1999b], so the vertical compaction at time t of the $i-$th depth interval with initial length $\overline{h_{i,0}}$ is:

$$\Delta h_{i,t} = c_{M,i}\overline{h_{i,0}}\Delta\sigma_{z,i,t} \tag{2.5}$$

where $\Delta h_{i,t}$ is the difference between $\overline{h_{i,t}}$ and $\overline{h_{i,0}}$, $c_{M,i}$ is the medium uniaxial compressibility in the $i-$spacing, and $\Delta\sigma_{z,i,t} = \sigma_{z,i,t} - \sigma_{z,i,0}$ is the vertical effective stress variation in the $i-$spacing during the monitored time interval. As long as there is no abrupt increase in the stiffness of confining rocks, $\Delta\sigma_{z,i,t}$ practically equates the fluid pore pressure variation $\Delta p_{i,t}$, which is positive with a pressure rise (i.e. natural recovery or fluid injection from outside) and negative with a decline (i.e. fluid withdrawal). The estimation of average pore pressure variation within the deforming intervals is calculated using static reservoir pressure measurements taken at each logging time of the marker intervals.

The uniaxial compressibility of the $i-$spacing is readily derived from equation (2.5):

$$c_{M,i} = \frac{\Delta h_{i,t}}{\overline{h_{i,0}}\Delta p_{i,t}} \tag{2.6}$$

The vertical deformation $\Delta h_{i,t}$ is affected by the uncertainty of $\overline{h_{i,0}}$ and $\overline{h_{i,t}}$ measurements. Denoting the related variance by $\sigma_{i,0}^2$ and $\sigma_{i,t}^2$ (eq. (2.3)), the empirical variance of $\Delta h_{i,t}$ is:

$$\sigma_{\Delta h_{i,t}}^2 = \sigma_{i,0}^2 + \sigma_{i,t}^2$$

and thus the standard deviation associated with $c_{M,i}$ can be computed as:

$$\sigma_{c_{M,i}} = \frac{\sigma_{\Delta h_{i,t}}}{\overline{h_{i,0}}\Delta p_{i,t}} \tag{2.7}$$

where $\Delta p_{i,t}$ is assumed to be a deterministic value.

The uniaxial compressibilities evaluated in a monitoring well by the above-described procedure (eq. (2.6)) may be quite scattered, due to the different uncertainties affecting each measurement. As we know from elementary statistics [Hald, 1952], the standard deviation of the mean of a data set reduces if the data are clustered together, and generally decreases with the size of the cluster. A statistical method used to cluster the compressibility values is the moving average method. Denoting the cluster size of the moving averages (called window size) as w, the average compressibility of the $k-$th cluster in a well monitored by N_s spacings is computed as:

$$\overline{c_M}_{,k} = \frac{\sum_{i=k}^{k+w-1} a_i c_{M,i}}{\sum_{i=k}^{k+w-1} a_i} \qquad k = 1, \ldots, N_s - w + 1 \tag{2.8}$$

with the weights a_i calculated as [Hald, 1952]:

$$a_i = \frac{1}{\sigma^2_{c_{M,i}}}$$

and $\sigma^2_{c_{M,i}}$ given by equation (2.7). The standard deviation associated with $\overline{c_M}_{,k}$ is:

$$\sigma^2_{\overline{c_M}_{,k}} = \frac{1}{\sum_{i=k}^{k+w-1} a_i}$$

The compressibility data obtained from equation (2.8) can be used to model the constitutive behavior of the monitored formations. Since the total vertical stress $\hat{\sigma}_z$ is known from density logging data, each $\overline{c_M}_{,k}$ can be associated to the corresponding average effective stress [Baù *et al.*, 1999]:

$$\overline{\sigma_z}_{,k} = \frac{\sum_{i=k}^{k+w-1} \overline{h}_{i,0} \left(\hat{\sigma}_{z,i} + p_{i,0} + 0.5\Delta p_{i,t}\right)}{\sum_{i=k}^{k+w-1} \overline{h}_{i,0}} \qquad k = 1, \ldots, N_s - w + 1 \tag{2.9}$$

where $\hat{\sigma}_{z,i}$ is computed at the midpoint of $i-$spacing and the effective stress at the midpoint of the time interval. The compressibility values (2.8) are ultimately regressed versus σ_z (eq. (2.9)) to obtain a representative constitutive relationship for the monitored rock formations. According to the pore pressure variation (decline or rise) experienced in the productive layers, uniaxial compressibility estimates can be obtained in virgin loading or unloading-reloading conditions [Baù *et al.*, 2002].

2.2.2 Deformation monitoring in the Northern Adriatic basin, Italy

Five offshore boreholes in the Northern Adriatic Sea were recently equipped with radioactive markers to monitor the field compaction due to gas production. The position of the markers is determined with both FSMT and CMI logging tools and the wells are periodically surveyed every 2 or 4 years. The outcome of marker surveys from three boreholes was used to derive a basin-scale constitutive law in virgin loading and unloading-reloading conditions for the Northern Adriatic basin [Baù *et al.*, 2002]. Since many reservoirs are located close to the coast, gas extraction may have a strong impact on shoreline configuration [Gambolati *et al.*, 1999a], so the use of realistic subsurface geomechanical properties as input parameters in numerical models is essential to a reliable land settlement prediction. The marker measurement interpretation is not always straightforward, however, and numerous uncertainties may affect its accuracy and reliability.

Tables 2.1 through 2.3 show the outcome of marker surveys performed between 1992 and 1999 in three wellbores in the Northern Adriatic Sea. The measured deformations Δh_i are represented graphically in Figure 2.3, emphasizing the reliability interval (i.e. the standard deviation) of each value and the relative position with respect to the productive layers. A number of intervals, especially in wells 2 and 3, exhibit an unexpected expansion despite a reported pore pressure decline, while in other cases compactions with zero Δp are recorded. These experimental values do not allow to use equations (2.5) and (2.6) since a negative or infinite uniaxial compressibility would result. Hence such measurements cannot be used in the procedure illustrated in the previous section, thus reducing the data available for deriving reliable constitutive laws for the rock. However, the observed deformations could be correct and indeed related to a real local rock mechanical behavior, as will be shown later. Moreover, equation (2.6) is based on the assumption that the deformation is likely to occur mainly in the vertical direction with negligible lateral displacements, as it is simulated in an oedometer. If horizontal pore pressure gradients toward the wellbore take place, as is the case when the wellbore is productive, a horizontal strain may be generated which opposes the vertical compaction, thus leading to an underestimate of the measured uniaxial compressibility.

In order to assess the reliability of in situ radioactive marker measurements for a realistic evaluation of the mechanical properties of productive gas/oil fields, it appears to be of paramount importance to investigate the deformation mechanisms occurring during the development of gas reservoirs embedded in the stratifications of the Northern

spacing	depth (m)		$\Delta h_{i,92-96}$	$\sigma_{\Delta h_{i,92-96}}$	$\Delta p_{i,92-96}$
i	upper marker	lower marker	(mm)	(mm)	(MPa)
1	2748	2759	+0.7	0.62	–
2	2759	2770	-3.7	3.50	-0.8
3	2770	2781	-1.9	2.90	-1.0
4	2781	2791	-4.0	1.00	-1.0
5	2869	2880	-7.2	1.50	-9.4
6	3230	3240	-8.9	0.81	-4.7
7	3240	3251	-5.0	0.41	-5.1
8	3251	3261	-1.1	0.61	-1.8
9	3348	3359	-11.5	0.35	-20.5
10	3359	3369	-7.1	0.79	-8.2
11	3369	3380	-8.0	0.40	-4.9
12	3380	3390	-3.7	0.47	-3.1
13	3390	3401	+1.6	0.33	-2.2
14	3401	3411	-1.7	0.72	-0.3
15	3449	3460	-19.1	0.59	-23.8
16	3460	3470	-17.5	0.81	-23.5
17	3470	3481	-11.5	0.65	-13.4
18	3502	3512	-10.4	0.52	-18.7
19	3512	3523	-9.5	0.61	-19.2
20	3523	3534	-1.9	0.67	-10.6
21	3647	3657	-7.1	0.69	-2.8
22	3657	3667	-5.7	0.44	-2.8
23	3667	3678	-1.4	0.65	-2.9
24	3678	3688	-5.1	0.79	-2.0
25	3688	3699	-2.7	0.79	-2.0
26	3699	3710	-1.4	0.70	-2.0
27	3710	3720	-0.3	0.54	–
28	3720	3730	-4.4	0.89	-2.4

Table 2.1: Marker measurements and corresponding pore pressure variation in well 1 during the period 1992-1996.

spacing	depth (m)		$\Delta h_{i,94-96}$	$\sigma_{\Delta h_{i,94-96}}$	$\Delta p_{i,94-96}$
i	upper marker	lower marker	(mm)	(mm)	(MPa)
1	1040	1051	-0.4	1.58	–
2	1051	1061	+3.3	–	–
3	1061	1072	-25.1	–	–
4	1072	1082	-43.9	2.97	-0.3
5	1082	1093	-10.4	2.66	-0.3
6	1093	1103	+0.8	–	-0.2
7	1103	1114	-1.9	1.54	-0.3
8	1113	1124	-12.7	–	-0.6
9	1149	1160	+3.7	–	-0.6
10	1160	1170	+2.6	1.34	–
11	1170	1181	-2.1	1.53	-0.2
12	1181	1191	-10.9	1.58	-0.9
13	1191	1201	+17.7	0.94	-1.7
14	1201	1212	+16.8	1.66	-1.3
15	1212	1222	-14.9	1.61	-0.2
16	1222	1233	+5.3	–	-0.5
17	1233	1243	+14.0	1.68	-0.9
18	1243	1254	-10.5	1.36	-0.9
19	1254	1264	+12.7	1.19	-0.5
20	1264	1275	-4.0	1.17	-1.5
21	1320	1330	+7.4	1.80	-0.8
22	1330	1341	-23.0	1.81	-1.0
23	1341	1351	-6.1	2.21	-1.0
24	1351	1362	-8.4	1.89	-1.0
25	1362	1372	+5.4	2.58	-1.1
26	1372	1383	-5.2	1.36	-1.1
27	1383	1393	-1.4	0.81	-1.1
28	1393	1404	+6.2	1.17	-2.0
29	1404	1414	-5.6	2.26	-0.9
30	1414	1425	+2.0	3.00	-0.9

Table 2.2: Marker measurements and corresponding pore pressure variation in well 2 during the period 1994-1996.

spacing	depth (m)		$\Delta h_{i,96-99}$	$\sigma_{\Delta h_{i,96-99}}$	$\Delta p_{i,96-99}$
i	upper marker	lower marker	(mm)	(mm)	(MPa)
1	2955	2977	+5.6	2.70	–
2	2977	2987	+2.6	0.88	–
3	2987	2998	-3.0	0.88	–
4	2998	3019	-43.9	3.20	-0.3
5	3019	3029	0.0	0.94	-0.1
6	3029	3040	+1.6	0.50	–
7	3040	3051	+2.8	1.10	–
8	3051	3071	-11.1	1.70	–
9	3071	3082	+1.5	0.73	–
10	3082	3103	+13.4	2.90	–
11	3103	3114	+1.2	0.63	–
12	3114	3124	+1.3	0.72	-2.3
13	3187	3208	+36.2	4.50	–
14	3208	3219	-0.5	1.10	–
15	3219	3229	+2.9	0.73	–
16	3229	3240	+2.7	0.87	–
17	3240	3250	-2.7	0.66	–
18	3250	3261	-5.3	0.92	–
19	3261	3270	+5.6	1.10	–
20	3270	3278	+10.5	0.80	–
21	3278	3287	-10.7	0.79	–
22	3287	3303	+1.8	2.50	-7.0
23	3303	3324	+0.7	3.90	-12.3

Table 2.3: Marker measurements and corresponding pore pressure variation in well 3 during the period 1996-1999.

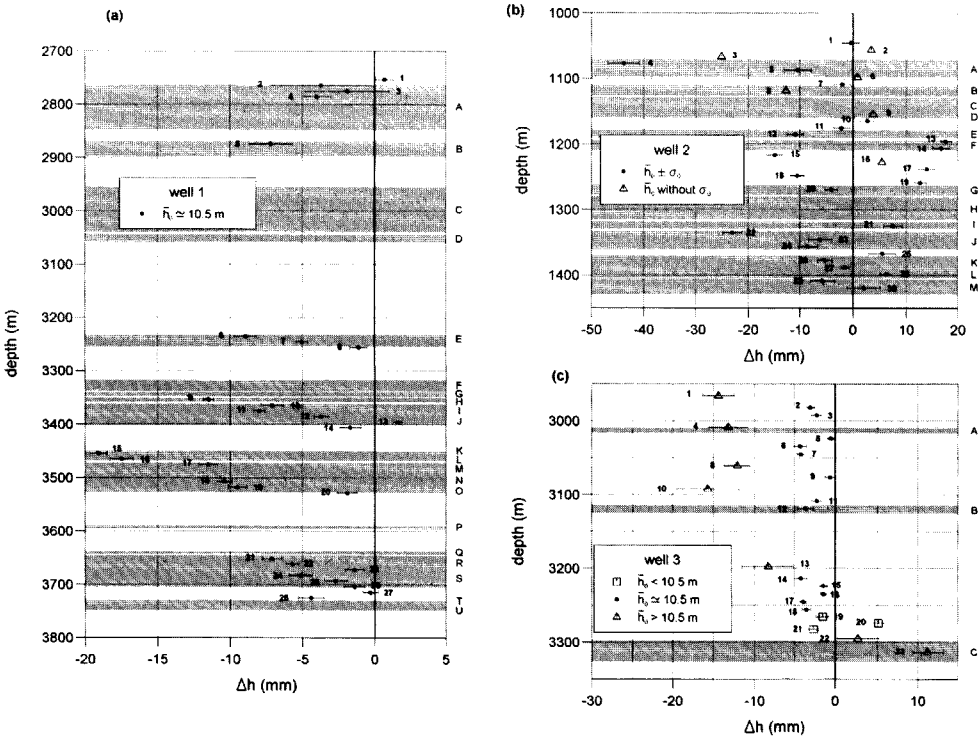

Figure 2.3: Marker measurements referred to the midpoint of each interval for (a) well 1, 1992-1996; (b) well 2, 1994-1996; (c) well 3, 1996-1999. Gray shaded areas correspond to the productive units.

Adriatic sedimentary basin. In fact, one of the main causes of the observed discrepancy can be that equations (2.5) and (2.6) have been derived for a single reservoir layer, while in reality there are a number of pumped reservoirs and their mutual influence should be taken into account. This can be done using simplified theoretical models, such as Geertsma's [1966; 1973a] formulation, and numerical consolidation models, thus taking into account a number of additional factors, e.g. coupling, hydromechanical heterogeneity and 3-D geometry, with a complete picture obtained incorporating the layered structure of the soil and the depletion of various reservoirs.

2.3 Productive reservoir compaction

It is common knowledge that the extraction of subsurface fluids from an underground reservoir causes local changes in the stress and strain field which can be predicted by poro-elastic theory [Biot, 1941]. The analytical solution for a disc-shaped compacting reservoir embedded in a homogeneous elastic half-space bounded by a traction-free surface is given by Geertsma [1966, 1973a] based on the nucleus of strain concept. Though such a solution disregards a number of factors, including the heterogeneity of the porous medium, coupling between stress and flow, and complex 3-D field geometry, it nonetheless represents a very useful tool for grasping the basic deformation phenomena arising from interaction between the compacting reservoir and its surroundings.

According to the nucleus of strain concept, each volume element at a place ξ contributes to the displacement u_i at x in proportion to the fluid pressure p at ξ. So:

$$u_i = \int_V p(\xi)\, u_i^*(x,\xi)\, dV(\xi) \tag{2.10}$$

where u_i^* is the displacement along the $i-$direction at x resulting from a unit pressure at ξ in the volume dV. Thus, the function u_i^* can be considered as the Green function for the displacements and is calculated using the solution suggested by Mindlin and Cheng [1950] in thermoelasticity. Denoting the depth of the nucleus undergoing a unit pressure change as c and the radial distance from it as r, the vertical displacement u_z^* to use in the equation (2.10) is [Geertsma, 1966, 1973a]:

$$u_z^*(r,z) = \frac{c_M}{4\pi}\left\{\frac{z-c}{\left[r^2+(z-c)^2\right]^{3/2}} + \frac{4\nu(z+c)-(z+3c)}{\left[r^2+(z+c)^2\right]^{3/2}} - \frac{6z(z+c)^2}{\left[r^2+(z+c)^2\right]^{5/2}}\right\} \tag{2.11}$$

If the half-space deformation is induced by a spherical cavity contraction, equation (2.11) still holds true with the volume reduction of the cavity $-\Delta V$ substituting c_M. The

quantity ΔV can be expressed as:

$$\Delta V = 4\pi R_0^2 a \tag{2.12}$$

with R_0 the initial cavity radius and a the radial displacement at the cavity boundary. Being the vertical strain inside the cavity $\epsilon_z^{(i)} = -a/R_0$, equation (2.12) can be also written as:

$$\Delta V = -4\pi R_0^3 \epsilon_z^{(i)} \tag{2.13}$$

The vertical strain $\epsilon_z^{(o)}$ outside the cavity is calculated by derivating equation (2.11) with respect to z. In particular, along the axis $r = 0$, $\epsilon_z^{(o)}$ reads:

$$\epsilon_z^{(o)} = \frac{\partial u_z^*(r=0)}{\partial z} = \frac{\Delta V}{2\pi}\left[\frac{1}{|z-c|^3} + \frac{4\nu - 1}{(z+c)^3} - \frac{6z}{(z+c)^4}\right] \tag{2.14}$$

Using equation (2.13) into (2.14) gives the ratio between $\epsilon_z^{(o)}$ and $\epsilon_z^{(i)}$ as a function of z:

$$\frac{\epsilon_z^{(o)}}{\epsilon_z^{(i)}} = -2R_0^3\left[\frac{1}{|z-c|^3} + \frac{(4\nu-1)(z+c) - 6z}{(z+c)^4}\right] \tag{2.15}$$

The main feature of equations (2.14) and (2.15) is that $\epsilon_z^{(o)}$ is always positive, i.e. indicates an extension, and is about twice the absolute value of the strain inside the cavity just above and below the cavity itself. In fact, it can be noted that for $z = c \pm R_0$ the first term in the brackets reduces to $1/R_0^3$, while the second term is negligible since $c \gg R$.

Let us now consider a constant pore pressure change Δp occurring in a disc-shaped volume with a thickness s at a depth c. As long as $s \ll R$, R being the disc radius, the integral (2.10) can be approximated to:

$$u_z(r,z) = s\Delta p \int_0^R \int_0^{2\pi} u_z^*(r,z,\rho,\varphi)\,\rho d\rho d\varphi \tag{2.16}$$

The complete solution to (2.16) leads to Hankel integrals, but along the vertical axis passing through the center of the reservoir ($r = 0$) the expression (2.11) is simpler and the vertical displacement (2.16) reads:

$$\begin{aligned} u_z(0,z) = -\frac{c_M s\Delta p}{2}\Bigg\{ & \frac{z-c}{\sqrt{R^2+(z-c)^2}} - \frac{(3-4\nu)(z+c)}{\sqrt{R^2+(z+c)^2}} + \frac{2zR^2}{\left[R^2+(z+c)^2\right]^{3/2}} + \\ & +3-4\nu+\eta\Bigg\} \end{aligned} \tag{2.17}$$

with $\eta = -1$ for $z > c + s/2$ and $\eta = +1$ for $z < c - s/2$. Using the dimensionless parameters $Z = z/c$ and $C = c/R$, equation (2.17) becomes:

$$u_z(0,z) = -\frac{c_M s \Delta p}{2}\left\{\frac{C(Z-1)}{\sqrt{1+C^2(Z-1)^2}} - \frac{(3-4\nu)C(Z+1)}{\sqrt{1+C^2(Z+1)^2}} + \frac{2CZ}{\left[1+C^2(Z+1)^2\right]^{3/2}} + \right.$$
$$\left. +3-4\nu+\eta\right\} \tag{2.18}$$

The vertical surface displacement over the center of the reservoir, i.e. maximal land subsidence, is readily obtained from (2.18) by taking $Z = 0$.

With the radioactive marker technique, the vertical deformation of a $\overline{h_{i,0}}$ thick rock layer is recorded, i.e.:

$$\Delta h_i = \int_{z_i}^{z_i+\overline{h_{i,0}}} \epsilon_z dz$$

where z_i is the upper marker's depth. The vertical strain inside the reservoir is readily derived as:

$$\epsilon_z^{(i)} = \frac{c_M s \Delta p}{s} = c_M \Delta p$$

while outside the reservoir and over the center of the field it can be obtained as:

$$\epsilon_z^{(o)} = \frac{\partial u_z}{\partial z} = \frac{1}{c}\frac{\partial u_z}{\partial Z}$$

with u_z given by equation (2.18). Differentiating equation (2.18) yields:

$$\epsilon_z^{(o)} = -\frac{c_M s \Delta p}{2R}\left\{\frac{1}{\left[1+C^2(Z-1)^2\right]^{3/2}} - \frac{3-4\nu}{\left[1+C^2(Z+1)^2\right]^{3/2}} + \right.$$
$$\left. + \frac{2\left[1-C^2(Z+1)(2Z-1)\right]}{\left[1+C^2(Z+1)^2\right]^{5/2}}\right\} \tag{2.19}$$

The ratio of $\left|\epsilon_z^{(o)}\right|$ to $\left|\epsilon_z^{(i)}\right|$ depends on s/R and C. In our problems, typically c is comparable to R ($0.2 < C < 2$) and hence the above ratio has the same order of magnitude as s/R, which means that $\left|\epsilon_z^{(o)}\right| \ll \left|\epsilon_z^{(i)}\right|$.

Figure 2.4 shows the outcome of equations (2.18) and (2.19) along a vertical axis passing through the center of the reservoir for different values of C. According to equation (2.18) a positive u_z means land settlement, i.e. subsidence. Note that the reservoir's top subsides for any C, while its bottom rises with $C > 0.46$ and subsides otherwise. $|u_z|$ diminishes as $Z \to 0$, so a positive vertical strain is always predicted in the reservoir's surroundings (Figure 2.4b).

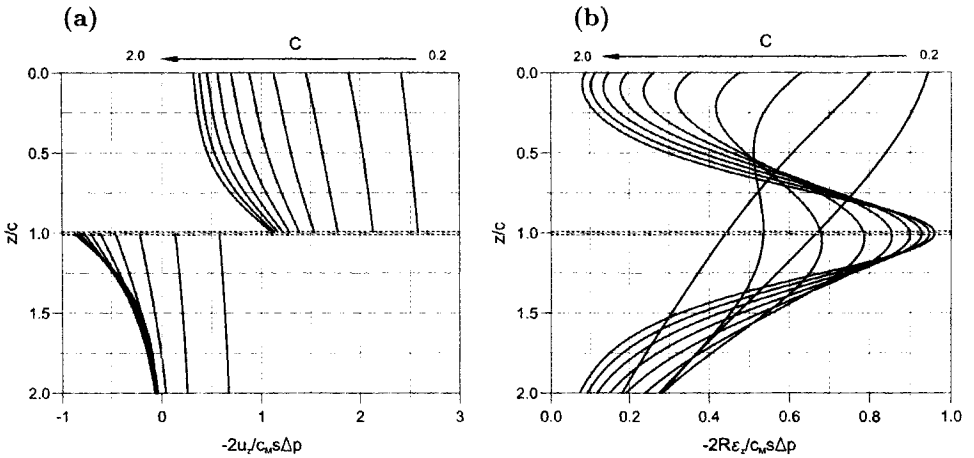

Figure 2.4: Double Geertsma solution for a compacting disc-shaped reservoir with $s/R \ll 1$ over the center of the field: (a) normalized vertical displacement; (b) normalized vertical strain outside the reservoir.

Since $\left|\epsilon_z^{(o)}\right| << \left|\epsilon_z^{(i)}\right|$, the expansion is much smaller than the reservoir compaction. However, if more than one reservoir is developed, the contributions from each single reservoir add and the vertical traction among the productive layers increases. As an example, Figure 2.5 shows $\epsilon_z^{(o)}$ caused by a unit pore pressure decline occurring in two disc-shaped reservoirs ($s = 20$ m, $R = 1000$ m) located at $c = 980$ m and $c = 1020$ m, respectively. Note that the vertical strain nearly doubles in the rock formations between the reservoirs.

In a sedimentary basin such as the Northern Adriatic, Italy, gas fields are typically composed of a number of thin productive sandy formations frequently interbedded with impermeable clay layers and unproductive compacted silts and sands, as shown in Figure 2.3, where the productive reservoirs are shaded in gray. As a consequence, radioactive markers can theoretically be expected to record expansions if the monitored spacing largely includes the unproductive confining rocks. This is particularly true if reservoirs are very thin ($s \simeq 1$ to 2 m) and the vertical distance between two adjacent reservoirs is of the order of 10 m.

2.4 Conclusions

Estimating realistic geomechanical properties of productive gas/oil fields is a key factor for improving the reliability of land subsidence numerical models. In situ reservoir compaction

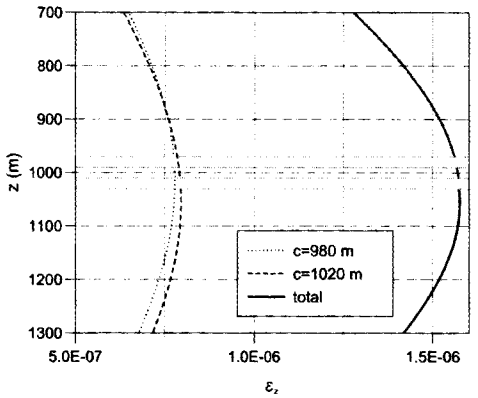

Figure 2.5: Vertical strain $\epsilon_z^{(o)}$ induced by a simultaneous unit pore pressure decline in two reservoirs located at $c = 980$ m and $c = 1020$ m, respectively.

monitoring with radioactive markers represents a promising technique for assessing vertical uniaxial rock compressibility of productive layers. As currently implemented, the marker technique is reported to allow for an accuracy of 1 mm for deformation measurements of 10.5 m wide intervals. However, recent experience in several Northern Adriatic wellbores shows that unexpected measurements may be recorded, such as expansions with zero or declining pore pressure in the monitored strata, which may pose serious problems for the proper interpretation of the corresponding data.

In order to understand the basic rock deformation mechanisms in the vicinity of productive reservoirs, Geertsma's analytical solution was analyzed in a simplified, uncoupled and homogeneous setting, showing that:

- a positive vertical strain above and below the depleted disc-shaped volume occurs;
- for typical field settings with R much larger than s and comparable to c, deformations outside the reservoir are much smaller than inside the reservoir;
- a number of different productive layers increases the magnitude of expansion in the confining and interbedded rock formations;
- markers located just above (or below) a depleted level or between producing layers or including thin depleted reservoirs can compact only partially or even expand depending on the actual litho-stratigraphic sequence of the monitored depth interval.

Productive fields in the Northern Adriatic basin are typically composed of a series of thin sandy gas-bearing formations interbedded with impermeable clay and silt layers. As

a result, incorrect marker placement - largely including unproductive and impermeable rocks - may lead to reduced compaction or expansion measurements that cannot be used for uniaxial compressibility estimation.

Chapter 3

Geological and geomechanical setting of the Northern Adriatic basin, Italy

The detailed characterization of geological and hydro-geomechanical properties of the study area is of paramount importance to provide the most reliable interpretation of local rock deformation measurements. For the Northern Adriatic basin, Italy, a fairly large database is currently available by means of extensive reconnaissance studies, wellbore drillings, and laboratory tests on sample cores performed over the last 30 years. Recently, significant advances have been made through the use of more sophisticated technologies, such as electrical log analyses and their statistical interpretation. The present chapter provides an overview of the current knowledge of the Northern Adriatic geology together with a summary of the available geomechanical and hydraulic properties of deep reservoir rocks. In particular, some typical litho-stratigraphic sequences are described with the aid of electrofacies analyses. Then, a basin-scale constitutive relationship both in virgin load and in unloading-reloading conditions is derived based on the radioactive marker surveys performed over the last decade by ENI-Divisione Agip. Finally, some hydraulic properties are given for the sandy productive formations. The data presented in this chapter will be used for the accurate numerical reproduction of the real deep rock behavior in the vicinity of a marker borehole.

3.1 Introduction

The interpretation of radioactive marker data may not be straightforward, especially for a reliable estimate of uniaxial compressibility. An example of anomalous measurements

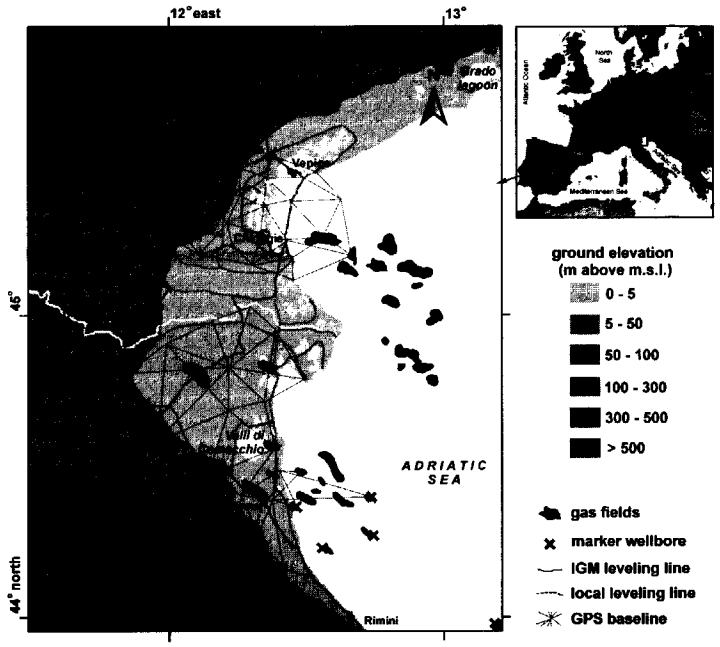

Figure 3.1: Map of the Northen Adriatic basin, showing the trace of some major gas fields discovered in this area, together with the location of marker boreholes and the leveling and GPS networks established for land subsidence monitoring.

was discussed in the previous chapter, with reference to the marker surveys performed by ENI-Divisione Agip, the Italian national oil company, in Northern Adriatic boreholes. The theoretical argument developed in chapter 2 suggests that it may be difficult to use marker data for a mechanical characterization of deep reservoirs, especially in heterogeneous sedimentary basins, where the gas-bearing formations are frequently interbedded with low permeable shale layers and exhibit a local heterogeneity over a scale smaller than the marker spacing. It thus becomes essential to know the geological setting and have highly-detailed litho-stratigraphic sequences available on the monitoring borehole in order to ensure a most reliable interpretation of in situ deformation measurements.

A number of reconnaissance studies and drillings have been performed in the last decades to gain a detailed knowledge of the Northern Adriatic's geological structure. The Northern Adriatic is an epicontinental normally consolidated and pressurized basin, originating from the deposition of clastic Pliocene-Quaternary sediments after the uplift of the Alpine and Apennine ranges. The sedimentary sequence was laid in different

environments (littoral and marine in the lower zone, continental and lagoonal in the upper one) and consists of alternating sand, silt and clay layers interbedded with all possible mixtures of these lithologies. A considerable number of gas fields has been discovered by ENI-Divisione Agip at a burial depth ranging between 1000 and 4500 m. The trace of some of the major fields is shown in Figure 3.1. The gas-bearing formations are mostly located in the pre-Quaternary basement and consist mainly of thin sandy layers ($\sim$ 1 to 10 m thick) with no cementing materials, with the caprock made of shale beds often less than 1 m thick [Marsala *et al.*, 1994].

A large database of the main geo-hydro-mechanical properties of Northern Adriatic geological formations is currently available from extensive explorations and monitoring surveys performed in recent years with a view to developing subsurface resources. Results of laboratory tests for estimating rock mechanical properties [Ricceri and Butterfield, 1974; Brignoli and Figoni, 1995; Gambolati *et al.*, 1998] are given together with measurements obtained from in situ compaction monitoring [Baù *et al.*, 1999; Cassiani and Zoccatelli, 2000]. Recently, new advanced surveying technologies, such as 3D seismic analyses [AGIP, 1996], and lithological, electrical and porosity well-logs [Marsala *et al.*, 1994], have been used by ENI-Divisione Agip to gain a detailed knowledge of the stratigraphic sequence with the related properties encountered in the wellbore drillings for water and gas/oil production. Since the early years of the last century, geodetic leveling lines have been established and continuously improved by both national (IGM, Military Geographic Institute) and local agencies over the eastern area of the Po plain, in order to measure ground surface settlement [Bondesan *et al.*, 1997; Tosi *et al.*, 2000]. These leveling lines are currently integrated with a GPS network [Bitelli *et al.*, 2000] which allows for further improvements in the geodetic surveys (see Figure 3.1). This huge amount of data can be used for a more realistic evaluation of the deep compaction of depleted formations and resulting land settlement as well.

The present chapter gives a detailed description of some significant features of the study area, including the most reliable values for the mechanical and hydraulic rock parameters. These data will subsequently be used for a realistic modeling of flow, stress, and strain fields developing in the vicinity of vertical monitoring boreholes in the Northern Adriatic basin during reservoir depletion. After a few comments on the basin's geology and hydrocarbon occurrence, some stratigraphic sequences resulting from well-log analyses by the electrofacies technique are presented and discussed. A reliable mechanical characterization of deep rock formations is developed using both laboratory and in situ measurements, leading to a basin-scale compressibility law for both virgin loading and

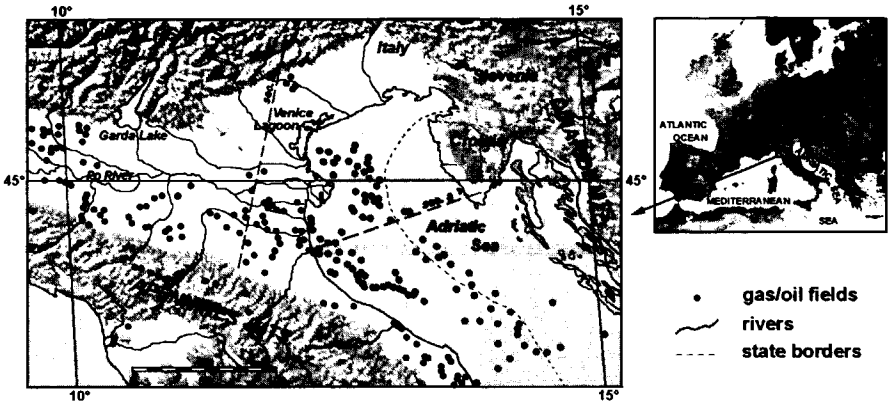

Figure 3.2: The Po River plain and Northern Adriatic basin with the location of gas/oil fields.

unloading-reloading conditions. The most significant hydraulic properties of different recurrent lithotypes are summarized, defining equivalent horizontal and vertical permeability coefficients to describe the behavior of highly heterogeneous layers. Finally, a few comments are provided on the availability and reliability of the geo-hydro-mechanical parameters required for the realistic modeling of Northern Adriatic boreholes.

3.2 Geological setting and petroleum occurrence

The Northern Adriatic basin is located between latitude 43°-46° North and longitude 12°-15° East, and is bounded by the Alps to the north, the Apennine Ranges to the south, and the Dinaride Mountains to the east (Figure 3.2). The sedimentary deposition started in conjunction with the Alpine and Apennine orogenies in the Cenozoic, about 70-80 million years BP and the generation of the Po River drainage system [Haan and Arnott, 1991]. The total sedimentary column ranges from a minimum of 4-5 km at the northern Alpine border to a maximum of approximately 12 km along the Apennine thrust front [Mattavelli *et al.*, 1983]. As an example, two structural cross-sections showing the basic sedimentary sequence of the Northern Adriatic basin are shown in Figure 3.3.

From bottom to top, the main stratigraphic sequence can be summarized as follows [Dondi *et al.*, 1985]:

- Mesozoic limestone basement;

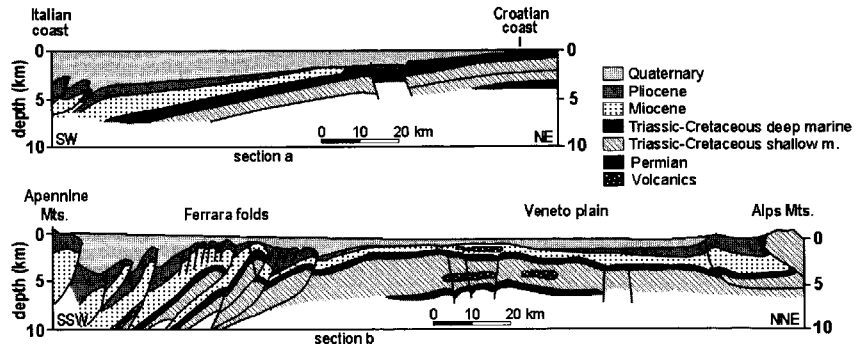

Figure 3.3: (a) Off-shore and (b) on-shore structural cross-section of the Northern Adriatic basin (after Anelli *et al.* [1996]). Section lines are shown in Figure 3.2.

- Eocene-Oligocene and Miocene formations, with alternating marl and limestone;
- Pliocene sediments, overlain by the confining shale bed known as "Argille del Santerno";
- Quaternary sands and clays, known as "Sabbie di Asti".

Above the "Argille del Santerno", the "Sabbie di Asti" were deposited mainly in a shallow sea or delta environment and consist of sand, silt, and clay, with a smooth transition from one lithotype to another. Peat deposits can be found near the top of the Quaternary formation, thus indicating a shallow marine or littoral depositional environment.

Exploratory wells in the Northern Adriatic basin have been drilled since the last decade of the 19th century. To date, approximately 260 gas/oil fields (Figure 3.2) have been discovered [Petroconsultants, 1996]. About 75% of the hydrocarbons detected in this area are Pliocene and Pleistocene biogenetic/diagenetic gases generated in geological traps with high sedimentation rates and a relatively cool thermal regime ($< 60°C$), where bacteria can still survive and the organic material does not degrade. Such conditions occurred especially during the deposition of Pliocene and Pleistocene turbidites, north-east and parallel to the present Apennine Range, near and just off the present Adriatic Italian coastline (see Figure 3.2). Biogenetic gas has been found down to 4500 m [Mattavelli *et al.*, 1983]. At present, the thermal gradients of the area are still low, ranging from 19 to 25 °C/km [Mattavelli and Novelli, 1990].

The gas-bearing rocks range from silty to fine-grained sandstones, but the key feature of these reservoirs is that gas accumulation occurs in multi-pay formations with a thickness

varying from a few centimeters to several dozen meters. The average reservoir porosity is about 25-30%, with a permeability varying from 5 to 1000 mD and water saturation from 35 to 75%. The net-to-gross ratio is estimated to be about 27% in silty formations and 95% in coarser sands. Usually, reservoir caprocks consist of deep-marine and impermeable shale sometimes less than 1 m thick [Mattavelli *et al.*, 1991].

3.2.1 Well litho-stratigraphic sequencing by electrofacies

One of the most important and intensive tasks required by the petroleum industry is the correct identification of the stratigraphic sequence drilled along a borehole. The recent development of sophisticated automatic log tools has almost replaced the direct, often hotly-debated, identification of lithologies from sample cores with the automated correlation between electric signals and lithotypes. First, log-response patterns are associated with the corresponding lithological sequences by preliminary tests on sample cores, thus building up a reference database; then, an automated pattern-recognition device linking tool response with rock properties is used, typically adopting curve-fitting techniques to screen out statistical noise on the recorded signal. The use of statistical interpretation methods allows for an estimation of the uncertainty related to a lithotype's identification. This basic concept for lithofacies analysis was set out by Serra and Abbott [1982], who coined the term "electrofacies" for the above procedure. The automated electrofacies method was originally introduced by Wolff and Pelissier-Combescure [1982]. For more details on the origins and current developments of electrofacies, see Doventon and Prensky [1992].

In the Northern Adriatic boreholes, ENI-Divisione Agip has performed extensive electrofacies analyses with SHDT (Stratigraphic High Resolution Dipmeter Tool) and EATT (Electromagnetic Attenuation Propagation Tool) logs. The former provides microresistivity measurements while the latter relates the fluid content (and hence porosity) to the attenuation of an electromagnetic wave. Examples of litho-stratigraphic sequences obtained with electrofacies are shown in Figures 3.4, 3.5, and 3.6, for wells 1, 2 and 3, respectively. Each log analysis is represented by a specific set of lithotypes, preliminarily identified from sample cores. Every facies is also characterized by a porosity (estimated by EATT) and an intrinsic permeability (estimated from laboratory rock samples) value.

Each litho-stratigraphy exhibits a pronounced heterogeneity at the radioactive marker resolution scale, i.e. 10.5 m. Well 1's sedimentary sequence is characterized mainly by relatively thick heterogeneous sandy permeable units (up to a few dozen meters) incorpo-

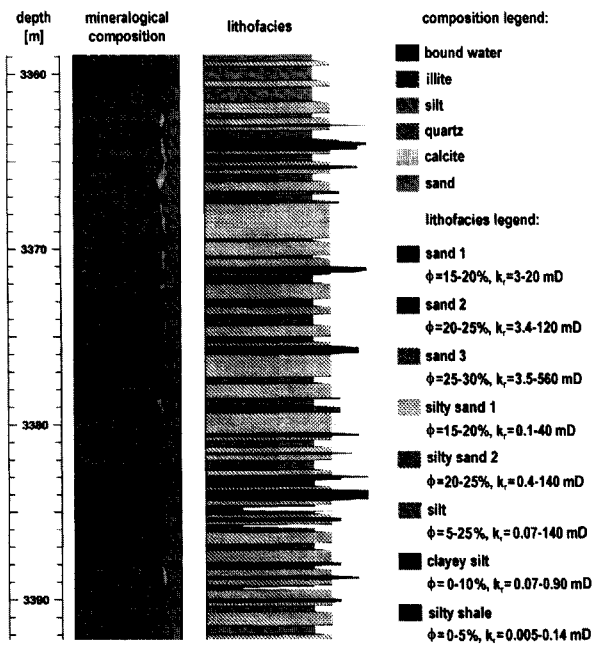

Figure 3.4: Litho-stratigraphic sequencing by electrofacies of a representative portion of well 1 as obtained from SHDT well-logs. The length of bars in the far right-hand column is related to lithotype permeability.

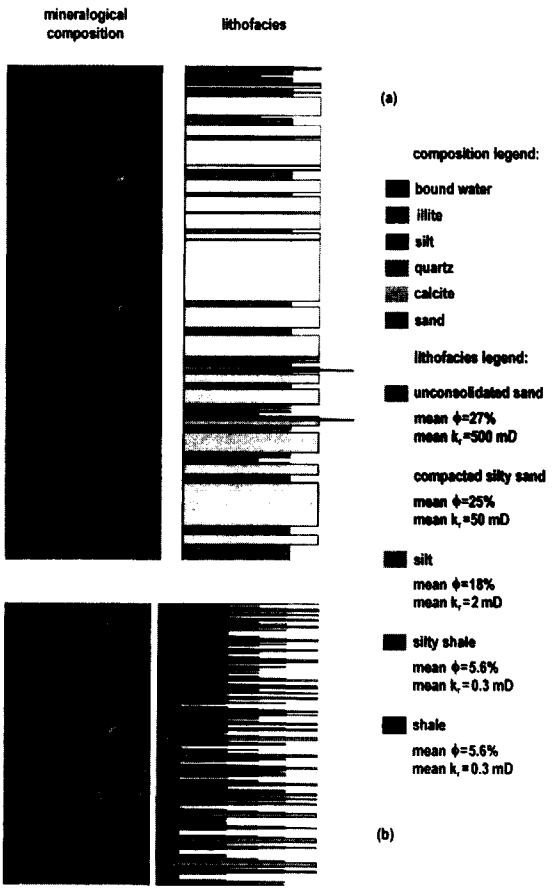

Figure 3.5: Same as in Figure 3.4, for well 2.

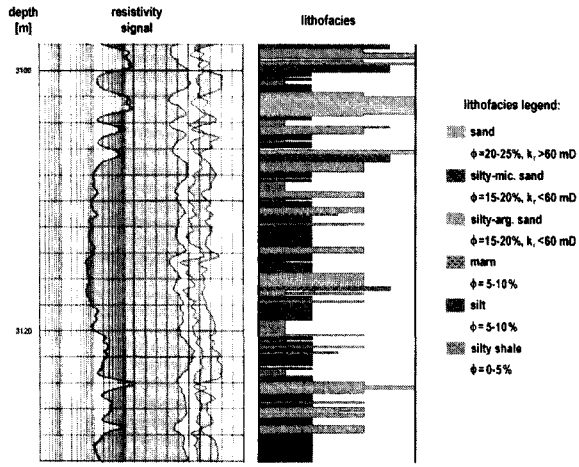

Figure 3.6: Same as in Figures 3.4 and 3.5, for well 3.

rating thin silt-clay layers which confine possible productive formations (Figure 3.4). A similar stratigraphy is predicted in the upper part of well 2 (Figure 3.5a) to a depth of about 1200 m, while further down (Figure 3.5b) the frequent alternation of thin sand, silt and clay horizons makes it much more difficult to distinguish between producing and non-producing geological units. Finally, the litho-stratigraphy for well 3 appears to feature thin sandy gas-bearing formations incorporated in a clayey porous matrix with a generally low permeability (Figure 3.6). As observed in the previous chapter, we can expect the marker measurements to be more reliable where relatively thick depleted sandy units prevail over the clayey ones, i.e. in well 1 and (to some extent) well 2, rather than in well 3.

3.3 Constitutive equations

Because a reliable knowledge of soil and rock compressibility is very important for the prediction of sediment compaction, a fairly large number of experimental studies has been performed over the last few decades to provide a realistic assessment of Northern Adriatic rock mechanical parameters. As mentioned previously, two pathways are currently available: laboratory measurements, i.e. oedometric and/or triaxial tests, and in situ measurements, using radioactive marker data.

Concerning the former, oedometers are widely used because they reproduce quite sat-

isfactorily the stress path of deep hydrocarbon reservoirs, i.e. vertical compaction with negligible lateral expansion [Gambolati *et al.*, 1999b]. Oedometric tests on samples obtained from drilling cores have been carried out since the early '70s, thus providing a fairly large database [Cassiani and Zoccatelli, 2000]. Lab uniaxial compressibilities c_M were analyzed by the "Commissione per lo Studio della Subsidenza di Ravenna" (Committee for the Study of Ravenna Subsidence) [Gambolati *et al.*, 1991] giving rise to a constitutive law for sands and clays with c_M decreasing with depth z from about 1.02×10^{-2} MPa^{-1} near the ground surface to 6.12×10^{-4} MPa^{-1} at 4000 m depth. These properties were later updated with more recent acquisitions [Bertoni *et al.*, 1995; Brignoli and Figoni, 1995] and used to predict land subsidence above the Dosso degli Angeli field [Gambolati *et al.*, 1998]. Experience has often shown, however, that such values are likely to be overestimated, thus leading to unreliable predictions of sediment compaction. This is often attributed to the stress release occurring in the sample on its way from the deep soil to the testing apparatus, and to the microcracks formed in the handling of the sample.

Radioactive marker surveys, done by ENI-Divisione Agip in several Northern Adriatic boreholes in the last ten years, have provided a new database of rock mechanical parameters derived from in situ compaction monitoring. The in situ c_M values have proved about one order of magnitude smaller than the lab c_M, thus showing the low reliability of lab sample findings. The new data will enable the development of a different and, hopefully, more reliable mechanical characterization of deep reservoir rocks [Baù *et al.*, 1999; Cassiani and Zoccatelli, 2000; Baù *et al.*, 2002]. However, despite recent attempts to account for the difference between lab and in situ compressibility as being due to aging effects [Hueckel *et al.*, 2000], the matter is still open to debate [Brighenti *et al.*, 2000].

For the aims of the present study, we chose to use constitutive laws derived from in situ c_M values. This is basically so for two reasons. First, recent studies seem to confirm that in situ c_M describes the deep rock mechanical behavior more realistically [Mobach and Gussinklo, 1994; Baù *et al.*, 1999; Teatini *et al.*, 2000; Cassiani and Zoccatelli, 2000; Macini and Mesini, 2000; Palozzo *et al.*, 2000]. Second, this allows for an "a posteriori" validation of in situ c_M through the correct reproduction of radioactive marker data by borehole modeling, as shown in the following chapters.

3.3.1 Virgin load conditions

As discussed in chapter 2, the compressibility values obtained from in situ measurements (eq. (2.6)) may be quite scattered because of the different uncertainties affecting the

data. To obtain a narrower confidence interval, the data are partially clustered by the moving average method (eq. (2.8)) and associated with the corresponding effective stress (eq. (2.9)). Denoting the number of boreholes with available measurements by b and the number of spacings in the $i-$th borehole by $N_{s,i}$, the data set to regress for a selected window size w is made of:

$$N_{tot} = \sum_{i=1}^{b} (N_{s,i} - w + 1)$$

values of $\overline{c_{M,k}}$ from equation (2.8), with the related variance $\sigma^2_{\overline{c_{M,k}}}$ and the effective stress $\overline{\sigma_{z,k}}$.

Plotting the data with an arithmetic scale suggests the use of a power law correlating uniaxial compressibility c_M with effective stress σ_z, and hence with depth z in undisturbed conditions:

$$c_M(\sigma_z) = M\sigma_z^P \tag{3.1}$$

with $M > 0$ and $P < 0$. A regression by equation (3.1) can be conveniently obtained on a double log-log plot, thus transforming it into a linear regression carried on the logarithms of the data:

$$\log c_M = \log M + P \log \sigma_z \quad \Rightarrow \quad y = \varrho + \varphi x \tag{3.2}$$

An additional difficulty is introduced here because the compressibility data to regress are to be regarded as statistical quantities, with an average value $\overline{c_{M,k}}$ for each $\sigma_{z,k}$ and an associated variance $\sigma^2_{\overline{c_{M,k}}}$. For this problem the linear regression (3.2) may be written as [Hald, 1952]:

$$y(x) = \varrho + \varphi(x - \overline{x}) \tag{3.3}$$

with the weighted mean $\overline{x}$ given by:

$$\overline{x} = \frac{\sum_{k=1}^{N_{tot}} w_k x_k}{\sum_{k=1}^{N_{tot}} w_k} \tag{3.4}$$

and the coefficients ϱ and φ by:

$$\varrho = \frac{\sum_{k=1}^{N_{tot}} w_k \overline{y}_k}{\sum_{k=1}^{N_{tot}} w_k} \tag{3.5}$$

$$\varphi = \frac{\sum_{k=1}^{N_{tot}} w_k \left(x_k - \overline{x}\right) \overline{y}_k}{\sum_{k=1}^{N_{tot}} w_k \left(x_k - \overline{x}\right)^2} \tag{3.6}$$

In the above equations $\overline{y}_k$ is the average value of y at x_k and the weights w_k are the inverse of the variance associated with $\overline{y}_k$:

$$w_k = \frac{1}{\sigma^2_{\overline{y}_k}} \qquad k = 1, 2, \ldots, N_{tot} \tag{3.7}$$

The variables x and y in equations (3.3) through (3.7) are the logarithmic transformation of the statistical data set $(\overline{\sigma_z}_{,k}, \overline{c_M}_{,k})$. According to Papoulis [1965], such a transformation yields:

$$x_k = \log \overline{\sigma_z}_{,k}$$

$$\overline{y}_k \simeq \log \overline{c_M}_{,k} - 0.21715 \left(\frac{\sigma_{\overline{c_M},k}}{\overline{c_M}_{,k}} \right)^2$$

$$\sigma^2_{\overline{y}_k} \simeq \left(0.43429 \frac{\sigma_{\overline{c_M},k}}{\overline{c_M}_{,k}} \right)^2 \left[1 - \frac{1}{4} \left(\frac{\sigma_{\overline{c_M},k}}{\overline{c_M}_{,k}} \right)^2 \right]$$

The empirical variance of the regressed data (eq. (3.3)) is given by [Hald, 1952]:

$$v^2 = \frac{\sum_{k=1}^{N_{tot}} \left[\overline{y}_k - y\left(x_k\right) \right]^2}{N_{tot} - 2}$$

so the 68% and 95% confidence intervals for $y\left(x\right)$ are obtained from:

$$y_{68\%}\left(x\right) = \varrho + \varphi \left(x - \overline{x}\right) \pm v \tag{3.8}$$

$$y_{95\%}\left(x\right) = \varrho + \varphi \left(x - \overline{x}\right) \pm 2v \tag{3.9}$$

Finally, back-transformation from equations (3.3), (3.8), and (3.9) to the original law (3.1) yields:

$$c_M\left(\sigma_z\right) = 10^{\varrho - \varphi \overline{x}} \sigma_z^{\varphi} = M \sigma_z^P \tag{3.10}$$

$$c_{M,68\%}\left(\sigma_z\right) = 10^{\varrho - \varphi \overline{x} \pm v} \sigma_z^{\varphi} = M^{\pm}_{68\%} \sigma_z^P \tag{3.11}$$

$$c_{M,95\%}\left(\sigma_z\right) = 10^{\varrho - \varphi \overline{x} \pm 2v} \sigma_z^{\varphi} = M^{\pm}_{95\%} \sigma_z^P \tag{3.12}$$

which represent the constitutive law and related confidence intervals obtained from the statistical analysis of the in situ radioactive marker measurements.

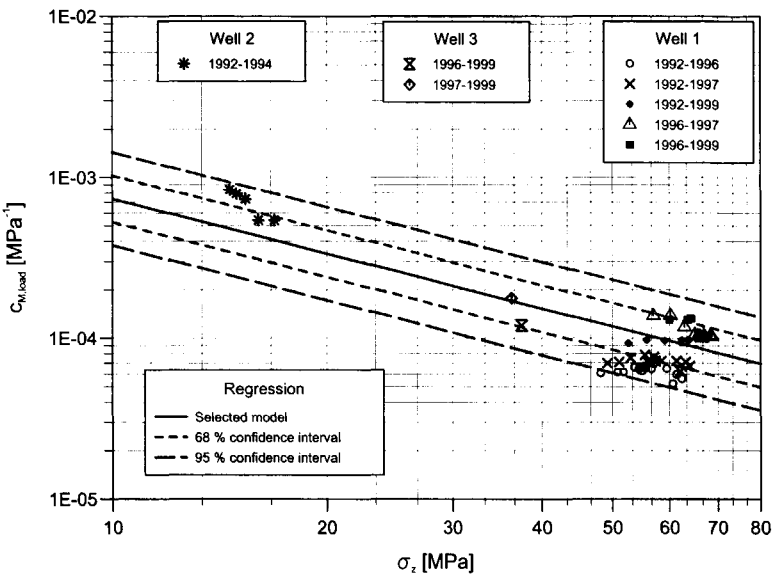

Figure 3.7: Constitutive law of uniaxial compressibility c_M in virgin loading conditions selected for the Northern Adriatic sediments. Confidence intervals and c_M values used for regression are also shown.

The available marker data are obtained from 3 wells in the Northern Adriatic basin monitored over 6 different time intervals [Baù *et al.*, 2002]. The data are first filtered for consistency in order to eliminate deformation measurements with a doubtful interpretation (see, for instance, the data reported in section 2.2.2). Then, equations (3.10) through (3.12) are calculated using a window size $w = 5$ and $w = 10$. Finally, the different regression straight lines are compared and the following is chosen as representative of the mechanical behavior of rock in the Northern Adriatic sediments under virgin loading conditions [Baù *et al.*, 2002]:

$$c_{M,\text{load}} = 1.0044 \cdot 10^{-2} \sigma_z^{-1.1347} \tag{3.13}$$

with $c_{M,\text{load}}$ in MPa^{-1} and σ_z in MPa. The factors $M^{\pm}_{68\%}$ and $M^{\pm}_{95\%}$ of equations (3.11) and (3.12) are:

$$M^{-}_{68\%} = 7.1989 \cdot 10^{-3} \qquad M^{+}_{68\%} = 1.4011 \cdot 10^{-2}$$

$$M^{-}_{95\%} = 5.1602 \cdot 10^{-3} \qquad M^{+}_{95\%} = 1.9546 \cdot 10^{-2}$$

A graphical representation of the constitutive law (3.13) with the associated confidence intervals is shown in Figure 3.7, where the $\overline{c_{M,k}}$ values used for regression are also given.

The selected law allows for a fairly good match with almost all measurements with the validity range of equation (3.13) limited to the σ_z interval between about 10 and 80 MPa, which corresponds approximately to a depth of between 900 and 7000 m in undisturbed conditions.

It should be observed that in soil mechanics the stiffness is often considered to be proportional to the isotropic stress, in agreement with Terzaghi's logarithmic compression formula [Terzaghi and Peck, 1967; Craig, 1974]. This would mean that $P = -1$ in equation (3.13), which is close to the value here obtained.

3.3.2 Unloading-reloading conditions

Production from some reservoirs monitored by well 1 was stopped in 1996 and 1997. In the two years that followed, a natural pore pressure recovery was observed, due to the active waterdrive connected to the field. Correspondingly, expansion measurements were obtained by the marker spacings incorporating the abandoned formations. Table 3.1 summarizes these data, which are graphically represented with respect to the productive layers in Figure 3.8. Table 3.2 shows the change of sign in the measured deformation in some spacings due to pore pressure decline and recovery.

These marker data enable an estimate of in situ uniaxial compressibility in unloading-reloading conditions. The limited size of the data set available suggests the direct regression of the single compressibility values (eq. (2.6)) with the related variance (eq. (2.7)), without using the moving average technique. The constitutive law (3.10) now reads [Baù *et al.*, 2002]:

$$c_{M,\text{unload}} = 2.9087 \cdot 10^{-4} \sigma_z^{-0.4315} \tag{3.14}$$

with $c_{M,\text{unload}}$ in MPa^{-1} and σ_z in MPa. The factors $M^{\pm}_{68\%}$ and $M^{\pm}_{95\%}$ are:

$$M^{-}_{68\%} = 1.7471 \cdot 10^{-4} \qquad M^{+}_{68\%} = 4.8426 \cdot 10^{-4}$$

$$M^{-}_{95\%} = 1.0494 \cdot 10^{-4} \qquad M^{+}_{95\%} = 8.0623 \cdot 10^{-4}$$

As expected, the limited amount of data produces a wider confidence interval and hence a smaller validity range than for virgin loading conditions. As shown in Figure 3.9 which represents the constitutive law (3.14) with the confidence intervals and the regressed measurements, this relationship holds true for $37 < \sigma_z < 65$ MPa, i.e. an approximate depth ranging between 3200 and 5800 m in undisturbed conditions.

It might be interesting to evaluate the ratio between the virgin loading and the unloading-reloading compressibility. Using the selected constitutive laws (3.13) and (3.14),

spacing	depth (m)		$\Delta h_{i,97-99}$	$\sigma_{\Delta h_{i,97-99}}$	$\Delta p_{i,97-99}$
i	upper marker	lower marker	(mm)	(mm)	(MPa)
1	2748	2759	-3.2	2.10	–
2	2759	2770	+1.1	1.20	-3.5
3	2770	2781	+2.2	1.80	-4.5
4	2781	2791	+0.2	1.00	-4.5
5	2869	2880	+7.1	0.64	+12.0
6	3230	3240	+5.0	0.40	+7.6
7	3240	3251	+2.2	0.43	+8.3
8	3251	3261	+3.9	1.20	+4.9
9	3348	3359	+2.8	0.58	+4.8
10	3359	3369	+2.6	0.75	+2.0
11	3369	3380	-0.1	0.34	+1.3
12	3380	3390	+0.8	0.62	-0.3
13	3390	3401	+1.4	0.39	-1.2
14	3401	3411	-1.8	1.20	-0.2
15	3449	3460	-5.0	0.57	-3.3
16	3460	3470	-5.5	0.92	-2.3
17	3470	3481	-0.9	0.38	-1.6
18	3502	3512	-9.0	0.44	-3.8
19	3512	3523	-1.0	0.46	n.a.
20	3523	3534	-1.3	0.69	n.a.
21	3647	3657	-2.0	0.33	-2.5
22	3657	3667	-2.8	0.27	-2.5
23	3667	3678	+0.9	0.54	+1.0
24	3678	3688	+0.4	0.49	+0.4
25	3688	3699	+0.4	0.65	+0.4
26	3699	3710	+4.3	0.54	+0.3
27	3710	3720	+6.1	0.67	–
28	3720	3730	-5.5	1.00	-4.3

Table 3.1: Marker measurements and corresponding pore pressure variations in well 1 during 1997-1999. n.a. = not available.

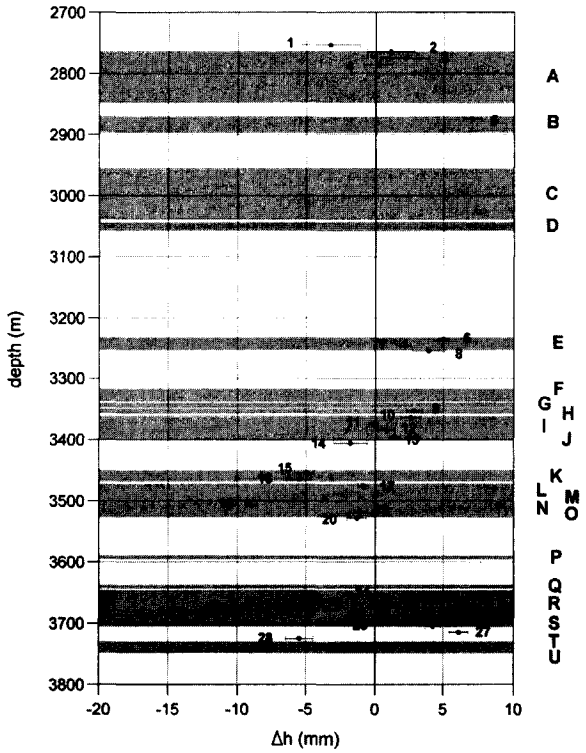

Figure 3.8: Marker measurements referred to the midpoint of each interval for well 1, 1997-1999.

Average marker spacing depth (m)	1992-1996 Δp (MPa)	1992-1996 $\Delta\overline{h} \pm \sigma_{\Delta\overline{h}}$ (mm)	1996-1997 Δp (MPa)	1996-1997 $\Delta\overline{h} \pm \sigma_{\Delta\overline{h}}$ (mm)	1997-1999 Δp (MPa)	1997-1999 $\Delta\overline{h} \pm \sigma_{\Delta\overline{h}}$ (mm)
2874.5	-9.5	-7.2 ± 1.5	-3.1	-7.3 ± 1.4	+12.2	$+7.0 \pm 0.6$
3235.0	-4.8	-8.9 ± 0.8	+4.3	$+2.4 \pm 0.8$	+7.8	$+5.0 \pm 0.4$
3245.5	-5.2	-5.0 ± 0.4	+4.7	$+2.1 \pm 0.5$	+8.4	$+2.2 \pm 0.4$
3256.0	-1.8	-1.1 ± 0.6	+1.6	-0.5 ± 0.7	+3.0	$+3.9 \pm 1.2$
3354.5	-20.9	-11.5 ± 0.3	-3.6	-4.5 ± 0.4	+5.0	$+2.8 \pm 0.6$
3364.0	-8.4	-7.1 ± 0.8	-1.2	-1.1 ± 0.7	+2.1	$+2.6 \pm 0.7$

Table 3.2: Pore pressure change and marker measurements for the spacings in well 1 where a pore pressure recovery was observed after 1996.

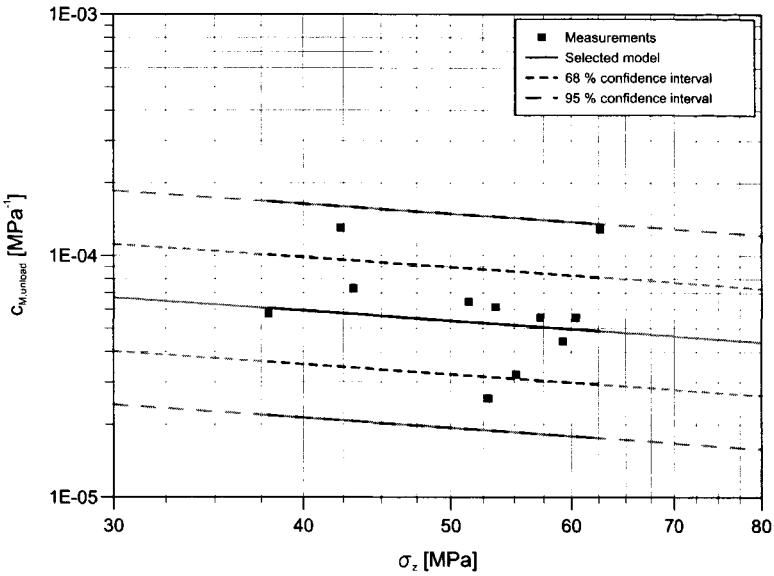

Figure 3.9: The same as Figure 3.7 for unloading-reloading conditions.

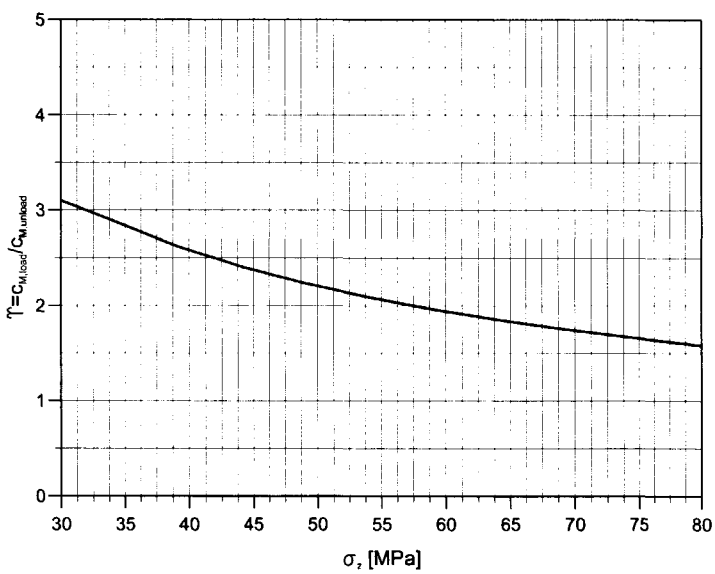

Figure 3.10: Ratio between virgin loading and unloading-reloading compressibility using the constitutive laws (3.13) and (3.14).

we obtain:

$$\Upsilon = \frac{c_{M,\text{load}}}{c_{M,\text{unload}}} = 34.53089\sigma_z^{-0.7032} \tag{3.15}$$

with σ_z in MPa and Υ a dimensionless factor. Equation (3.15) is graphically represented in Figure 3.10. Within the reliable range, i.e. approximately $30 < \sigma_z < 80$ MPa, Υ exhibits quite a narrow interval, between 1.5 and 3, with an average value of 2.2.

3.3.3 Biot coefficient

The coupling effect of pore pressure variation on porous matrix deformation, and vice versa, is also related to the Biot coefficient α (see eq. (1.10)) defined as:

$$\alpha = 1 - \frac{c_{br}}{c_{bm}} \tag{3.16}$$

where c_{br} is the grain compressibility and c_{bm} the bulk volumetric compressibility. We assume $c_{br} = 1.63 \times 10^{-5}$ MPa^{-1}, as suggested by Geertsma [1973b]. The value of the volumetric compressibility c_{bm} is related to the uniaxial compressibility c_M by:

$$c_{bm} = 3\frac{1-\nu}{1+\nu}c_M \tag{3.17}$$

ν being the Poisson ratio. The Poisson ratio was measured by ENI-Divisione Agip by means of a number of in situ hydraulic fracture tests [Teatini *et al.*, 2000]. An average confinement factor $\kappa = \nu/1 - \nu = 0.546$ was derived, hence $\nu = 0.35$. The outcome of triaxial lab tests on Northern Adriatic samples at variable depths provides an average value $\nu = 0.25$ [Teatini *et al.*, 2000]. So a final value of 0.30 can reasonably be assumed for the Poisson ratio in the Northern Adriatic boreholes.

Implementing the constitutive law (3.13) into equation (3.17) enables an estimation of Biot's coefficient as a function of the effective stress σ_z, and hence of the depth z in undisturbed conditions. The graphical representation of equation (3.16) is given in Figure 3.11. Note that, for the depth of interest for hydrocarbon reservoirs, i.e. down to 4500 m, α is quite close to one, so the usual assumption of rigid solid grains ($c_{br} \ll c_{bm}$) appears to be generally acceptable for our problem.

3.4 Hydraulic properties

The reliable evaluation of hydraulic properties is often one of the most difficult tasks in the petrophysical characterization of deep reservoirs. Permeability k is established from

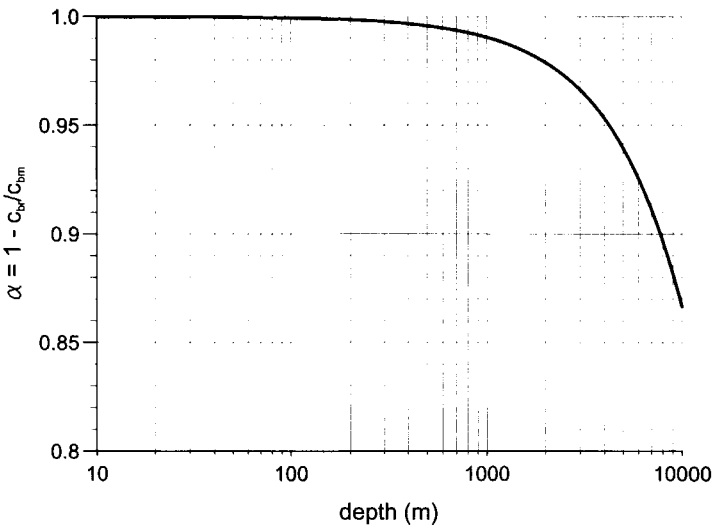

Figure 3.11: Biot coefficient α vs depth in undisturbed conditions.

lab tests on rock samples used to estimate the production of each gas field, while porosity ϕ is measured in situ by EATT logs, which relate the attenuation of an electromagnetic wave transmitted through the formation to the fluid content, and hence the porosity, of each facies. The available k and ϕ values associated with the lithotypes identified by electrofacies in wells 1, 2 and 3 are shown in Figures 3.4, 3.5, and 3.6. Some permeability values for shale layers are also provided.

In petroleum engineering, permeability is usually recorded in "Darcy" units (D) or their submultiple "milliDarcy". This unit actually corresponds to the intrinsic permeability k_r (m^2 in the International System, 1 D = $0.9869233 \cdot 10^{-12}$ m^2) which relates to the hydraulic conductivity, or permeability, k by:

$$k = \frac{k_r \rho}{\mu} \tag{3.18}$$

where ρ and μ are the pore fluid density and viscosity, respectively. In (3.18) with k_r given in [m^2], k is expressed in [m/s]. The use of mD units for k_r in equation (3.18) calls for the introduction of appropriate dimensional coefficients to obtain the correct unit conversion:

$$k \text{ [m/s]} = \frac{0.9869233 \cdot \rho \cdot k_r \text{ [mD]}}{10^{15} \cdot \mu} \tag{3.19}$$

It should be remembered that ρ and μ have to be calculated in reservoir conditions.

For instance, if the pore fluid is groundwater, we have [Chierici and Long, 1953]:

$$\rho_w(p,T,c) = 730.6 + 2.025T - 3.8\cdot 10^{-3}T^2 + \left[2.362 - 1.197\cdot 10^{-2}T + 1.835\cdot \right.$$
$$\left.\cdot 10^{-5}T^2\right]p + \left[2.374 - 1.024\cdot 10^{-2}T + 1.49\cdot 10^{-5}T^2 - 5.1\cdot 10^{-4}\cdot \right.$$
$$\left.\cdot p\right]c \qquad (3.20)$$

and [Schlumberger, 1974]:

$$\mu_w(T,c) = 10^3\left(1 + 2.765\cdot 10^{-3}c\right)\exp\left[11.897 - 5.943\cdot 10^{-2}T + 6.422\cdot 10^{-5}T^2\right] \qquad (3.21)$$

where p is the pore pressure in [MPa], T the temperature in [K], c the salinity in [kg/m^3], and the numerical coefficients have the corresponding appropriate dimensions. The resulting groundwater density ρ_w is expressed in [kg/m^3] and the viscosity μ_w in [Pa·s]. The above experimental relationships have the following validity ranges:

$$0 < p < 50 \text{ MPa}$$
$$273 < T < 393 \text{ K}$$
$$0 < c < 300 \text{ kg/m}^3$$

The temperature used in equations (3.20) and (3.21) is calculated as:

$$T = T_0 + g_t z \qquad (3.22)$$

where g_t is the thermal gradient in [K/m] and T_0 the surface temperature. The average value of g_t is usually assumed to equate 0.029 K/m. However, experimental measurements and geological considerations [Mattavelli and Novelli, 1990] suggest using a smaller value, i.e. 0.02 K/m, for the Northern Adriatic basin. In equation (3.22) the surface temperature is conventionally assumed to be 288.2 K, i.e. 15 °C [Chierici, 1989].

As shown in Figures 3.4, 3.5, and 3.6, the litho-stratigraphic sequence in the Northern Adriatic boreholes may exhibit a very pronounced vertical heterogeneity on a small scale, often less than a few centimeters. For practical calculations it may be useful to combine several thin layers into a thicker unit characterized by an equivalent horizontal and vertical permeability, k_h and k_v respectively.

Consider a layered formation consisting of n different layers with thickness s_i and permeability k_i (Figure 3.12), and assume a horizontal flow through the total thickness s due to a variation in the hydraulic head $\Delta\Phi$ over a unitary horizontal length. For the sake of simplicity and without loss of generality, we refer to a plane analysis. According to Darcy's law, the fluid discharge q_h through the $i-$th layer is:

$$q_{h,i} = s_i k_i \Delta\Phi_i \qquad (3.23)$$

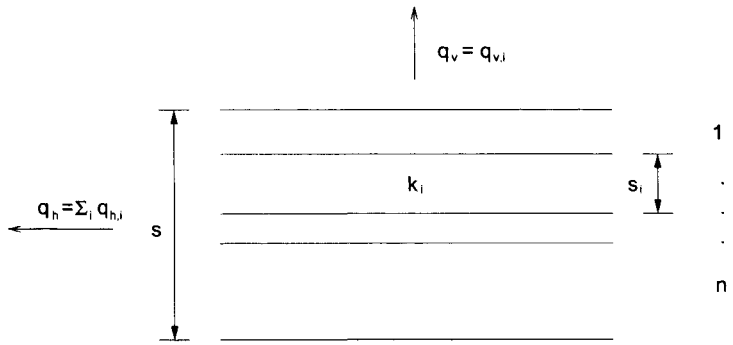

Figure 3.12: Sample layered formation for the equivalent horizontal and vertical permeability estimate.

while the total discharge is:

$$q_h = sk_h\Delta\Phi \tag{3.24}$$

The total q_h must equal the sum of $q_{h,i}$. Hence, equation (3.24) with equation (3.23) becomes:

$$\sum_{i=1}^{n}(s_i k_i \Delta\Phi_i) = sk_h\Delta\Phi$$

and, noting that for a horizontal flux $\Delta\Phi_i = \Delta\Phi$, $i = 1, \ldots, n$, we obtain:

$$k_h = \frac{\sum_{i=1}^{n} s_i k_i}{s} \tag{3.25}$$

Now assume a vertical flow through a unitary horizontal length due to a variation in hydraulic head $\Delta\Phi$ over the total thickness s. Again, with Darcy's law we can write the fluid discharge q_v through the $i-$th layer as:

$$q_{v,i} = k_i \frac{\Delta\Phi_i}{s_i} \tag{3.26}$$

and the total discharge as:

$$q_v = k_v \frac{\Delta\Phi}{s} \tag{3.27}$$

In this case, the total variation in hydraulic head $\Delta\Phi$ must equal the sum of the hydraulic head variations $\Delta\Phi_i$ occurring in each layer. Solving equations (3.26) and (3.27) for $\Delta\Phi_i$ and $\Delta\Phi$, respectively, yields:

$$\frac{sq_v}{k_v} = \sum_{i=1}^{n}\left(\frac{s_i q_{v,i}}{k_i}\right)$$

Conservation of the vertical fluid discharge implies $q_v = q_{v,i}$, $i = 1, \ldots, n$, i.e.:

$$k_v = \frac{s}{\sum_{i=1}^{n} s_i/k_i} \tag{3.28}$$

In geohydrology the above formulas (3.25) and (3.28) are usually summarized stating that for a horizontal flow the transmissivities must be added, whereas for vertical flow the resistances should be added.

The combination of thin layers into a thicker unit with equivalent horizontal and vertical permeabilities k_h and k_v gives rise to an equivalent anisotropic layer with anisotropy ratio a_k equal to:

$$a_k = \frac{k_h}{k_v} = \frac{(\sum_{i=1}^{n} s_i k_i)\,(\sum_{i=1}^{n} s_i/k_i)}{s^2}$$

which is larger than 1, or at least as large in the trivial case $n = 1$.

3.5 Conclusions

In order to provide a reliable interpretation of in situ radioactive marker measurements, it is essential to have detailed litho-stratigraphic sequences, together with realistic hydro-geomechanical properties of deep reservoirs. Recently-developed technologies combined with the statistical correlation between log-response patterns and deep rock properties allow for high-resolution litho-stratigraphies and facies characterizations. Examples are given of the detailed lithological sequences recognized by SHDT and EATT logging tools in wells 1, 2 and 3.

A fairly large database is currently available for rock mechanical characterization, resulting from oedometric and triaxial tests performed over the last 30 years on borehole rock samples, together with more recent uniaxial compressibility estimates obtained from in situ deformation measurements. There are some differences between lab and in situ compressibilities; in the present work, priority is given to in situ data on the assumption that it is more reliable, as claimed by a number of authors, and with a view to an "a posteriori" constitutive law validation through modeling.

By contrast, hydraulic properties, and particularly permeability, are generally derived from lab tests performed on rock samples with the purpose to estimate production from each gas field.

In particular, the following points are worth emphasizing:

- electrofacies analyses show a very pronounced heterogeneity, often on a scale smaller than the marker spacing. Typical lithological configurations of the Northern Adriatic basin exhibit the occurrence of sandy productive formations up to a few dozen meters thick, confined by thin (1 m or less) shale caprocks, as in borehole 1, as well

as thin reservoirs (even less than 1 m thick) incorporated in a mainly clayey porous matrix, as in borehole 3;

- using a statistical approach, the available marker data are used to develop a constitutive law for uniaxial rock compressibility, versus the effective vertical stress, and hence depth in undisturbed conditions. A few expansion measurements, obtained after the field was abandoned and during the natural pore pressure recovery phase, enable a first preliminary constitutive relationship in unloading-reloading conditions, with a $c_{M,\text{load}}/c_{M,\text{unload}}$ ratio between 1.5 and 3;

- a homogenization procedure is presented for permeability in order to combine thin layers into a thicker unit. Equivalent horizontal and vertical permeability coefficients are calculated using Darcy's law, thus also giving rise to a vertical hydraulic anisotropy ratio a_k.

The hydro-geomechanical parameters discussed in the present chapter allow for a reliable rock characterization for the Northern Adriatic basin. These data will be used to reproduce the rock deformations accurately on a marker scale with the aid of a finite element numerical model.

Chapter 4

Radioactive marker response in heterogeneous reservoirs

A numerical study is performed to simulate the vertical deformation recorded within a depth interval representing a marker spacing (10.5 m wide) in deep heterogeneous sedimentary reservoirs during production. The realistic hydro-geo-mechanical setting of the Northern Adriatic basin is used, with particular reference to two basic geologic scenarios typical of the study area. In the former, sands prevail within the marker spacing with thin low permeable confining caprocks; in the latter, thin sandy producing layers are incorporated in a mostly clayey porous matrix. The sensitivity of the marker response is investigated in relation to clay and sand permeability and compressibility, Biot's coefficient, and respective position of monitoring and fluid pumping wells. The results presented in this chapter confirm the theoretical qualitative behaviour predicted by Geertsma's model, with rock expanding above and below the depleted layers. This phenomenon may have a strong influence on radioactive marker response, in dependence on the actual marker position and stratigraphic configuration. Moreover, the numerical analysis performed in this chapter helps provide some indications as to the marker reliability and suitability in sedimentary, highly heterogeneous geological structures.

4.1 Introduction

Several gas fields in the Northern Adriatic basin are currently monitored during production using the radioactive marker technique. The marker surveys started in 1992, collecting records every two or four years, including static pressure values in the test holes, with

the aid of the FSMT by Schlumberger and the CMI by Western Atlas. By 1999, eleven surveys on three of five monitoring boreholes had been completed, with the marker data processed statistically, as shown in chapters 2 and 3, to provide a basin-scale constitutive law for uniaxial compressibility in virgin loading and unloading-reloading conditions. Significant data scatter was observed, however, with a large associated standard deviation which could hardly correlate with a natural c_M variability due to lithology alone. Moreover, a number of measurements (some of which were reported in chapter 2 as an example) were excluded from the analysis because of their inconsistency with the assumptions leading to the uniaxial compressibility estimate of the monitored porous medium. These difficulties in the direct use of in situ measurements for the mechanical characterization of rock in deep reservoirs has raised some concern as to the actual reliability of the marker data [Bevilacqua *et al.*, 1999; Brighenti *et al.*, 2000].

As discussed in chapter 3, the Northern Adriatic basin is characterized by sedimentary sequences that are heterogeneous over a smaller, and locally much smaller scale than the radioactive marker measurement scale, i.e. 10.5 m. In particular, the key feature of productive reservoirs in this area is that gas accumulation occurs in multi-pay formations with a thickness varying from a few centimeters to several meters. Such conditions appear to favor the generation of expanding rock formations among the producing volumes, as verified theoretically using Geertsma's approach [1966; 1973a] in chapter 2, which can influence the radioactive marker measurements, even quite significantly in some cases.

Some tentative interpretations have been suggested [Ferronato *et al.*, 2003a] and verified [Ferronato *et al.*, 2003b] in several examples to account for the unexpected behavior of some marker spacings. For instance, if the depleted layer is considerably thinner than the marker spacing, only a fraction of the monitored depth interval undergoes compaction with the surrounding unproductive rocks exhibiting an expansion. This usually leads to an overall reduced marker compaction and a consequent c_M underestimation, or even in some particular configurations to an expansion, which must be discarded from the statistical analysis used to update the monitored rock's mechanical properties. Another situation leading to unreliable marker data may develop when the monitoring borehole is too close to, or even coincides with, a producing well. In this case, apart from the technological problems involved [Mobach and Gussinklo, 1994], the horizontal pore pressure gradients caused by fluid extraction may be large enough to generate a horizontal strain opposing the vertical compaction. Such a condition is no longer consistent with an oedometric deformation and may yield important an underestimation of the compressibility c_M.

The aim of the analysis developed in the present chapter is to reproduce the response

of an ideal marker tool by means of a coupled poroelastic mathematical model. The study addresses the vertical deformation at the marker resolution scale of a litho-stratigraphic column with a heterogeneous sequence similar to the one observed in the Northern Adriatic test holes using the electrofacies analysis (see chapter 3). In particular, the investigation focuses on the stratigraphic configurations that may lead to unexpected marker measurements, pointing to rock expansions despite a decline in pore pressure.

The chapter is organized as follows. The finite element model for solving Biot's poroelastic equations, discussed in chapter 1, is specifically adapted to the problem of marker-scale rock deformation along a vertical test hole. Based on the stratigraphic sequences detected by electrofacies, two layering configurations typical of the Northern Adriatic boreholes are selected and discretized with a high-resolution mesh. The results obtained with the finite element model are first checked for consistency versus the analytical results provided by the classical Geertsma approach [1966; 1973a], then used to analyze the radioactive marker measurements. A sensitivity analysis is performed on the main hydro-geomechanical properties of the porous medium, such as compressibility, permeability, and the Biot coefficient, to capture the main mechanisms most affecting the marker measurements. On the basis of this analysis, a few typical layering configurations that prompt a critical interpretation of marker data are simulated and discussed, also showing the possible consequences on the final uniaxial compressibility estimate. Finally, some conclusive remarks are made, with recommendations for an efficient marker installation strategy in heterogeneous reservoirs.

4.2 Finite Element numerical model

The stress and strain fields induced in a deforming porous medium by the development of deep producing reservoirs, and so by the consequent pore pressure variation occurring in the depleted volumes, can be described by the classic Biot poroelasticity theory [1941], in which saturating fluid pressures and skeleton displacements are intimately connected. Since the present analysis is mainly concerned with the structural behavior of the porous matrix due to the depletion of producing volumes, the medium can be considered as fully saturated by a single-phase fluid with the source of strength given by an appropriate pore pressure decline distribution in the active reservoirs. The saturating fluid is assumed to be groundwater. Finally, the location of compacting volumes at a considerable depth (more than 3000 m) with a relatively small pore pressure variation suggests that in this case the medium can reasonably be assumed to behave elastically, with the assumption

of small strains.

4.2.1 Axi-symmetric setting

The main results of interest here are the vertical displacements occurring along a monitoring borehole where a marker tool is supposed to be installed. For this purpose, an axi-symmetric instead of a fully three-dimensional setting can be assumed, with the ideal radioactive markers implemented along the symmetry axis.

Let's consider a cylindrical reference frame r, θ, and z. The classical poroelastic equations by Biot [1941], as modified later by Van der Knaap [1959], Geertsma [1966], and Verruijt [1969], written in the unknown radial and vertical displacements u_r and u_z now read:

$$G\nabla^2 u_r + (G+\lambda)\frac{\partial \epsilon}{\partial r} - G\frac{u_r}{r^2} = \alpha\frac{\partial p}{\partial r} \tag{4.1}$$

$$G\nabla^2 u_z + (G+\lambda)\frac{\partial \epsilon}{\partial z} = \alpha\frac{\partial p}{\partial z} \tag{4.2}$$

$$\frac{k}{\gamma}\nabla^2 p = [\phi\beta + c_{br}(\alpha-\phi)]\frac{\partial p}{\partial t} + \alpha\frac{\partial \epsilon}{\partial t} \tag{4.3}$$

where λ and G are the Lamé constant and the shear modulus of the porous medium. Note that assuming axial symmetry means that u_θ vanishes and the groundwater flow equation (4.3) formally coincides with equation (1.10) taking the following definitions into account for the medium volumetric strain ϵ:

$$\epsilon = \frac{\partial u_r}{\partial r} + \frac{u_r}{r} + \frac{\partial u_z}{z}$$

and the Laplace operator ∇^2:

$$\nabla^2 = \frac{\partial^2}{\partial r^2} + \frac{\partial^2}{\partial z^2} + \frac{1}{r}\frac{\partial}{\partial r}$$

The structural equations (4.1) and (4.2) are integrated by the use of the principle of virtual work for the whole system and Terzaghi's effective stress concept (eq. (1.3)). To obtain a linear algebraic system, the standard Finite Element approach for elastic continuum problems is used [Zienkiewicz and Taylor, 1989], thus yielding the matricial form (1.8):

$$\mathbf{K}\boldsymbol{\delta} - \mathbf{Q}\mathbf{p} = \mathbf{f}^u$$

The hypothesis of axial symmetry suggests using annular finite elements and integrating equations (4.1) and (4.2) over a vertical cross-section passing through the symmetry

axis. We chose to use a triangular cross-section for the annular elements, since this allows for a much larger number of finite elements and this appears to be an important issue in reproducing the very pronounced small-scale heterogeneity typical of the Northern Adriatic boreholes as accurately as possible (see Figures 3.4, 3.5, and 3.6). The local displacement and pore pressure vectors in the generic element e are:

$$\boldsymbol{\delta}_e^T = \begin{bmatrix} u_{r,i} & u_{z,i} & u_{r,j} & u_{z,j} & u_{r,m} & u_{z,m} \end{bmatrix}$$

$$\mathbf{p}_e^T = \begin{bmatrix} p_i & p_j & p_m \end{bmatrix}$$

where the subscripts i, j, and m indicate the nodes corresponding to element e. The shape functions N are linear. For node i, the shape function can be written as:

$$N_i = \frac{a_i + b_i r + c_i z}{2\Delta_e}$$

with:

- $a_i = r_j z_m - r_m z_j$;
- $b_i = z_j - z_m$;
- $c_i = r_m - r_j$;
- $2\Delta_e = \det \begin{bmatrix} 1 & r_i & z_i \\ 1 & r_j & z_j \\ 1 & r_m & z_m \end{bmatrix}$, i.e. twice the area of the triangular cross-section of element e.

Shape functions N_j and N_m are simply obtained from N_i by an index permutation.

The local displacement vector is therefore (see eq. (1.4)):

$$\mathbf{u}_e = \mathbf{N}_{u,e}\boldsymbol{\delta}_e = \begin{bmatrix} N_i\mathbf{I}_2 & N_j\mathbf{I}_2 & N_m\mathbf{I}_2 \end{bmatrix} \boldsymbol{\delta}_e \tag{4.4}$$

Assuming small deformations, the strain components can be related to displacements by the following first-order relationships:

$$\epsilon_r = \frac{\partial u_r}{\partial r}, \quad \epsilon_z = \frac{\partial u_z}{\partial z},$$

$$\epsilon_\theta = \frac{u_r}{r}, \quad \gamma_{rz} = \frac{\partial u_r}{\partial z} + \frac{\partial u_z}{\partial r},$$

with null $\gamma_{\theta r}$ and $\gamma_{z\theta}$ because of the axial symmetry assumption. The differential operator $\mathbf{L}$ to use in equation (1.7) is:

$$\mathbf{L} = \begin{bmatrix} \dfrac{\partial}{\partial r} & 0 \\ 0 & \dfrac{\partial}{\partial z} \\ r^{-1} & 0 \\ \dfrac{\partial}{\partial z} & \dfrac{\partial}{\partial r} \end{bmatrix} \tag{4.5}$$

so the local strain matrix $\mathbf{B}_e$ from equations (4.4) and (4.5) can be written as:

$$\mathbf{B}_e = \mathbf{L}\mathbf{N}_{u,e} = \frac{1}{2\Delta_e} \begin{bmatrix} b_i & 0 & b_j & 0 & b_m & 0 \\ 0 & c_i & 0 & c_j & 0 & c_m \\ \dfrac{2\Delta_e N_i}{r} & 0 & \dfrac{2\Delta_e N_j}{r} & 0 & \dfrac{2\Delta_e N_m}{r} & 0 \\ c_i & b_i & c_j & b_j & c_m & b_m \end{bmatrix} \tag{4.6}$$

Equation (1.6) needs the local elastic matrix $\mathbf{D}$ over element e, which – for an isotropic medium – reads:

$$\mathbf{D}_e = \frac{E_e\,(1-\nu_e)}{(1+\nu_e)\,(1-2\nu_e)} \begin{bmatrix} 1 & \dfrac{\nu_e}{1-\nu_e} & \dfrac{\nu_e}{1-\nu_e} & 0 \\ \dfrac{\nu_e}{1-\nu_e} & 1 & \dfrac{\nu_e}{1-\nu_e} & 0 \\ \dfrac{\nu_e}{1-\nu_e} & \dfrac{\nu_e}{1-\nu_e} & 1 & 0 \\ 0 & 0 & 0 & \dfrac{1-2\nu_e}{2\,(1-\nu_e)} \end{bmatrix} \tag{4.7}$$

where E_e and ν_e are the Young modulus and the Poisson ratio of the porous medium in the element e. Note that the factor $E_e\,(1-\nu_e)\,/\,[(1+\nu_e)\,(1-2\nu_e)]$ is the inverse of the vertical uniaxial compressibility $c_{M,e}$, so equation (4.7) can also be written as:

$$\mathbf{D}_e = \frac{\mathbf{D}'_e}{c_{M,e}} \tag{4.8}$$

Equation (4.8) can be used to introduce non-linearities in the elastic behavior of the porous matrix by varying $c_{M,e}$.

From equation (1.8), the local expression for the elastic stiffness and the coupling matrices $\mathbf{K}_e$ and $\mathbf{Q}_e$ can now be calculated. Bearing in mind that the integration volume is an annular element with a triangular cross-section Δ_e, we have:

$$\mathbf{K}_e = \int_e \mathbf{B}_e^T \mathbf{D}_e \mathbf{B}_e dV_e = 2\pi \int_{\Delta_e} \mathbf{B}_e^T \mathbf{D}_e \mathbf{B}_e r dr dz \tag{4.9}$$

$$\mathbf{Q}_e = \int_e \alpha_e \mathbf{B}_e^T \mathbf{i}\mathbf{N}_{p,e} dV_e = 2\pi \int_{\Delta_e} \alpha_e \mathbf{B}_e^T \mathbf{i}\mathbf{N}_{p,e} r dr dz \tag{4.10}$$

We recall that $\mathbf{i}^T = [1,1,1,0]$ (see eq. (1.1)) and that the elemental pore pressure is (see eq. (1.5)):

$$p_e = \mathbf{N}_{p,e}\mathbf{p}_e = \begin{bmatrix} N_i & N_j & N_m \end{bmatrix} \mathbf{p}_e$$

As equation (4.6) shows, the explicit calculation of integrals (4.9) and (4.10) is not trivial because the inner functions depend on the radial and vertical coordinates r and z. If the mesh is sufficiently refined, however, we can assume the elastic strain matrix $\mathbf{B}_e$ and the coordinate r to be constant over e:

$$\mathbf{B}_e(r,z) \simeq \overline{\mathbf{B}}_e(\overline{r}_e, \overline{z}_e) \qquad r \simeq \overline{r}_e \tag{4.11}$$

where $\overline{r}_e$ and $\overline{z}_e$ are the gravity center coordinates for the triangular cross-section of element e:

$$\overline{r}_e = \frac{r_i + r_j + r_k}{3} \qquad \overline{z}_e = \frac{z_i + z_j + z_k}{3}$$

It can be seen that such an approximation is satisfactory as long as a sufficiently fine radial discretization is used in the close vicinity of the symmetry axis. For a thorough discussion of the errors introduced and a comparison with the exact integration, see Gambolati *et al.* [2001a].

By the use of assumption (4.11) in equations (4.9) and (4.10), and bearing in mind that:

$$\int_{\Delta_e} N_k d\Delta_e = \frac{\Delta_e}{3} \qquad k = i,j,m \tag{4.12}$$

$$\int_{\Delta_e} N_k N_l d\Delta_e = \begin{cases} \dfrac{\Delta_e}{6} & \text{if } k = l \\ \dfrac{\Delta_e}{12} & \text{if } k \neq l \end{cases} \tag{4.13}$$

we have the following local expressions for $\mathbf{K}_e$ and $\mathbf{Q}_e$:

$$\mathbf{K}_e = 2\pi \overline{\mathbf{B}}_e^T \mathbf{D}_e \overline{\mathbf{B}}_e \overline{r}_e \Delta_e \tag{4.14}$$

$$\mathbf{Q}_e = \frac{\alpha_e \pi \overline{r}_e}{3} \begin{bmatrix} b_i + \dfrac{\Delta_e}{\overline{r}_e} & b_i + \dfrac{\Delta_e}{2\overline{r}_e} & b_i + \dfrac{\Delta_e}{2\overline{r}_e} \\ c_i & c_i & c_i \\ b_j + \dfrac{\Delta_e}{2\overline{r}_e} & b_j + \dfrac{\Delta_e}{\overline{r}_e} & b_j + \dfrac{\Delta_e}{2\overline{r}_e} \\ c_j & c_j & c_j \\ b_m + \dfrac{\Delta_e}{2\overline{r}_e} & b_m + \dfrac{\Delta_e}{2\overline{r}_e} & b_m + \dfrac{\Delta_e}{\overline{r}_e} \\ c_m & c_m & c_m \end{bmatrix} \tag{4.15}$$

The solution to the groundwater flow equation (4.3) is obtained with the Galerkin method of weighted residuals and Green's first identity, so as to allow for a linear approximation of pore pressure over each finite element (eq. (1.11)). This standard Finite Element technique [Zienkiewicz *et al.*, 1975; Huyakorn and Pinder, 1983] yields the global matricial form (1.12):

$$\mathbf{Hp} + \mathbf{P}\dot{\mathbf{p}} + \mathbf{Q}^T\dot{\boldsymbol{\delta}} = \mathbf{f}^p$$

Using the corresponding definitions, the local expressions for the flow stiffness and capacity matrices $\mathbf{H}_e$ and $\mathbf{P}_e$ can now be calculated, obtaining:

$$\mathbf{H}_e = \int_e \frac{k_e}{\gamma} \left(\nabla \mathbf{N}_{p,e}\right)^T \nabla \mathbf{N}_{p,e} dV_e = \frac{2\pi}{\gamma} \int_{\Delta_e} k_e \left(\nabla \mathbf{N}_{p,e}\right)^T \nabla \mathbf{N}_{p,e} r dr dz \tag{4.16}$$

$$\mathbf{P}_e = \int_e \left[\phi\beta + c_{br}\left(\alpha - \phi\right)\right]_e \mathbf{N}_{p,e}^T \mathbf{N}_{p,e} dV_e = 2\pi \int_{\Delta_e} \left[\phi\beta + c_{br}\left(\alpha - \phi\right)\right]_e \mathbf{N}_{p,e}^T \mathbf{N}_{p,e} r dr dz \tag{4.17}$$

where $\nabla = [\partial/\partial r, \partial/\partial z]^T$ is the gradient operator. To account for the hydraulic anisotropy that may occur along the Northern Adriatic boreholes (see eqs. (3.25) and (3.28)), local permeability k_e is expressed in a tensorial form:

$$\mathbf{k}_e = \begin{bmatrix} k_{h,e} & 0 \\ 0 & k_{v,e} \end{bmatrix}$$

Using the gravity center approximation for r (eq. (4.11)) and the analytical integrals (4.13), we can finally calculate the local matrices (4.16) and (4.17) explicitly, thus having:

$$\mathbf{H}_e = \frac{\pi \overline{r}_e}{2\Delta_e \gamma} \left(k_{h,e} \begin{bmatrix} b_i^2 & b_i b_j & b_i b_m \\ b_j b_i & b_j^2 & b_j b_m \\ b_m b_i & b_m b_j & b_m^2 \end{bmatrix} + k_{v,e} \begin{bmatrix} c_i^2 & c_i c_j & c_i c_m \\ c_j c_i & c_j^2 & c_j c_m \\ c_m c_i & c_m c_j & c_m^2 \end{bmatrix} \right) \tag{4.18}$$

$$\mathbf{P}_e = \left[\phi\beta + c_{br}\left(\alpha - \phi\right)\right]_e \frac{\pi \overline{r}_e \Delta_e}{3} \begin{bmatrix} 1 & 1/2 & 1/2 \\ 1/2 & 1 & 1/2 \\ 1/2 & 1/2 & 1 \end{bmatrix} \tag{4.19}$$

Note that the elastic stiffness, flow stiffness, and capacity matrices are symmetric and positive definite. After assembling the local matrices (4.14), (4.15), (4.18), and (4.19), the finite difference scheme (1.13) is used with $\theta = 0.5$, thus yielding the Crank-Nicolson second-order scheme. The final linear system (1.14) to be solved for different time steps therefore has the following coupled matrix and right-hand term:

$$\mathbf{A}_{\Delta t} = \begin{bmatrix} 0.5\mathbf{K} & -0.5\mathbf{Q} \\ \dfrac{\mathbf{Q}^T}{\Delta t} & \dfrac{\Delta t \mathbf{H} + 2\mathbf{P}}{2\Delta t} \end{bmatrix}$$

$$\mathbf{b}_t = \begin{bmatrix} -0.5\mathbf{K} & 0.5\mathbf{Q} \\ \dfrac{\mathbf{Q}^T}{\Delta t} & \dfrac{2\mathbf{P} - \Delta t\mathbf{H}}{2\Delta t} \end{bmatrix} \begin{Bmatrix} \boldsymbol{\delta}_t \\ \mathbf{p}_t \end{Bmatrix} - \frac{1}{2} \begin{Bmatrix} \mathbf{f}^u_{t+\Delta t} + \mathbf{f}^u_t \\ \mathbf{f}^p_{t+\Delta t} + \mathbf{f}^p_t \end{Bmatrix}$$

This coupled finite element model has been developed according to the so-called "total stress" formulation. Following the "pore pressure gradient" formulation would have led to the same global terms through different local matrices, with the addition of a linear integral extended over the domain boundary. For a thorough discussion of the different properties and practical applications of the two formulations in coupled and uncoupled models, see Ferronato *et al.* [1999] and Gambolati *et al.* [2001a].

4.2.2 Withdrawal distribution

The system's source of stress is the pore pressure decline Δp experienced by the producing formation during extraction. From a mathematical viewpoint, Δp can be prescribed by either Dirichlet or Neumann conditions over a number of nodes within or in the boundary of the depleted volumes. As we know, when the Dirichlet conditions are used, the Δp value is assigned at each node by properly modifying the corresponding matrix row and right-hand component, while with the Neumann conditions a pumping rate Q equating the fluid volume extracted from the elemental porous volume associated with each node in the time unit is specified. We chose to adopt Neumann conditions in the producing reservoirs using the withdrawal rate function $Q(t)$ shown in Figure 4.1, with the Q^* value calibrated in each ideal scenario so as to obtain an average Δp of 10 MPa in the depleted volume after n years of pumping. This is done to get comparable results, in terms of pore pressure distribution and vertical deformation, from the different simulations by only calibrating the Q^* parameter.

In the numerical analysis of simulated deformations along a vertical test hole monitored by an ideal marker tool, a simplified axi-symmetric setting was assumed, with the markers installed along the symmetry axis. In order to reproduce a realistic pore pressure distribution in the porous medium surrounding the monitored vertical axis, fluid pumping can take place as follows:

1. $Q(t)$ is uniformly pumped from an annular volume. In this case, the monitoring well is assumed to be located in a gravity center position with respect to the producing wells. In the innermost zone around the symmetry axis the horizontal pore pressure gradient is practically zero, as is usually the case in producing gas reservoirs;

2. $Q(t)$ is uniformly withdrawn from a cylindrical volume whose axis coincides with the

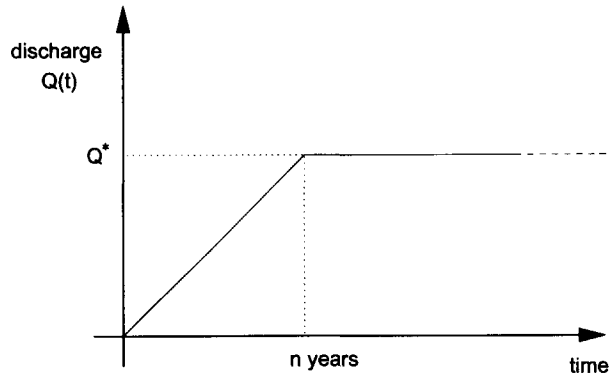

Figure 4.1: Pumping rate used in the numerical simulations. The value Q^* is calibrated in each scenario to obtain an average 10 MPa pore pressure decline in the depleted volume after n years of production.

monitoring well. In this pumping configuration, a near-uniform Δp is reproduced in the field, with a very gentle horizontal pressure gradient;

3. $Q(t)$ is extracted from a vertical line sink coinciding with the symmetry axis. This simulates a monitoring well which is also a producing well, thus generating a significant horizontal pressure gradient around the markers' vertical axis.

It can be shown numerically that the pore pressure fields, and hence the related stresses and strains, generated by the withdrawal scenarios 1. and 2. are very similar, so only the results obtained with scenarios 2. and 3. are discussed in the sequel, without loss of generality. The two withdrawal distributions will be denoted as volume sink (point 2.) and line sink (point 3.), and basically differ in the intensity of the horizontal gradients generated around the marker test hole. Since the volume sink problem can be solved with different radii R of the cylindrical depleted medium, the line sink case can also be seen as the volume sink limit as R approaches zero.

4.2.3 FE mesh and boundary conditions

The purpose of the present numerical study is to analyze the vertical displacements that could be recorded by an ideal marker tool in producing reservoirs with a heterogeneity scale smaller than the marker spacing size. As shown in chapter 3, this is typically the case of the Northern Adriatic boreholes.

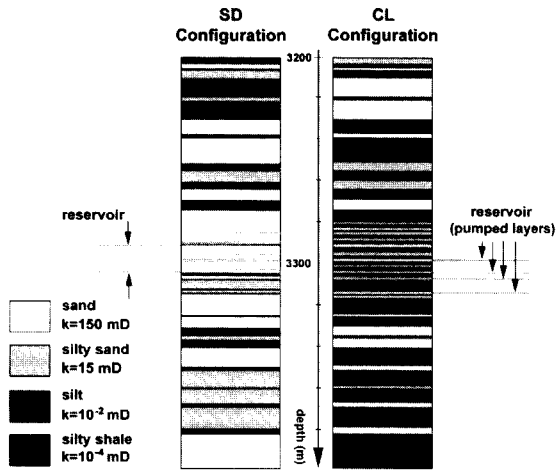

Figure 4.2: Detailed litho-stratigraphy used in the SD and CL configurations in the 3200-3400 m depth range. The reservoir burial depth is approximately 3300 m. The cumulative thickness of the producing layers is 13 and 4 m, respectively. The estimated intrinsic permeability of each lithotype is indicated in the legend.

Electrofacies analysis suggests that the Northern Adriatic gas-bearing formations consist of compacted sand structures confined by thin shale caprocks (see as an example Figure 3.4) or several thin productive sand layers frequently interbedded with low permeable beds (e.g. Figure 3.6). Based on these electric log sequences, two typical litho-stratigraphies of the Northern Adriatic boreholes have been reproduced using four lithotypes, as shown in Figure 4.2. In the leftmost porous column (configuration SD) a 13 m thick reservoir is confined by shale layers about 1 m thick, while in the rightmost sample (configuration CL) four productive 1m-thick sand layers are incorporated into a mainly clayey porous matrix. In Figure 4.2 each lithotype is also characterized by an estimated intrinsic permeability, which is converted into coherent units by equation (3.19).

Above and below the detailed porous columns in Figure 4.2, the model is completed by a sequence of alternating sand and clay layers. The mechanical properties of the medium are described by the constitutive law (3.13) for virgin loading conditions, with the Biot coefficient defined in Figure 3.11.

A high resolution mesh is needed to provide a satisfactory reproduction of the detailed litho-stratigraphies of Figure 4.2. Figure 4.3 shows the triangular discretization along a vertical cross-section, with the global size of the simulated cylindrical porous volume. Minimum vertical and radial spacings of 1 m are used in the most refined region in the

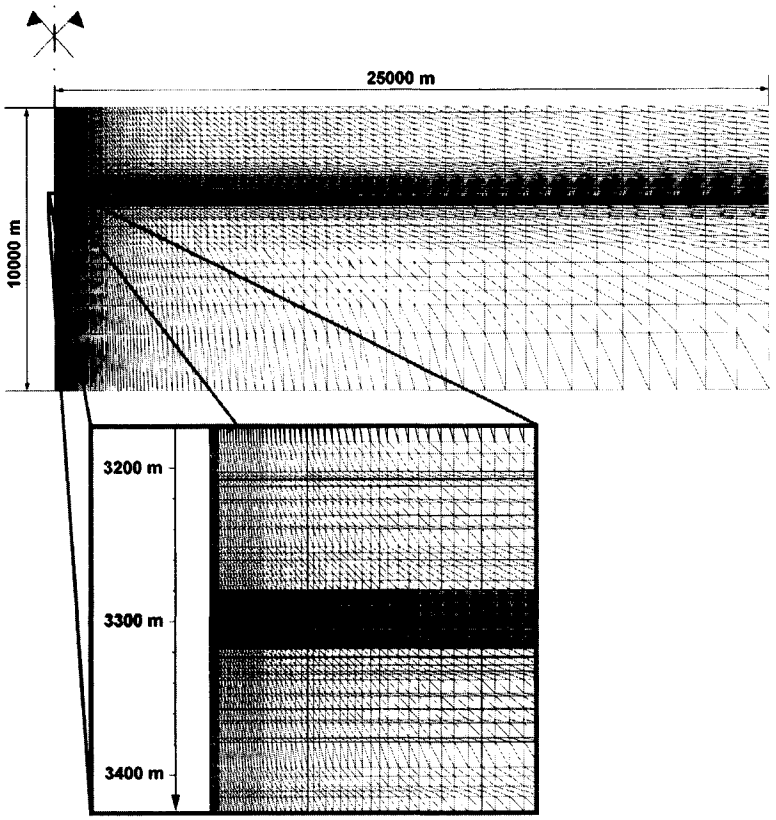

Figure 4.3: Vertical cross-section of the FE mesh used in the simulations.

vicinity of the symmetry axis. Standard Dirichlet boundary conditions are specified far enough away from the depleted volumes to avoid any appreciable influence on the final results. A rigid basement 10000 m deep is assumed, with a fixed outer boundary with zero Δp 25000 m away from the symmetry axis. Dirichlet conditions with zero Δp are also assumed on the top traction-free surface [Baù *et al.*, 2003]. The resulting FE mesh, used for both the SD and the CL configurations, comprises 19908 nodes and 39250 elements, with an overall system size of 59724.

As discussed in detail in chapter 1, the final linear system is repeatedly solved for increasing time steps Δt by using Bi-CGSTAB [Van der Vorst, 1992] preconditioned with the incomplete LU decomposition with partial fill-in ILUT(ρ, τ) [Saad, 1994]. In most

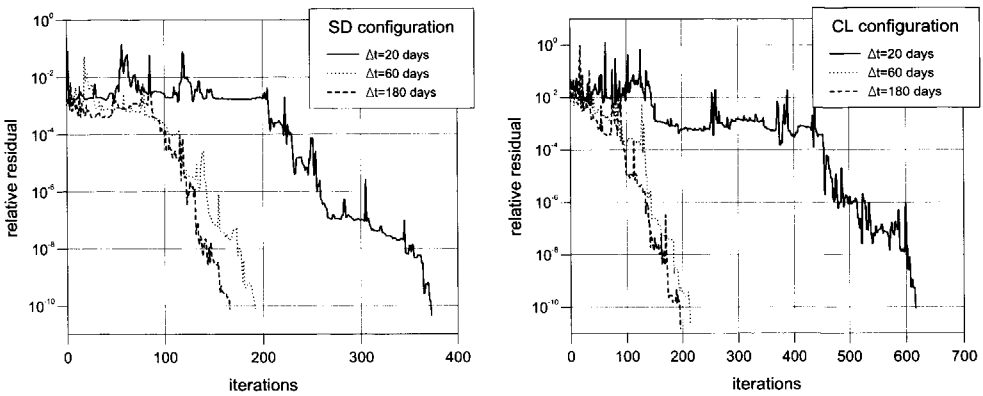

Figure 4.4: Convergence profiles obtained with preconditioned Bi-CGSTAB and LSL preliminary scaling in a few representative simulations for different time steps.

simulations the optimal values for ρ and τ turned out to be 25 and 10^{-3}, respectively, but in difficult cases with low permeabilities and time steps close to the critical Δt [Ferronato *et al.*, 2001], ρ and τ had to be set to 45 and 10^{-5}. In each solution, a preliminary Least Square Log scaling (see chapter 1) [Curtis and Reid, 1972] is performed. The critical time step was found experimentally to range between 10 and 20 days according to the different scenarios, so a minimum Δt of 20 days was always used.

The numerical solution to the resulting linear system obtained with the aforementioned techniques is quite efficient. An example of a few representative convergence profiles with different time steps is provided in Figure 4.4.

4.3 Flow, strain and stress fields

The withdrawal rate (Figure 4.1) was prescribed in the reservoirs of both SD and CL configurations using $n = 2$ years. The solution is obtained in terms of pore pressure distribution, strain and stress fields, and represented graphically in Figures 4.5, 4.6, and 4.7. All maps illustrate the situation after 2 years of starting production, i.e. at the end of the initial linear portion of the pumping rate profile used as the forcing function, in the surroundings of the depleted reservoir for both the volume and the line sink scenarios, also showing the local litho-stratigraphy (SD or CL). We have four different basic scenarios, i.e. SD with volume and line sinks, and CL with volume and line sinks.

As other authors have also pointed out [Verruijt, 1969; Hsieh, 1996; Gambolati *et*

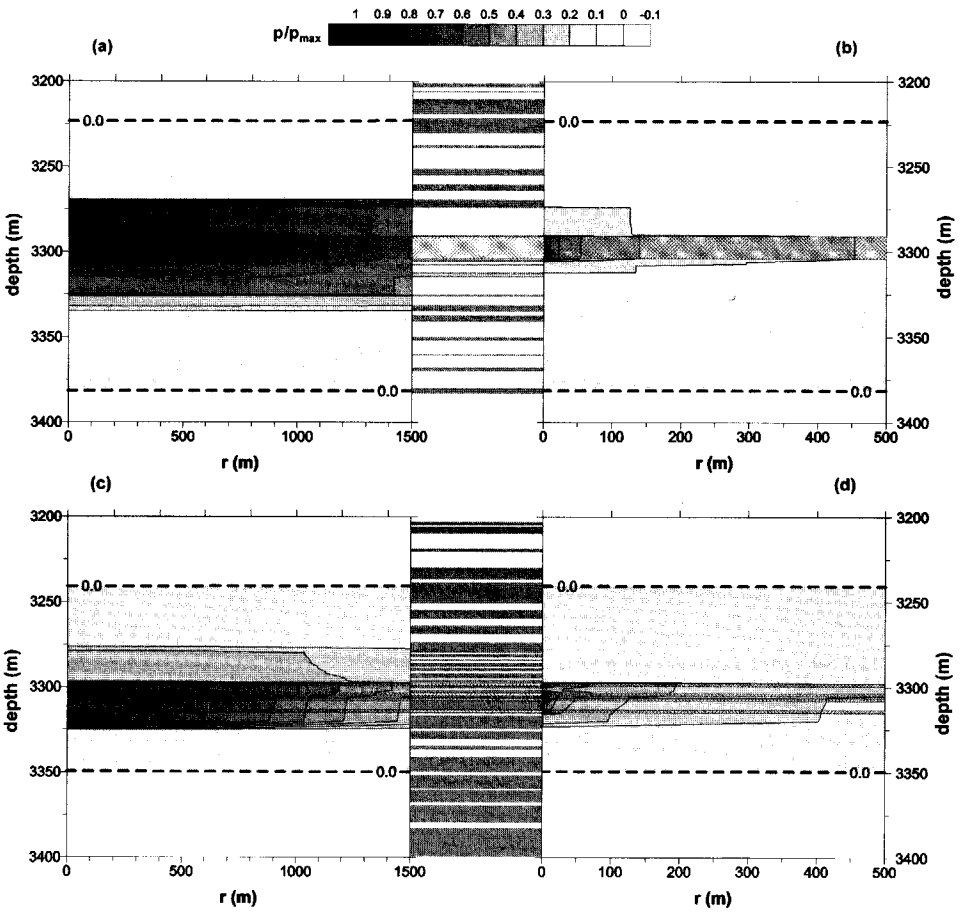

Figure 4.5: Pore pressure variation relative to the maximum pore pressure decline after two years of pumping: (a) SD scenario with volume sink; (b) SD scenario with line sink; (c) CL scenario with volume sink; (d) CL scenario with line sink. Litho-stratigraphies (clays are shaded gray) and the depleted layers (hatched areas) are also shown.

al., 2000; Gutierrez *et al.*, 2001; Pao *et al.*, 2001; Baù *et al.*, 2001], a slight overpressure develops above and below the depleted layers because of the coupling effect between fluid flow and medium deformation. The importance of this overpressure and the distance between the area affected and the producing reservoirs basically depend on the thickness and permeability of the confining shales. For instance, in cases with a thick impermeable ($k = 0$) caprock above gas/oil productive horizons, overpressures may reach 40% of the maximum drop in pore pressure [Gutierrez *et al.*, 2001]. In the hydro-geomechanical setting of the Northern Adriatic boreholes, however, they are always much less than 10% (see Figure 4.5). The thick clay deposits of the CL scenario reduce the distance between the overpressure zones and the depleted layers compared with the SD scenario, while the withdrawal distribution (volume or line sink) appears to have no significant impact.

The maps of vertical strain relative to the maximum compaction simulated in each case, are given in Figure 4.6. Consistent with the analytical solution of Geertsma model (see section 2.3), the medium expands vertically above and below the producing formation. The shape of the expanding regions and their distance from the depleted layers are not the same as those of the overpressure zones (see Figures 4.5 and 4.6) and depend on both the geological scenario (SD or CL) and the pumping configuration. We can notice that vertical expansions still occur in steady state, albeit at a greater distance from the reservoir, when the overpressures have already dissipated. This is in line with the behavior qualitatively captured by Geertsma model and suggests that medium expansion is related mainly to three-dimensional deformation of the porous volume rather than to coupling, though the latter may play an important role in the early stage of pumping at least. Finally, expansion is influenced by the extraction scenario, and hence by the horizontal pressure gradients generated around the monitored vertical axis. With line sink, expansion occurs closer to the producing layers, with a maximum value of 5% of compaction, whereas with volume sink the maximum expansion achieves only 1.3% of compaction. The latter is consistent with Geertsma's prediction, according to which vertical strain is much smaller outside a uniformly-depleted (i.e. no horizontal pressure gradients around the symmetry axis) disc-shaped reservoir than inside (see section 2.3).

The analysis of reservoir compaction within heterogeneous porous media is completed by addressing the stress invariants characterizing both a depleted and an expanding rock sample, as simulated by the coupled FE model. It is worth noting here that, in an axi-symmetric setting, the stress invariants p' and q are:

$$p' = -\frac{1}{3}(\sigma_{rr} + \sigma_{zz} + \sigma_{\theta\theta})$$

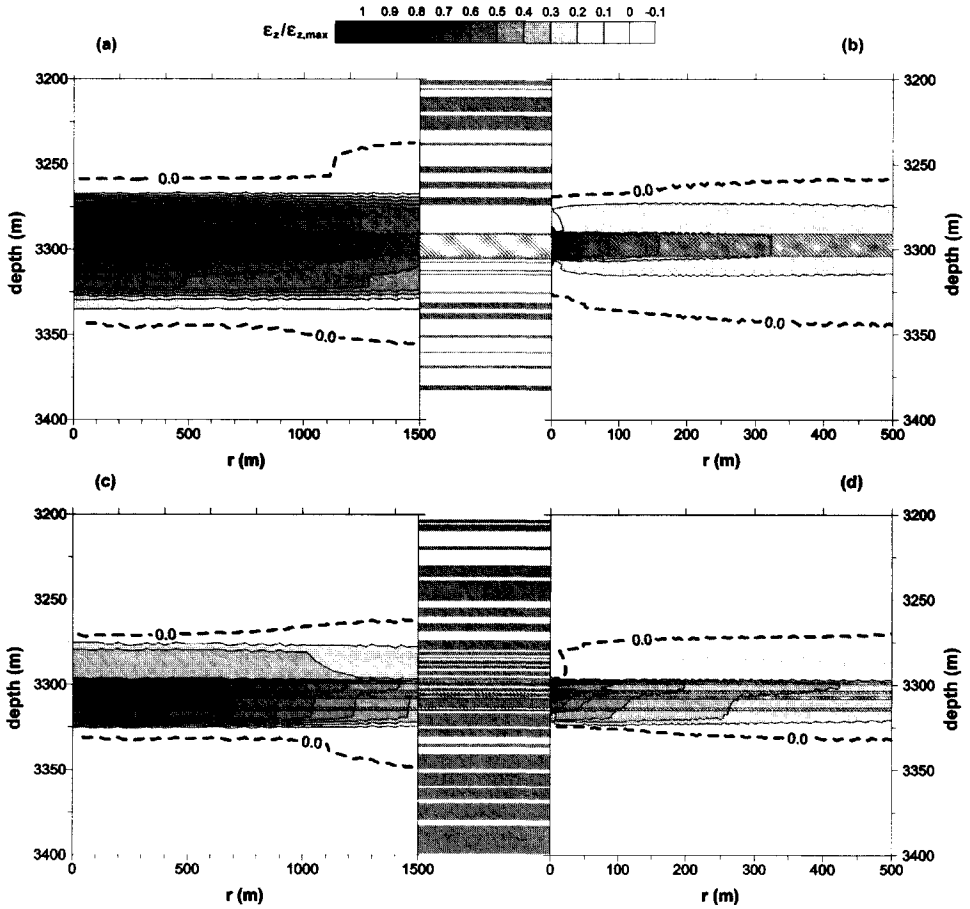

Figure 4.6: Vertical strain relative to the maximum value after two years of pumping: (a) SD scenario with volume sink; (b) SD scenario with line sink; (c) CL scenario with volume sink; (d) CL scenario with line sink. Litho-stratigraphies (clays are shaded gray) and the depleted layers (hatched areas) are also shown.

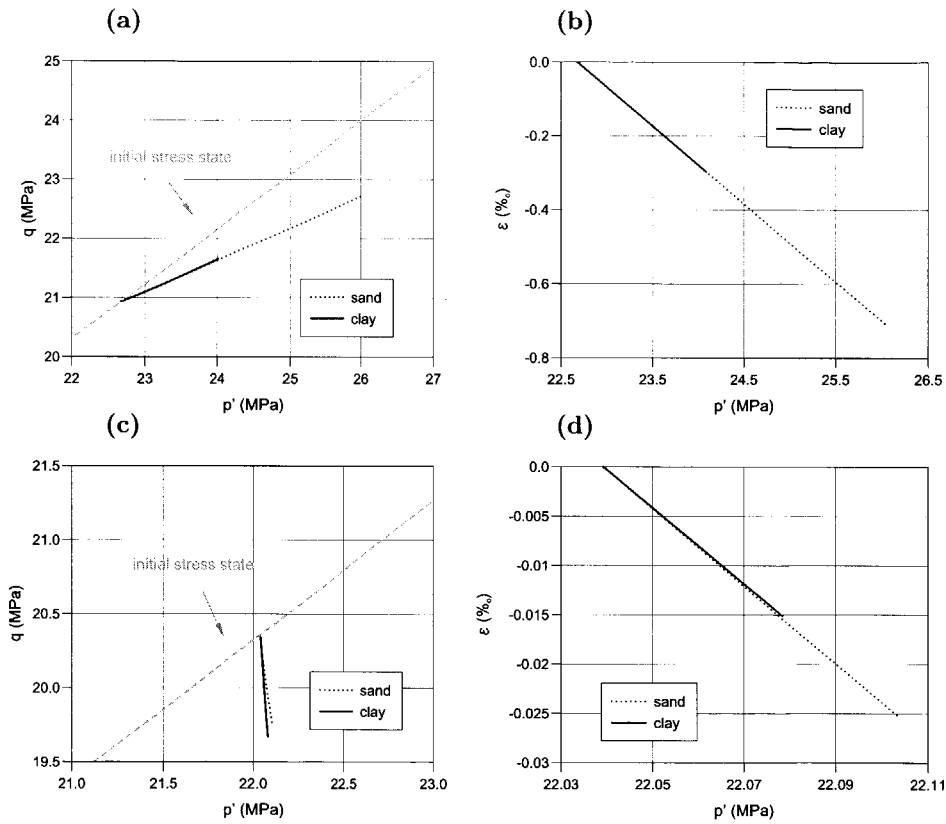

Figure 4.7: (a) q and (b) ϵ vs p' for depleted rock layers; (c) q and (d) ϵ vs p' for porous medium surrounding the depleted layers.

$$q = \sqrt{\sigma_{rr}(\sigma_{rr} - \sigma_{zz}) + \sigma_{zz}(\sigma_{zz} - \sigma_{\theta\theta}) + \sigma_{\theta\theta}(\sigma_{\theta\theta} - \sigma_{rr}) + 3\sigma_{rz}^2}$$

where σ_{ij} indicates the effective intergranular stress. Figure 4.7 shows the profiles q vs p' and ϵ vs p' calculated in a generic sand element within the depleted reservoir, in a generic clay element confining the depleted reservoir (Figures 4.7a and 4.7b), and in generic sand and clay elements within the expanding and overpressure region (Figures 4.7c and 4.7d). Stress invariant changes are compared with the initial stress profile:

$$q_0 = \frac{3(1 - K_0)}{1 + 2K_0} p_0'$$

with $K_0 = \sigma_{rr}/\sigma_{zz}$ in undisturbed conditions.

As expected, the sand and clay layers, respectively within and confining the reservoir, undergo a p' increase due to the drop in pore pressure, with a corresponding volume reduction (Figure 4.7b). Stress change and volumetric deformation are obviously lower in the clay layer since the pore pressure decline is smaller here than in the reservoir. Outside the depleted formation, rocks undergo vertical stress unloading, especially in the early pumping phase, but this is compensated by a horizontal stress increment, so overall the medium experiences a volume reduction (Figure 4.7d) that accounts for the onset of a slight overpressure. This is the basic mechanism behind the coupling effect. As consolidation proceeds, pore fluid (groundwater) flows out of these volumes and the overpressure gradually dissipates, but the vertical expansion may still persist.

4.4 Simulated marker response

As shown in detail in chapter 2, radioactive markers record the vertical deformation Δu_z occurring between two points about 10.5 m apart. In our FE implementation, we assumed an ideal marker tool to be installed along the symmetry axis, so the simulated measurements at time t referred to the midpoint depth of the pair of markers can be calculated as:

$$\Delta u_z(z,t) = \int_{z-5.25}^{z+5.25} \epsilon_z(r = 0, \zeta, t)\, d\zeta \tag{4.20}$$

where the vertical strain ϵ_z is obtained from FE numerical simulations for the different selected scenarios. Equation (4.20) is plotted vs depth for selected times in the neighborhood of the producing formations, thus giving the vertical deformation of a simulated heterogeneous 10.5 m wide interval along the monitoring axis.

Figures 4.8 and 4.9 show the outcome of equation (4.20) at various times after starting production until steady state is reached for the SD and CL configurations, and for

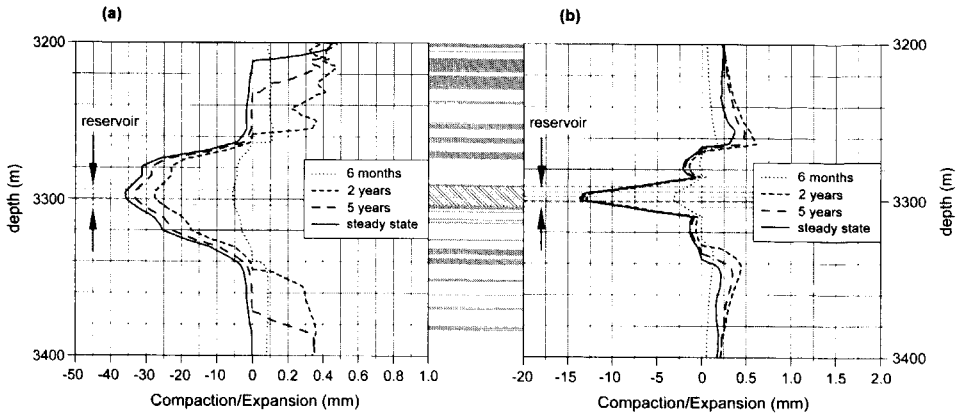

Figure 4.8: Simulated marker response (from eq. (4.20)) vs depth at different times in the SD scenario with: (a) volume sink; (b) line sink. The litho-stratigraphy is also shown. Compactions and expansions are depicted using different scales.

volume and line sink, respectively. As expected from the strain maps of Figure 4.6 and the Geertsma model prediction of chapter 2, the reservoir always compacts and small expansions above and below the producing layer occur. A different scale has been used for compactions and expansions in Figures 4.8 and 4.9, as well as in the ones that follow, to make the latter more easily readable. Expansions vary from 1% (SD with volume sink) to 10% (CL with line sink) of the field compaction and appear to be very sensitive to the withdrawal distribution. In particular, they usually increase with a line sink – basically because of the additional contribution of the greater horizontal stress. Moreover, expansions move farther from the reservoir as the simulation proceeds, and persist in steady state conditions. It is also worth noting the pronounced Δu_z variation occurring close to the shale beds confining the depleted volume, especially emphasized by the line sink pumping condition. This would suggest that the measured deformation, and hence the related compressibility estimate, are quite sensitive to the marker's actual location.

In order to grasp the influence of the hydro-geomechanical properties of the porous medium on the radioactive marker's response, a sensitivity analysis was performed by varying rock compressibility, shale permeability, and the Biot coefficient. The results from the four basic scenarios are shown in Figures 4.10 through 4.12 at time $t = 2$ years after the production started.

In Figure 4.10 the uniaxial compressibility $c_{M,tb}$ of the top and bottom layers confining

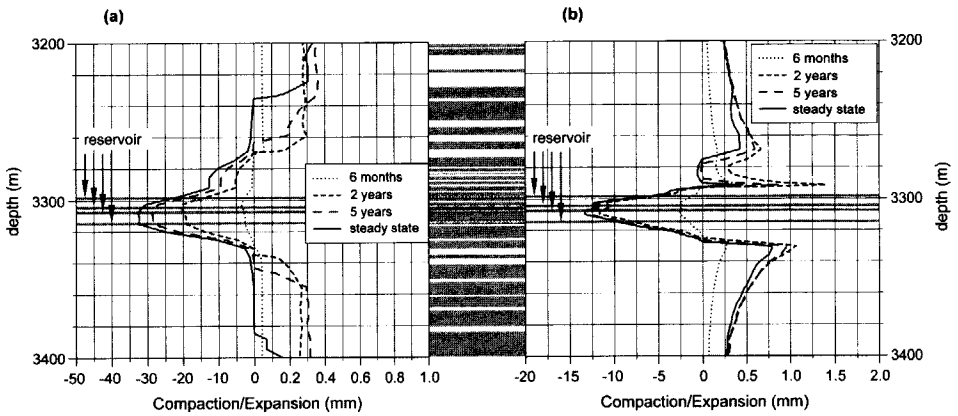

Figure 4.9: The same as Figure 4.8 for the CL scenario.

the producing formations is first halved (i.e. stiffer caprock), then doubled (i.e. softer caprock) with respect to the c_{M0} value provided by the selected constitutive law (3.13). Compaction of the depleted reservoir is uninfluenced by the compressibility contrast with the confining beds, while a variation is noticed in the marker spacings incorporating the stiffer or softer layers, as expected. A slight change is also found in the small expansion simulated in the lower part of the porous medium. However, differences due to rock compressibility contrasts can only be observed in the volume sink cases (and especially with the SD scenario), while in the line sink case the radioactive marker response appears to be practically unchanged.

The permeability values k_{cl} of the clay formations play a more important part in determining radioactive marker response, as shown in Figure 4.11 for the different simulated scenarios. k_{cl} was reduced by 2 and 4 orders of magnitude from the initial k_{cl0} value calculated using equation (3.19) with the estimates reported in Figure 4.2. As k_{cl} decreases, Figure 4.11 exhibits an increase in maximum expansion value, which is more pronounced with line sink extraction – achieving 12-13% of the corresponding field compaction. We can also see that the expansion regions come closer to the reservoir. Moreover, permeability variation influences reservoir compaction, and hence the estimation of its compressibility, in the CL scenario, i.e. when the producing layers are incorporated into a mainly clayey porous matrix. This suggests that such a lithological configuration is unlikely to give rise to reliable radioactive measurements of c_M.

Finally, the influence of the Biot coefficient on the simulated marker response was in-

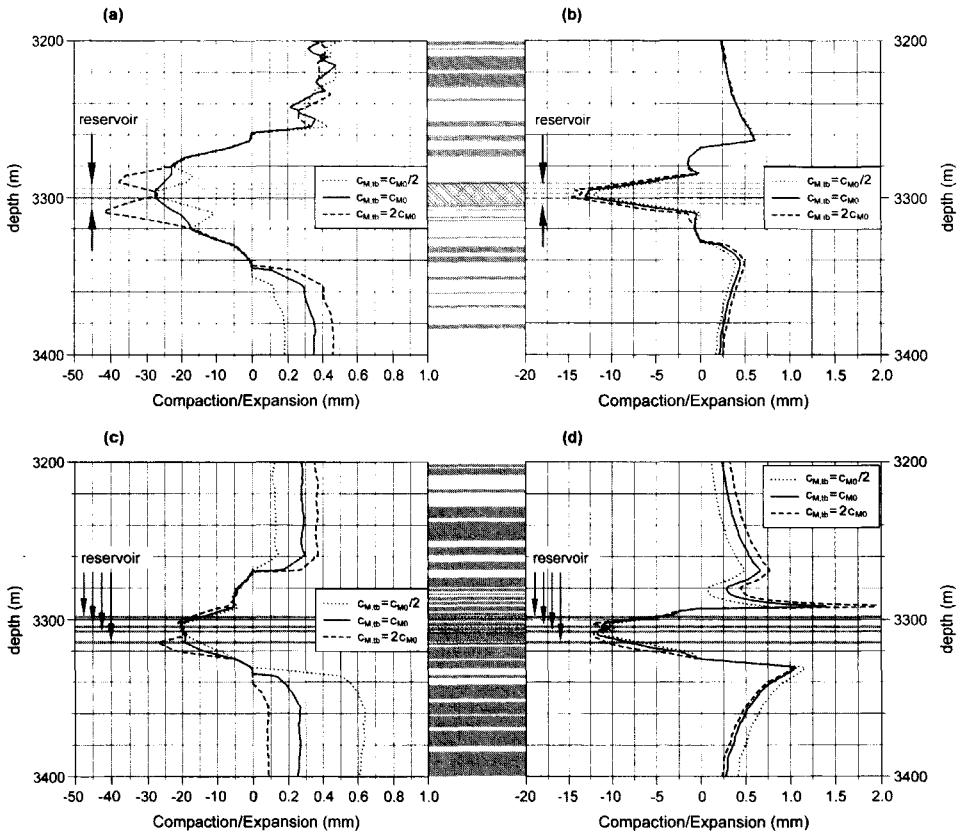

Figure 4.10: Sensitivity analysis in relation to rock compressibility: (a) SD scenario with volume sink; (b) SD scenario with line sink; (c) CL scenario with volume sink; (d) CL scenario with line sink. Marker response is simulated two years after starting production.

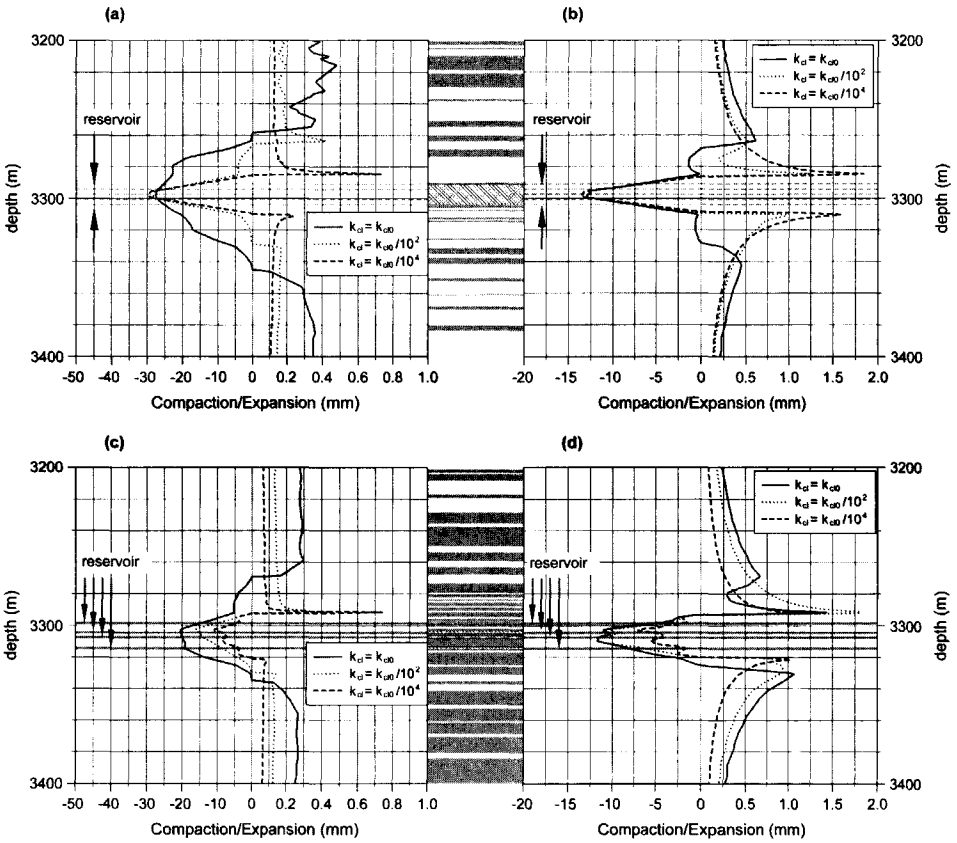

Figure 4.11: The same as Figure 4.10 for shale permeability.

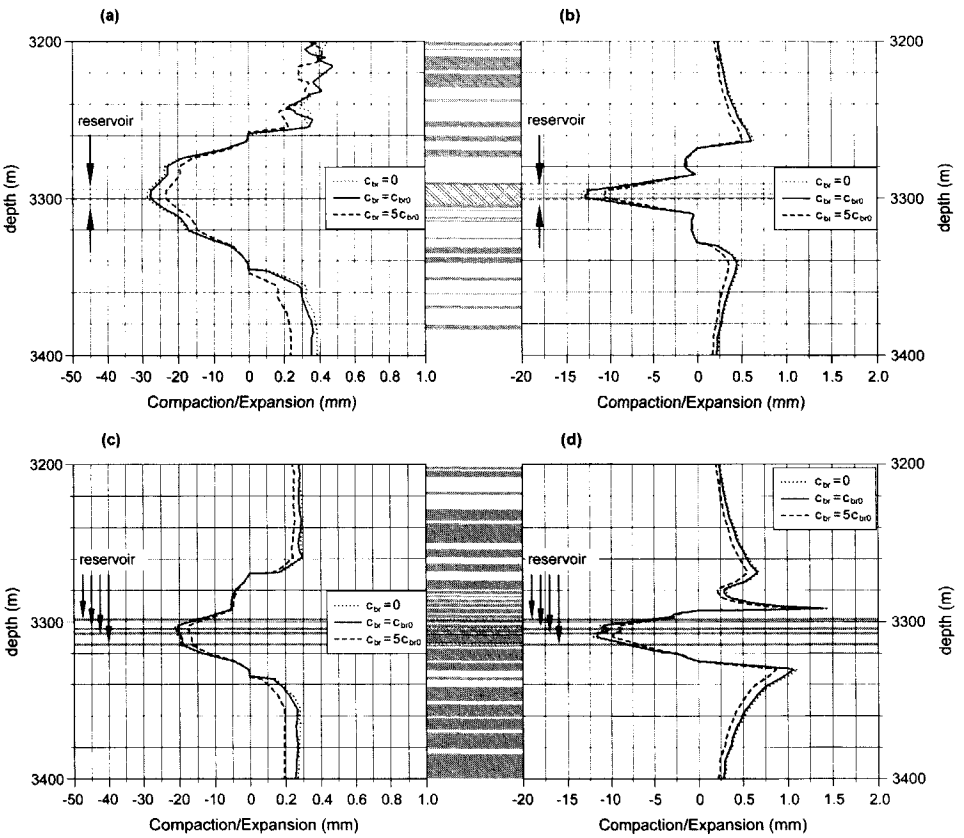

Figure 4.12: The same as Figures 4.10 and 4.11 for the Biot coefficient.

vestigated by varying the grain compressibility coefficient in equation (3.16). Solid grains were assumed to be either incompressible ($c_{br} = 0$, $\alpha = 1$) or 5 times more compressible than the basic value c_{br0} (see section 3.3.3), thus obtaining $\alpha \simeq 0.85$, i.e. the typical Biot coefficient of the Northern Adriatic basin at a depth of about 10000 m (see Figure 3.11). The results in Figure 4.12 show that this parameter does not significantly affect the marker response. In particular, the simplifying assumption of incompressible grains, i.e. $\alpha = 1$, is quite acceptable.

4.4.1 Critical situations for marker measurements

As extensively discussed in chapters 2 and 3, the importance of the radioactive marker technique relies on its ability to provide a reliable uniaxial compressibility estimate based on actual in situ compaction measurements. This is feasible where the assumption of one-dimensional deformation, leading to equation (2.6), holds true. So, though they are realistically recorded by radioactive markers in terms of actual mechanical behavior of the local rock, expansion data coinciding with a drop in pore pressure occurring within the monitored interval, or reduced compactions due to non-negligible lateral deformations, i.e. non-oedometric conditions, cannot contribute to the c_M estimate. To obtain a more efficient marker installation, so as to improve in situ measurement reliability for compressibility estimates and save large amounts of money, some of the most critical layering configurations must be preliminarily recognized.

Based on the results of the sensitivity analysis performed in the previous section, the case of thin producing layers embedded within a nearly impermeable clay matrix may severely affect the proper use and interpretation of marker data. In fact, spanning 10.5 m wide intervals may incorporate expanding rock formations which can partially or even totally offset reservoir compaction. As an example, Figure 4.13 shows the results obtained at different times from two critical layering configurations. In Figure 4.13a, a 1 m thick sand layer is depleted by a line sink with $k_{cl} = k_{cl0}/10^4$. An expansion corresponding to up to 20% of the field compaction occurs less than 5 m away from the depleted layer, so a given marker spacing incorporating the reservoir could still expand. Moreover, the very steep deformation profile above and below the field makes marker response very sensitive to the bullet's actual location. These effects can be magnified by the simultaneous depletion of a second thin reservoir located a few meters away from the previous producing layer. Assume a second reservoir located 17 m below the first. The expansion increases up to 25% (Figure 4.13b) of field compaction, and, especially in the

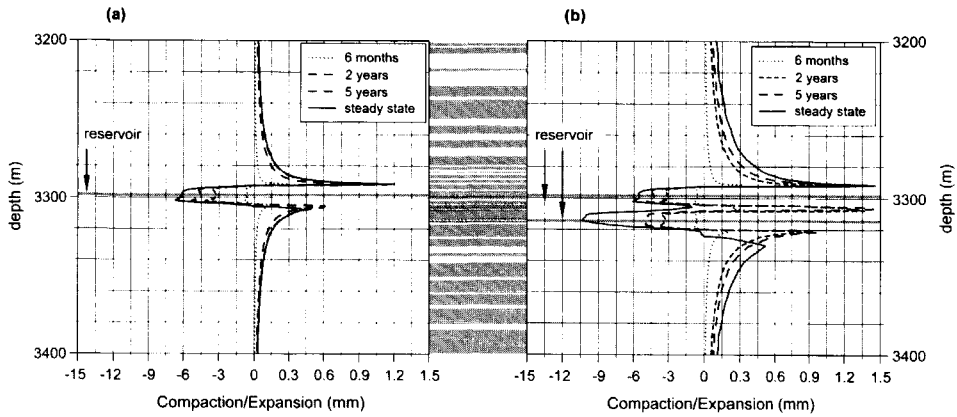

Figure 4.13: Simulated marker response vs depth in the CL scenario with line sink, $k_{cl} = k_{cl0}/10^4$, and: (a) 1 depleted layer; (b) 2 depleted layers.

relatively early production stages, the unproductive formation between the two reservoirs may expand significantly. In this case, radioactive markers may point to an expansion despite pore pressure data indicate an overall decline, thus providing measurements that are unreliable for the purpose of estimating the local uniaxial compressibility.

Another way to get an idea about the reliability of in situ marker measurements for the c_M calculation is to derive an "a posteriori" compressibility value from the simulated marker response and compare it with the constitutive law (3.13) used in the FE model. An indication of the reliability of the radioactive marker results is provided by the extent to which they match the compressibility value of equation (3.13).

The results of the "a posteriori" c_M are shown in Figure 4.14 for the four basic simulations described in section 4.3. To calculate the "a posteriori" c_M the simulated marker measurements and pore pressure distributions of Figures 4.8, 4.9, and 4.5 were used at time $t = 2$ years after pumping started. Obviously, the "a posteriori" c_M can only be computed over compacting depth intervals undergoing a pore pressure decline. The results obtained in the SD scenario with a volume distributed withdrawal are quite satisfactory. The CL scenario with volume sink also exhibits a fairly good agreement with the actual c_M, though the compacting depth interval is smaller and the oscillations of the estimated c_M around the actual value appear to be more pronounced than in the SD scenario. By contrast, the outcome of the line sink simulations (i.e. the monitoring well is also productive) fluctuates quite significantly in both scenarios, underestimating c_M by

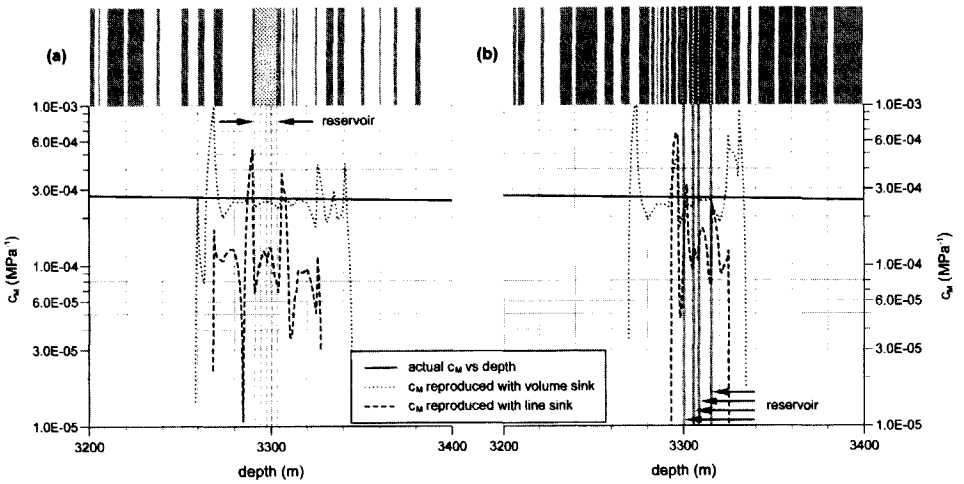

Figure 4.14: "A posteriori" c_M estimate using the simulated marker response and pore pressure drawdown in: (a) SD scenario; (b) CL scenario.

approximately 30% on average and locally much more. This result of course neglects the technological difficulties that can arise when the marker wellbore coincides with a producing wellbore, causing possible movements of the radioactive bullets from their original location and thus making it difficult to measure the actual marker spacing deformation during production [Mobach and Gussinklo, 1994]. In this case, the underestimation of c_M is basically due to the horizontal pressure gradients generated around the extraction well, which oppose vertical compaction more than in an oedometer and make the assumption of uniaxial deformation largely questionable.

In conclusion, the radioactive marker technique appears to be genuinely capable of providing a reliable estimate of the uniaxial compressibility c_M, as is proven by the "a posteriori" c_M calculation and comparison with the constitutive law (3.13) used in the simulations. However, great caution is required in the critical situations which can pose serious problems for the proper use of marker data. In particular, critical configurations can occur in litho-stratigraphic sequences similar to the CL scenario, where a few thin depleted layers are incorporated into basically low permeable clay formations, and when the monitoring well is close to, or even coincides with, an extraction well.

4.5 Conclusions

Radioactive marker response in heterogeneous reservoirs was simulated using a FE coupled consolidation model implemented in an axi-symmetric setting. The rock's vertical deformation on marker scale (10.5 m) was analyzed in two realistic highly-detailed litho-stratigraphic sequences typical of the Northern Adriatic sedimentary basin, one consisting mainly of sand interbedded with thin clay layers (SD scenario), the other composed of thin sand productive formations incorporated into a mainly shale matrix (CL scenario). Both litho-stratigraphies are taken from real sedimentary sequences detected by electrofacies. Two different pumping scenarios were implemented, one reproducing a monitoring test hole far enough away from the producing wells uniformly distributed within the field (volume sink, with gentle horizontal pressure gradients around the marker wellbore), and the other a monitoring test hole coinciding with a producing well (line sink, with significant horizontal pressure gradients around the marker wellbore). The most recent and reliable hydro-geomechanical data set on the Northern Adriatic basin, discussed in chapter 3, was used in the simulations.

The following points are worth emphasizing:

- depletion of deep heterogeneous reservoirs induces vertical rock expansions in the surrounding porous medium. Expansions are mainly related to the three-dimensional deformation of the porous medium and to the geological layering surrounding the depleted volumes, with coupling only initially contributing to the process. In some particular configurations, radioactive markers can record an expansion despite a drop in pore pressure occurring in the monitored depth interval;

- marker-scale hydraulic vertical heterogeneity plays a very important role in both the magnitude and the location of expanding zones. Where clay prevails over sand, with producing layers incorporated into very low permeable rock formations, significant expansions (up to 25% of field compaction in our test cases) can occur on the marker scale. Local stiffness contrasts do not influence the measurements obtained from adjacent markers and are well reproduced provided that horizontal pressure gradients are small in the vicinity of the monitoring wellbore. Grain compressibility does not significantly affect marker response, so the usual assumption of rigid solid grains ($\alpha = 1$) is quite acceptable;

- critical configurations can be found where expansions may be recorded by radioactive markers even though the marker spacing incorporates producing layers where

the pore pressure diminishes. This situation must be avoided in marker installation, since the resulting data cannot be used for the estimation of uniaxial rock compressibility;

- even leaving aside the technological problems involved, installing radioactive markers in producing wells gives rise to reduced compactions (and consequently unreliable c_M) due to horizontal deformation caused by local extraction, which undermines the assumption of oedometric compaction.

In conclusion, the radioactive marker technique is a promising tool for the realistic assessment of the actual mechanical properties of a producing reservoir. Great care must be paid to the configurations involved, however, which can easily give rise to difficulties and uncertainties in the interpretation of marker data. A detailed knowledge of the lithostratigraphic sequences of producing heterogeneous reservoirs consequently appears to be of paramount importance for a genuinely effective implementation of the radioactive marker technique.

Chapter 5

Radioactive marker interpretation in the Northern Adriatic gas fields

When the field consists of multi-pay reservoirs with the heterogeneity scale of the porous medium smaller than the marker spacing (10.5 m) a great care must be exercised in the interpretation of a radioactive marker survey. The rock may expand, or, if the monitored depth interval incorporates thin low permeable layers or the measurement is made in an active well, the measured compaction can occur in non-oedometric conditions. In the present chapter a set of radioactive marker measurements made by ENI-Divisione Agip over the last decade in 3 deep boreholes of the Northern Adriatic basin are simulated with the aid of the FE coupled poroelastic model developed in the previous sections. The modeling results show that the measurements can be reproduced satisfactorily in several case, both from a qualitative and also quantitative viewpoint, and indicate that an efficient marker installation requires that the monitored depth interval be made mostly of sand entirely depleted, with the markers placed far from a producing well and approximately 10.5 m apart. The c_M constitutive law used in the numerical analysis appears to be realistically accurate for a depth larger than 2500 m and generally underestimated between 800 and 1500 m. The measured expansions due to a natural pore pressure recovery allow for the assessment also of the reservoir c_M under unloading/reloading conditions.

5.1 Introduction

The structural setting of the Northern Adriatic basin [Haan and Arnott, 1991; Mattavelli *et al.*, 1991] may make it particularly difficult to interpret radioactive marker measure-

ments. This is mainly due to the vertical medium heterogeneity over a smaller scale than the marker monitoring interval, and to the gas accumulation occurring in layered formations even only a few centimeters thick [Ferronato *et al.*, 2003a]. As a major result, a number of marker spacings recorded an unexpected expansion, despite a measured drop in the pore pressure, or a compaction with zero Δp, thus raising concern as to the correct interpretation of such findings. The outcome of marker surveys performed at different times on three wellbores in the Northern Adriatic basin is shown in Tables 2.1 through 2.3 and 3.1, showing measurements which seem to be consistent with the expected medium deformation, along with some anomalous data that must be discarded in the evaluation of the local constitutive model [Baù *et al.*, 2002].

Interpreting marker measurements from the wells instrumented in the Northern Adriatic basin may require an ad hoc non-standard analysis. As shown in chapter 4, this can be done with the aid of a three-dimensional coupled poroelastic model solved by Finite Elements over the scale of the medium vertical heterogeneity as detected by the electrofacies technique. Using this mathematical tool enables marker response in a typical litho-stratigraphic sequence of the Northern Adriatic basin to be simulated, so it can also be used to reproduce numerically the vertical deformation supposedly recorded by radioactive markers along real monitoring wellbores.

The aims of the present numerical study are many-fold. First of all, the reproduction of real field measurements may help validate the coupled poroelastic model and its assumptions, and consequently also the analysis and conclusions developed in chapter 4. Secondly, this FE simulation can indicate the marker spacings that actually compact or expand in oedometric conditions, thus reliably representing the rock uniaxial compressibility. These data alone should be used correctly to estimate the reservoir c_M. At the same time, some anomalous measurements can be interpreted as real deformations due to the field geometry, the medium vertical heterogeneity, or non-oedometric conditions, whereas others can be related to instrumental errors or operational inaccuracy. Thirdly, using the "a posteriori" c_M calculation developed in the previous chapter, the basin-scale compressibility laws derived for the Northern Adriatic, both in virgin loading and in unloading-reloading conditions [Baù *et al.*, 2002], can be validated and also locally calibrated, if necessary. Finally, it may be worthwhile to consider performing a preliminary FE simulation of monitoring wellbores that are to be instrumented in the future, to guide the most appropriate marker installation.

This chapter describes the results obtained using the FE coupled poroelastic model to reproduce the marker data recorded in four surveys performed by ENI-Divisione Agip

over three monitoring boreholes over the last decade. In the analysis that follows, the wells are denoted as 1, 2, and 3. Detailed litho-stratigraphies obtained from electrofacies (Figures 3.4 through 3.6) and static pressure data are provided for each well, together with the main petrophysical properties estimated for the producing layers. High-resolution FE grids are used to represent the local vertical heterogeneity as accurately as possible.

After a brief review of the main features of the coupled poroelastic model used for the numerical experiments, the simulation of the deformations recorded in the surveys on each well is described in detail. The generation of high-resolution meshes on the basis of the available litho-stratigraphic sequences, provided by the electrofacies technique, is presented and discussed, together with the static pressure data of each producing layer. The constitutive model (3.13) is used, updating the compressibility of the previously-depleted layers in relation to the actual effective stress. The unloading-reloading constitutive law (3.14) is used to address the natural pore pressure recovery that occurred in abandoned fields. For each well, different scenarios are simulated, as far as the shale permeability values and the supposed horizontal pressure gradients are concerned, depending on the producing well's location with respect to the monitoring well. The results, comparing the numerical and actual marker measurements, are discussed for the most reliable scenarios, sometimes finding a good consistency between real and simulated deformations even for anomalous marker records, sometimes revealing a poor reproduction most likely related to actual instrumental or modeling inaccuracies. Finally, we draw a number of conclusions as to the reliability of marker data in the simulated wells, the effectiveness of the mathematical model used for the numerical analysis, and the validation of the constitutive laws (3.13) and (3.14).

5.2 Application to the Northern Adriatic boreholes

The radioactive marker measurements performed in three wells in the Northern Adriatic basin are simulated with the aid of the axi-symmetric coupled poroelastic model described in detail in section 4.2.1.

The depletion of each producing layer is reproduced by prescribing a pumping/injection rate $Q(t)$ uniformly distributed within a cylindrical volume with radius R, as in the volume sink case of chapter 4. The value of R is calibrated here in each scenario and basically depends on the average distance of the productive wells from the monitoring borehole in the real field. The pumping rate $Q(t)$ is assumed to vary linearly from 0 at $t = t_i$ to Q^* at $t = t_f$, where t_i and t_f are the initial and final time of simulation, respectively, and Q^*

Lithotype	Permeability k [m/s]	Porosity ϕ
overburden sand	10^{-5}	0.33
overburden clay	10^{-8}	0.33
underburden sand	3×10^{-7}	0.15
underburden clay	5×10^{-11}	0.05

Table 5.1: Permeability and porosity of additional lithotypes used in the FE model of the litho-stratigraphic sequence above and below the depth interval monitored by electrofacies.

is calibrated for each producing layer so as to obtain the average static reservoir pressure measured at t_f in the depleted or repressurized porous volume.

The model domain for each well extends vertically from the top traction-free surface to a rigid impervious basement 7000 m deep. The fixed outer boundary with zero Δp is set 15000 m away from the symmetry axis, and zero Dirichlet boundary conditions on pore pressure are also prescribed over the top surface [Baù *et al.*, 2003]. The depth intervals with the producing layers were monitored using the electrofacies technique to provide the most accurate and detailed description currently available of the vertical lithology. In these intervals the vertical discretization spacing Δz varies from 0.1 to 20 m, according to the local litho-stratigraphic sequence. In the remainder of the porous medium, Δz progressively increases toward the top and the basement. The minimum radial discretization spacing Δr in the vicinity of the symmetry axis is equal to 1 m and is small enough to provide practically no errors using the gravity center approximation (4.11) for the radial coordinate [Gambolati *et al.*, 2001a]. The FE meshes thus generated are made of more than 80,000 elements and totalize more than 40,000 nodes in each well.

The stratigraphic sequences detected by electrofacies are described by the lithotypes indicated in Figures 3.4 through 3.6. For the sake of simplicity, in each well two lithotypes for the permeable sandstone formations and two for silt and shale units are used to represent the litho-stratigraphic reality in the FE model. Four additional lithotypes (overburden sand and clay, underburden sand and clay) are assumed where the electrofacies analysis is unavailable, with the corresponding permeability and porosity summarized in Table 5.1.

Finally the geomechanical parameters discussed in chapter 3 are used. In particular, the compressibility c_M of each layer is evaluated as a function of the actual effective stress, thus taking the pore pressure variation previously occurred within the producing volume into account.

Lithotype	Permeability k [m/s]	Porosity ϕ	ID number
sand	1.1×10^{-6}	0.25	1
silty sand	1.8×10^{-7}	0.18	2
clayey silt	2.6×10^{-9}	0.05	3
silty shale	1.8×10^{-10}	0.03	4

Table 5.2: Lithotype permeability and porosity used in the FE model of the litho-stratigraphic sequence in well 1. The ID number is the same as in Figure 5.1.

5.2.1 Well 1

The well's litho-stratigraphy is monitored by the EATT logging tool (see section 3.2.1) in the depth interval between 2700 and 3800 m. The stratigraphy is represented by means of 8 lithotypes, the main petrophysical properties of which are summarized in Figure 3.4. The lithotypes consist of 3 permeable sand formations, 3 silt-sand mixtures with intermediate features, and 2 low permeable shales. The litho-stratigraphic reproduction in the FE model is obtained by clustering the permeable and intermediate lithotypes into 2 classes (sandy and silty-sandy formations), whose properties are summarized in Table 5.2.

An example of the discretization used in the FE model to reproduce the litho-stratigraphy detected by electrofacies is shown in Figure 5.1. The main feature of well 1 is that thick sand units are confined by thin silty-clayey layers. The producing volumes are represented by the hatched areas of Figure 5.1, with the gas accumulation indicated by the light gray shaded areas in the leftmost column of Figure 5.1. The heterogeneity scale is usually smaller than the minimum Δz, so thin layers are incorporated into a thicker one by the homogenization procedure described in section 3.4. The FE mesh (see Figure 5.2) totalizes 362 layers, 101,360 elements, and 51,183 nodes, with an overall system size equating to 153,549.

In the depth interval between 2700 and 3800 m, 21 gas-bearing layers, indicated from here on by letters A to U, were recognized and developed over the last decade, with the in-situ deformation monitored by 28 marker spacings. The location of the depleted layers and radioactive markers is schematically shown in Figures 2.3(a) and 3.8, where the measured compactions and expansions during the monitored periods 1992-1996 and 1997-1999 are also represented. The static bottom hole pressure (SBHP) values for each producing layer were provided by ENI-Divisione Agip before starting the gas extraction (initial pressure) and at each marker logging time (1992, 1996, 1997 and 1999). The 1992 and 1996 marker surveys were performed with the aid of Schlumberger's FSMT tool, while in 1997 and 1999 the Western Atlas CMI tool was used. The static reservoir pressure values are summarized

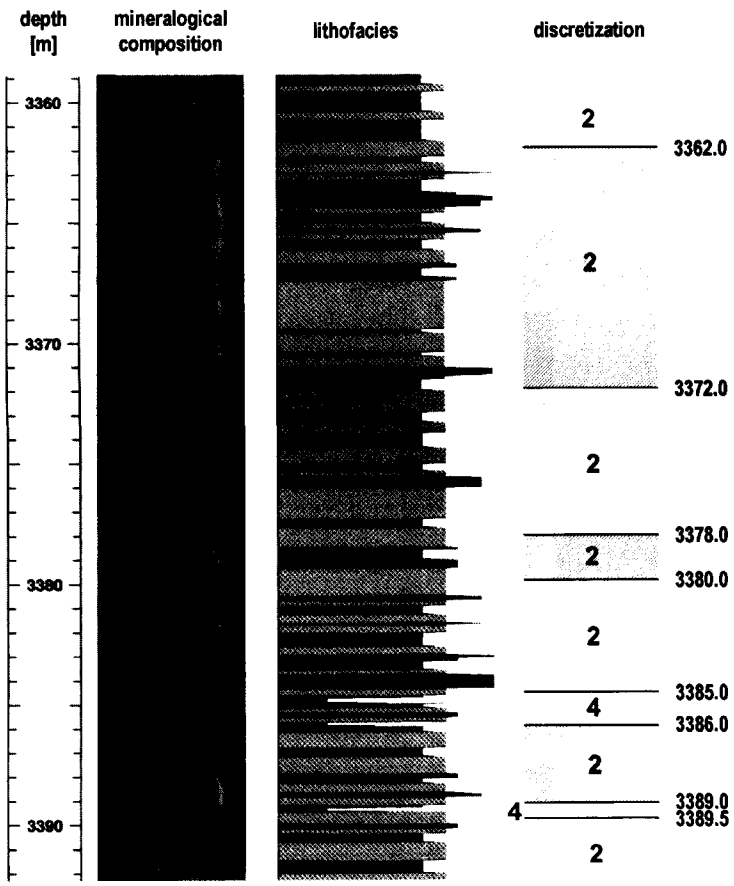

Figure 5.1: Stratigraphic discretization used in the FE model with the class ID number given in Table 5.2. Productive units are indicated by the dashed layers.

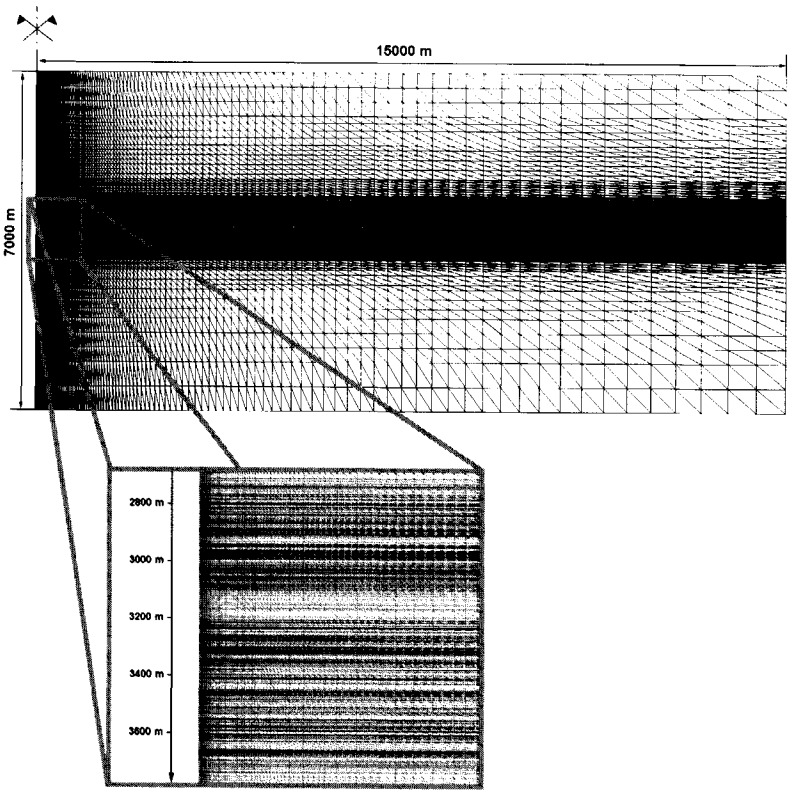

Figure 5.2: Cross-section of the FE mesh used to reproduce the in-situ deformations in well 1.

producing	static reservoir pressure (MPa)					Δp (MPa)	
layer	initial	1992	1996	1997	1999	92-96	97-99
A	30.8	29.0	28.0	22.3	17.8	-1.0	-4.5
B	32.0	32.0	22.3	19.1	31.5	-9.7	+12.4
C	32.9	32.9	32.9	24.3	31.5	0.0	+7.2
D	33.9	33.9	25.5	24.5	32.4	-8.4	+7.9
E	36.1	15.6	10.5	15.1	23.4	-5.1	+8.3
F	37.2	13.0	23.3	27.2	29.0	+10.3	+1.8
G	33.5	33.5	15.4	15.5	23.0	-18.1	+7.5
H	36.0	36.0	15.3	11.4	16.0	-20.7	+4.6
I	38.0	16.5	11.6	11.2	12.5	-4.9	+1.3
J	38.0	19.2	17.0	16.2	15.0	-2.2	-1.2
K	38.9	37.9	14.3	11.5	8.1	-23.6	-3.4
L	39.0	39.0	14.5	8.0	5.6	-24.5	-2.4
M	39.5	22.2	12.0	9.7	8.3	-10.2	-1.4
N	39.4	38.5	19.8	11.3	7.5	-18.7	-3.8
O	39.7	39.7	17.3	12.3	n.a.	-22.4	n.a.
P	41.3	41.3	8.0	20.6	35.0	-33.3	+14.4
Q	41.6	41.6	10.7	10.8	18.3	-30.9	+7.5
R	42.7	18.3	15.5	13.0	10.5	-2.8	-2.5
S	43.7	14.0	11.0	9.8	9.4	-3.0	-0.4
T	44.5	44.5	23.9	15.5	12.2	-20.6	-3.3
U	44.5	44.5	20.0	20.0	n.a.	-24.5	n.a.

Table 5.3: Static reservoir pore pressure values in well 1 before starting production and at each marker logging time. The pore pressure variations over the monitored periods are given in the far right-hand columns. n.a. = not available.

in Table 5.3. It should be noted that the SBHP values in 1999 for layers O and U are not available, many layers had already undergone a significant drop in pore pressure at the time of initial marker monitoring (1992), and several reservoirs exhibited a natural pore pressure recovery after their abandonment during the 1997-1999 period.

The geomechanical properties of the porous medium are defined by the constitutive laws (3.13) and (3.14). The effective stress σ_z of each element is calculated as [Terzaghi and Peck, 1967]:

$$\sigma_z(\bar{z}) = \hat{\sigma}_z(\bar{z}) + p(\bar{z}, t) \tag{5.1}$$

where $\hat{\sigma}_z$ is the total vertical stress, $\bar{z}$ the elemental gravity center depth, p the pore pressure, and t the time. The total vertical stress $\hat{\sigma}_z$ is obtained as:

$$\hat{\sigma}_z(\bar{z}) = \bar{z} \cdot obg(\bar{z}) \tag{5.2}$$

where $obg(\bar{z})$ is the overburden gradient function, which is defined by the statistical

interpretation of the results of a density log survey. This function was provided by ENI-Divisione Agip for well 1 as:

$$obg(\bar{z}) = 12218.174 \times 10^{-6}\bar{z}^{0.0766} \tag{5.3}$$

with $\bar{z}$ in [m] and $obg(\bar{z})$ in [MPa/m]. Using equations (5.2) and (5.3), and the SBHP values at the different times given in Table 5.3, enables an estimate of the effective stress σ_z of each layer with equation (5.1), and hence the uniaxial compressibility c_M with equation (3.13) – if Δp is negative and the effective stress is at least as large as the preconsolidation stress, or equation (3.14) – if Δp is positive or the initial effective stress is smaller than the preconsolidation stress.

Several simulation scenarios are addressed over the 1992-1996 and 1997-1999 periods to analyze the influence of the major sources of uncertainties. In particular, the variability of the following parameters was considered:

1. the permeability of clayey-silty units is often very difficult to measure. Moreover, gas accumulation in several layers suggests that there may be no hydraulic connection between the pools, so the permeability might reasonably be even considerably lower than the one provided by ENI-Divisione Agip (see Figure 3.4). Thus, the values of Table 5.2 referring to lithotypes 3 and 4 are reduced by a variable factor r_p up to 10^4, and the corresponding scenarios denoted by K0 ($r_p = 10^0$) to K4 ($r_p = 10^4$);

2. the radius R of the pumped porous volume is based on empirical considerations, and is consequently fairly uncertain. Bearing in mind the location of the monitoring well with respect to the producing wells in the real field, R is varied from 500 to 1000 m, with the corresponding scenarios denoted as R500 and R1000.

The FE model is solved with the aid of Bi-CGSTAB preconditioned with ILUT(ρ, τ). The user-controlled parameters ρ and τ are optimized for each scenario and in most cases equate 45 and 10^{-5}, respectively. The critical time step was found experimentally to be between 1 and 10 days in the 1992-1996 simulations, and between 10 and 20 days in the 1997-1999 simulations. The minimum time step was therefore set to 10 and 20 days, respectively, and then incremented as the simulation proceeded up to a maximum of 91.25 days, i.e. 3 months. Finally, the solver convergence was accelerated using a preliminary Least Square Log scaling technique, obtaining a quite efficient computer performance. A few representative convergence profiles, referring to different scenarios in both simulation periods with the minimum time step, are shown as an example in Figure 5.3.

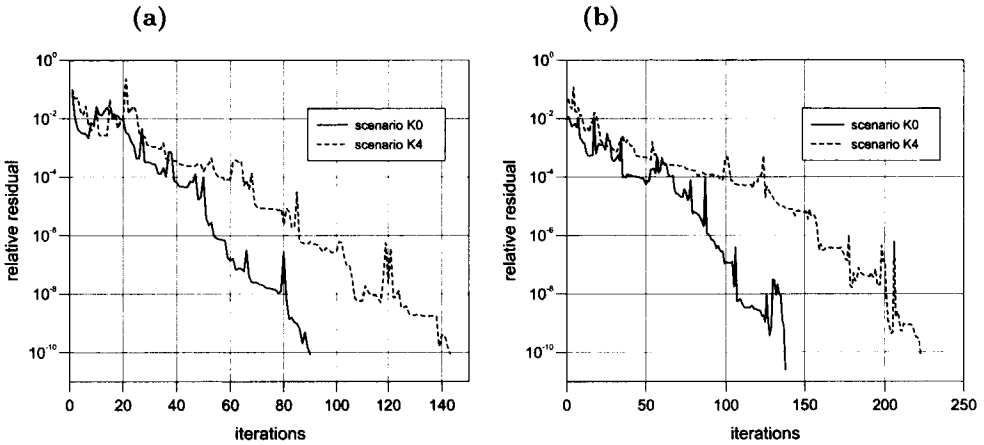

Figure 5.3: Well 1: representative convergence profiles obtained for: (a) $\Delta t = 10$ days, 1992-1996 simulation, and different scenarios; (b) $\Delta t = 20$ days, 1997-1999 simulation, and different scenarios.

First, the simulation over the time period 1992-1996 was performed. The most satisfactory results were obtained for $r_p = 10^4$ (scenario K4), i.e. with a negligible hydraulic communication between the productive units and the confining layers, as also shown by the in situ pore pressure measurements, and $R = 1000$ m (scenario R1000), i.e. with no important horizontal pore pressure gradients around the monitoring borehole. The comparison between the simulated marker response (eq. (4.20) vs depth) and the actual measurements recorded in the 1996 survey is shown in Figure 5.4. As predicted by the poromechanical analyses developed in the previous chapters, the model provides the compaction of the depleted layers and the expansion of the confining unproductive units. Figure 5.4 shows that the model can quite successfully reproduce not only most of the compacting spacings (e.g. spacings 5, 7, 8, 10, 12, 16, 17), but also the small expansions of markers incorporated into unproductive formations (spacings 1 and 13) and therefore unrelated to an increasing pore pressure. This provides evidence that the 1996 survey in well 1 generally supplied reliable deformation measurements, even where a few apparently anomalous data were encountered. The good match between simulation and measurements also validates the average behavior of the constitutive relationship (3.13), even though a few discrepancies can be found locally. For example, in the depth interval between 3650 and 3700 m – layers R and S, spacings from 21 to 26 – the rock compressibility appears to be slightly underestimated, since the simulated deformations are qualitatively similar to the measured deformations, but slightly smaller.

The simulation over the 1997-1999 time interval was done using the above calibrated r_p

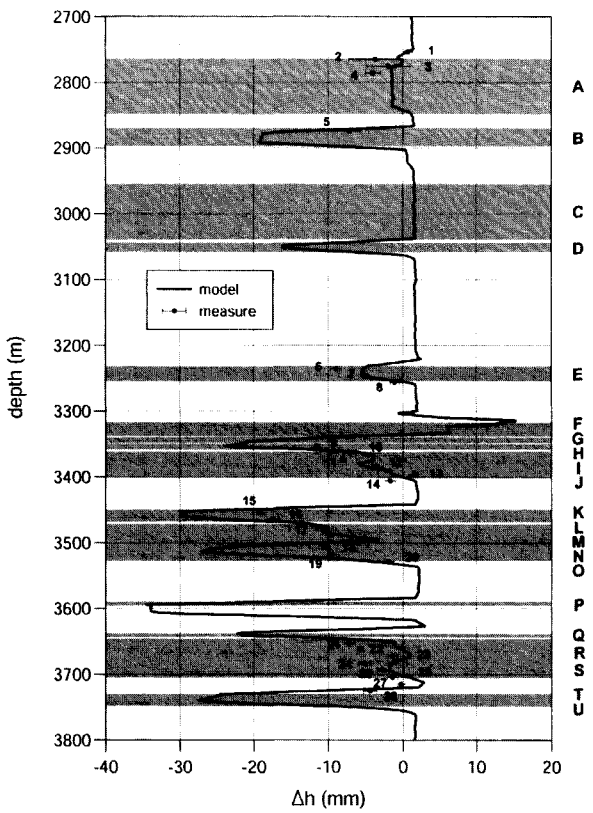

Figure 5.4: Well 1: comparison between the radioactive marker measurements and the model's results for the period 1992-1996.

and R values (10^4 and 1000 m, respectively). This period is characterized by the natural pore pressure recovery occurring in some of the depleted layers after they were abandoned. To address the mechanical hysteresis of the porous medium when the stress is reversed, the compressibility of recovering layers is calculated using the unloading-reloading constitutive law (3.14), with the loading c_M values divided by the average factor 2.2 [Baù *et al.*, 2002] with respect to the previous simulation. In layers O and U, where the static reservoir pressure values in 1999 are not available, a zero Δp is conventionally prescribed, but the unreliability of the simulated deformations in the vicinity of these layers should be kept in mind. Figure 5.5 shows the comparison between the actual marker measurements and the FE model's results. This comparison reveals a generally fairly good agreement, especially for spacings 5, 6, 7, 8, 9 and 12, which appear to be reliable for the estimate of a representative uniaxial compressibility in unloading-reloading conditions. Acceptable results are also obtained for compacting spacings incorporated into depleted layers, such as spacings 15, 17, 21 and 22, and – from a mainly qualitative viewpoint – also spacings 16 and 18. By contrast, spacings 2, 3 and 4 exhibit an anomalous behavior that cannot be accounted for by the model, since they expand although a pore pressure decrease of 4.5 MPa has supposedly occurred (see Table 5.3).

On the whole, the deformations measured by radioactive markers in the 1996 and 1999 surveys are reproduced fairly well by the FE model, despite a few discrepancies. This outcome shows that the marker implementation in well 1 is generally able to supply reliable measurements that can be used effectively to derive a constitutive relationship for c_M. In particular, the relationships (3.13) and (3.14) appear to be generally validated, with some possible local corrections to account for small quantitative differences.

5.2.2 Well 2

A detailed litho-stratigraphic sequence is available for well 2 in the depth interval between 900 and 1460 m. The log analysis is performed by means of the SHDT tool (see section 3.2.1), with the stratigraphical representation provided by 5 lithotypes, the properties of which are summarized in Figure 3.5. In the FE model of well 2, the low permeable shale formations are clustered into one class, thus obtaining the lithological classification given in Table 5.4.

Figure 5.6 shows an example of the discretization used in the FE model. While sand formations prevail over clays in the upper part of the borehole with a structure similar to the one encountered in well 1, in the lower part the stratigraphy is composed of alternating

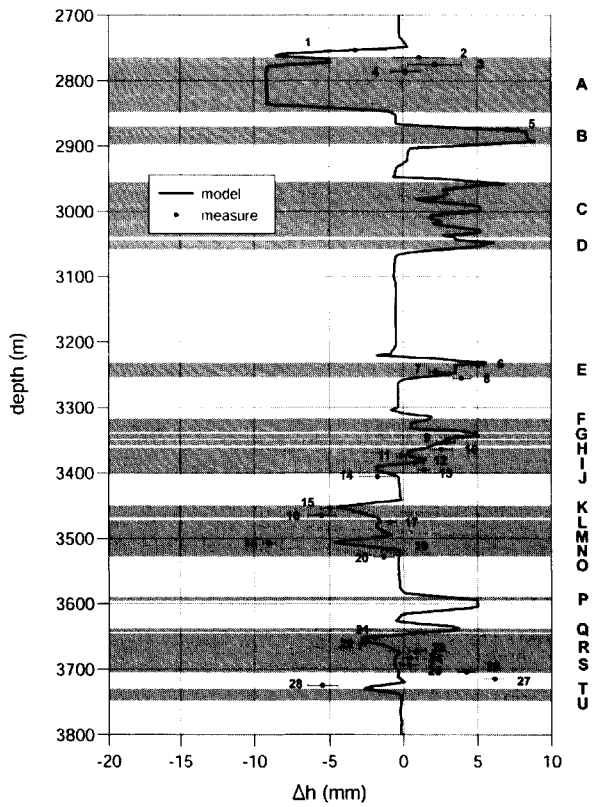

Figure 5.5: Well 1: the same as Figure 5.4 for the period 1997-1999.

Lithotype	Permeability k [m/s]	Porosity ϕ	ID number
unconsolidated sand	8.8×10^{-6}	0.27	1
silty sand	8.8×10^{-7}	0.24	2
silt	3.5×10^{-8}	0.06	3
shale	1.7×10^{-9}	0.06	4

Table 5.4: Lithotype permeability and porosity used in the FE model of the litho-stratigraphic sequence in well 2. The ID number is the same as in Figure 5.6.

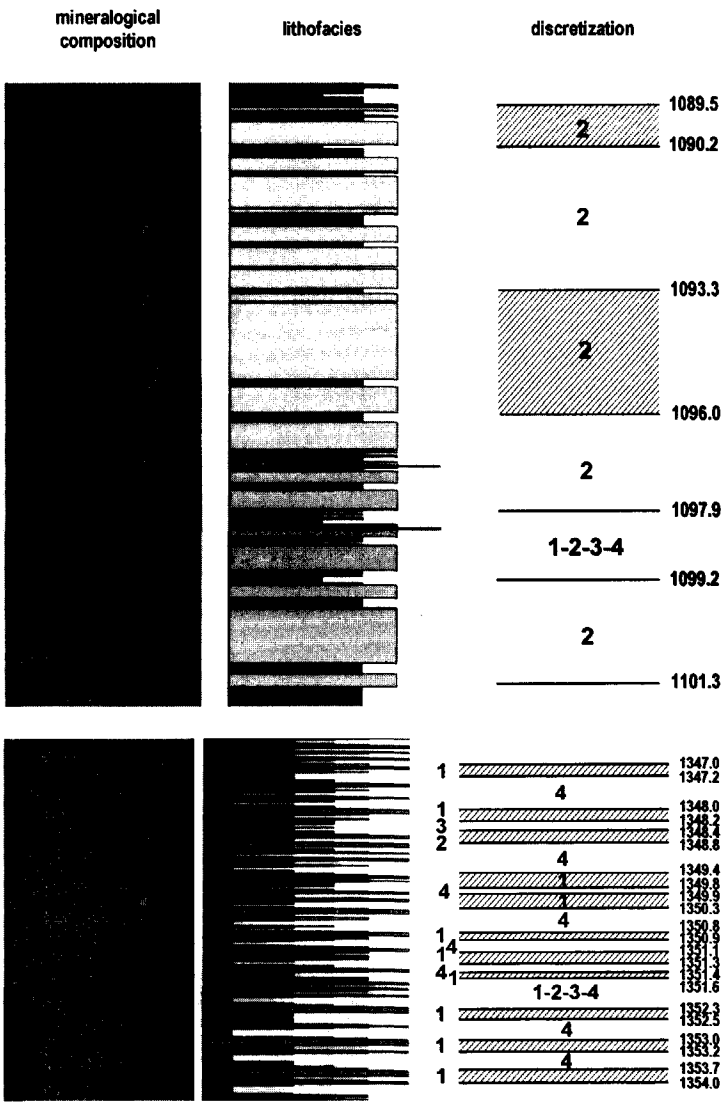

Figure 5.6: Stratigraphic discretization used in the FE model with the class ID number provided in Table 5.4. Productive units are indicated by the dashed layers.

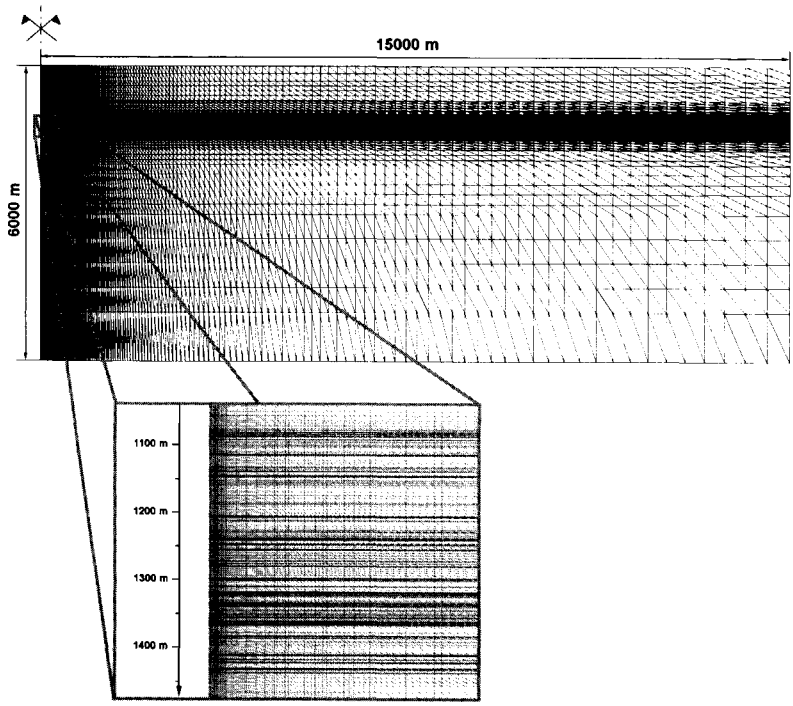

Figure 5.7: Cross-section of the FE mesh used to reproduce the in-situ deformations in well 2.

thin sandy, silty, and clayey horizons, which require a much higher FE resolution. The heterogeneity scale is quite often smaller than the minimum vertical spacing, i.e. 0.1 m, so the homogenization procedure of section 3.4 is used by necessity extensively in this case. The resulting FE mesh consists of 225 layers, 93,150 elements, and 47,008 nodes, with an overall system size of 141,024. The rigid basement of the model is set at a depth of 6000 m, since the depleted volumes are shallower than in well 1. A cross-section of the FE mesh is shown in Figure 5.7.

In the depth interval between 1050 and 1430 m, 17 gas-bearing layers were depleted in the period 1994-1996, and the corresponding deformations monitored by 30 marker spacings (see Table 2.2 and Figure 2.3(b)). The SBHP values are quite unreliable for 4 layers, so in the analysis that follows we consider 13 producing reservoirs and indicate them by the letters A to M. Available SBHP values are given in Table 5.5 at each marker logging time, together with the corresponding recorded variations. The 4 reservoirs without reliable pressure data are located between layers F and G. A conventional Δp of -1

producing layer	SBHP (MPa) 1994	1996	Δp (MPa) 94-96
A	7.9	7.3	-0.6
B	8.5	7.5	-1.0
C	8.2	7.6	-0.6
D	9.5	8.8	-0.7
E	9.1	8.6	-0.5
F	10.1	9.3	-0.8
G	12.8	12.5	-0.3
H	12.9	12.2	-0.7
I	10.5	9.5	-1.0
J	11.3	9.6	-1.7
K	10.5	9.5	-1.0
L	10.2	9.0	-1.2
M	9.4	8.2	-1.2

Table 5.5: Static reservoir pore pressure values in well 2 at each marker logging time. The pore pressure variations in the monitored period are given in the far right-hand column.

MPa is prescribed here, as derived from an indirect estimate provided by ENI-Divisione Agip. For well 2, both the 1994 and the 1996 surveys were completed using the FSMT logging tool.

The interpretation of the density log results by ENI-Divisione Agip provides the following relationship for the overburden gradient in well 2:

$$obg\,(\bar{z}) = 3270.771 \times 10^{-6} + 2415.588 \times 10^{-6} \ln \bar{z} \tag{5.4}$$

with again $\bar{z}$ in [m] and $obg\,(\bar{z})$ in [MPa/m]. Equation (5.4) and the SBHP values of Table 5.5 allow for the estimate of the effective stress using equation (5.1), and thus of the uniaxial compressibility of the lithology at depth $\bar{z}$.

Based on the results obtained for well 1, different scenarios are addressed by varying the shale permeability (scenario K0 to K4, the same as for well 1) and the radius R of the pumped volume. In this case, it should be borne in mind that the marker wellbore is also productive for layer A, so a line sink is used for this reservoir, while several scenarios are addressed for the other reservoirs with R between 100 and 1000 m.

Similarly to the FE model of well 1, the overall linear system was solved using Bi-CGSTAB preconditioned with ILUT(ρ, τ) and a preliminary Least Square Log scaling. The optimal values for ρ and τ turned out to be 45 and 10^{-4}, respectively, in most simulations. The critical time step was estimated experimentally between 1 and 10 days, so a minimum time step of 10 days was used. As the simulation proceeded, Δt was increased

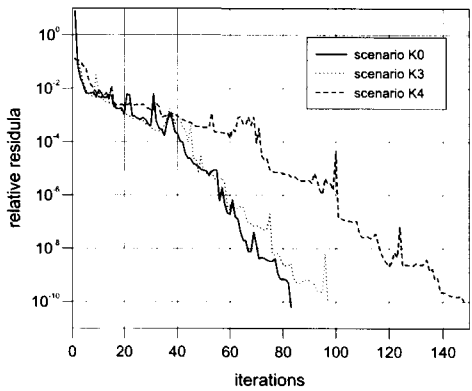

Figure 5.8: Well 2: representative convergence profiles obtained for $\Delta t = 10$ days and different scenarios.

up to 91.25 days. A few representative convergence profiles are shown in Figure 5.8 for $\Delta t = 10$ days and different scenarios. As predicted by theory [Ferronato *et al.*, 2001], the difficulty in solving the problem increases as the permeability decreases, i.e. in scenario K4 the convergence is slower than, for instance, in scenario K0 (Figure 5.8).

The scenario that best fits the measurements is obtained with $r_p = 10^4$, as in well 1, and $R = 100$ m for every producing layer, except layer A. This means that a somewhat appreciable horizontal pressure gradient is generated around the monitoring wellbore, especially in the vicinity of layer A. The comparison between the actual marker records and the FE results is shown in Figure 5.9. A qualitative consistency is found for the majority of the observations, the simulated deformations generally proving smaller than the measurements. A better reproduction is obtained, especially for spacings located in the upper part of the borehole, by locally doubling the uniaxial rock compressibility, as shown in Figure 5.10. This may imply that the constitutive relationship (3.13) could be underestimated for geological formations lying at a depth of about 1000 m.

Observing Figures 5.9 and 5.10 reveals that several compaction, and also expansion measurements are well reproduced by the FE model, e.g. for spacings 1, 2, 6, 7, 8, 10, 11, 22, 23, 24, 25, 26, 27 and 29, whereas the behavior of other markers appears difficult to simulate quantitatively, or even qualitatively. The spacings located within or close to layer A (no. 3, 4 and 5) exhibit a pronounced compaction relative to the quite small static pressure drop experienced by the formation. This might be explained by an unusually large local rock compressibility, or most likely the measurement's accuracy could be af-

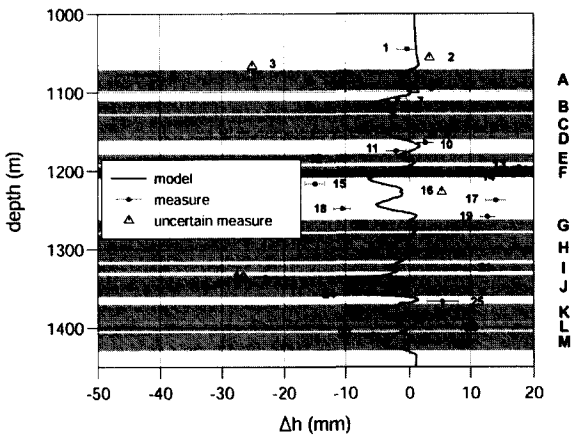

Figure 5.9: Well 2: comparison between radioactive marker measurements and the model's results computed using the compressibility law (3.13) for the period 1994-1996.

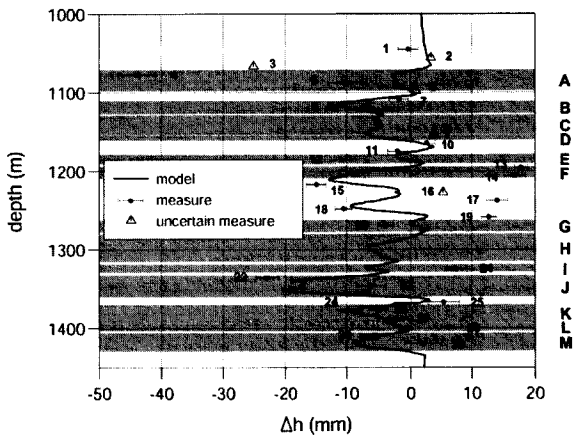

Figure 5.10: Well 2: the same as in Figure 5.9 locally doubling the compressibility provided by equation (3.13).

Lithotype	Permeability k [m/s]	Porosity ϕ	ID number
sand	5.5×10^{-6}	0.22	1
silty sand	5.5×10^{-7}	0.17	2
marny silt	3.7×10^{-9}	0.05	3
silty shale	3.7×10^{-10}	0.03	4

Table 5.6: Lithotype permeability and porosity used in the FE model of the litho-stratigraphic sequence in well 3. The ID number is the same as in Figure 5.11.

fected by the fluid production from this layer, thus causing a much higher local dynamic drop in pore pressure than the static value provided by ENI-Divisione Agip [Mobach and Gussinklo, 1994]. The behavior of spacings 13, 14 and 20 is rather difficult for the model to reproduce because of the uncertainty affecting the pore pressure data available for the producing layers located between layers F and G, as mentioned previously. Finally, the reliability of spacings 21, 28 and 30 appears to be dubious, since they exhibit an expansion despite being situated entirely within depleted layers. Obviously, the model cannot represent such measurements, which are most probably affected by some instrumental or operating errors. It is also worth noting that the more doubtful spacings lie in a litho-stratigraphic sequence characterized by a very marked heterogeneity (see Figure 5.6), which makes it quite difficult to locate the markers accurately relative to the productive and unproductive units and evaluate the actual pore pressure variation within the monitored depth interval. This type of configuration consequently appears to provide a limited contribution to the estimate of the porous medium compressibility.

5.2.3 Well 3

The litho-stratigraphy of well 3 was defined by using the EATT logging data in the depth interval between 2950 and 3350 m. Six lithotypes, summarized in Figure 3.6, were used to represent the detailed sequence, 3 being mainly permeable (sand and silty sand formations) and 3 mainly impermeable (silt and clay formations). In the FE discretization, the original lithotypes are clustered into 4 classes, consisting of 1 permeable sand, 2 intermediate mixtures (one where sand prevails over silt, and one the other way round), and 1 low permeable shale. The properties of these lithotypes are shown in Table 5.6.

An example of the discretization generated in the FE model is shown in Figure 5.11. Well 3 is characterized by thin gas-bearing formations incorporated into a mainly low permeable porous matrix. Here again, where the heterogeneity scale is too small, the homogenization procedure of section 3.4 is used to cluster thin adjacent layers into a

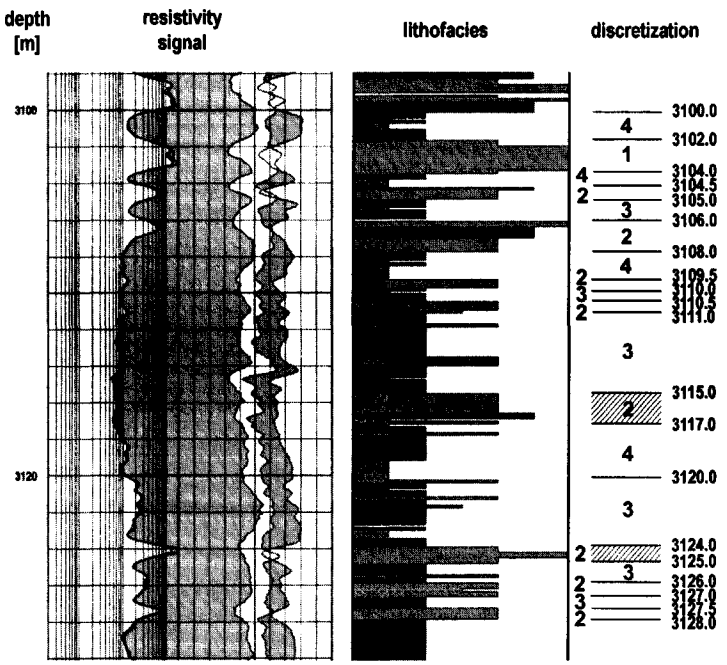

Figure 5.11: Stratigraphic discretization used in the FE model with the class ID number given in Table 5.6. Productive units are indicated by the dashed layers.

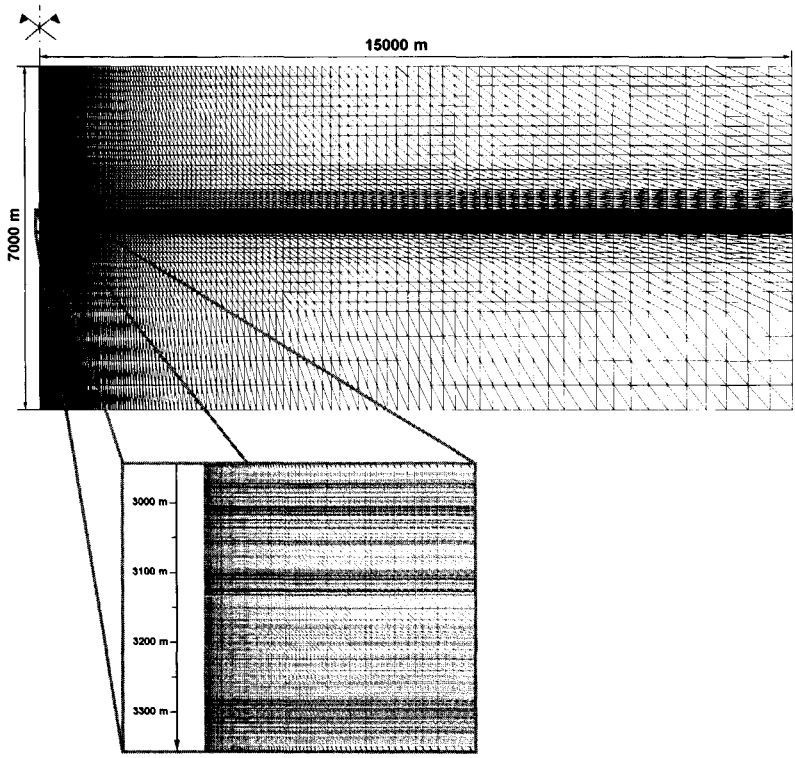

Figure 5.12: Cross-section of the FE mesh used to reproduce the in-situ deformations in well 3.

thicker unit with equivalent hydraulic properties. The FE mesh, shown in Figure 5.12, consists of 196 layers, 80,316 elements and 40,560 nodes, with an overall system size of 121,680.

Several gas-bearing layers were identified in the depth interval between 2950 and 3350 m, but only three reservoirs, indicated from here on by letters A, B and C, were depleted over the monitoring period 1996-1999. Twenty-three marker spacings were implemented in the above depth interval and the measurements, obtained in 1999 using the CMI logging tool, are given in Table 2.3 and graphically illustrated in Figure 2.3(c). Several operational problems occurred during the monitoring period in this well, however, and contributed to a much reduced efficiency of the radioactive marker technique:

1. a large proportion of the markers were displaced or even removed during the positioning of the well-casing because the radioactive bullets had not been shot deep

producing layer	SBHP (MPa) 1996	1999	Δp (MPa) 96-99
A	27.1	26.6	-0.5
B	34.7	29.6	-5.1
C	36.6	25.1	-11.5

Table 5.7: Static reservoir pore pressure values in well 3 at each marker logging time. The pore pressure variations in the monitored period are provided in the far right-hand column.

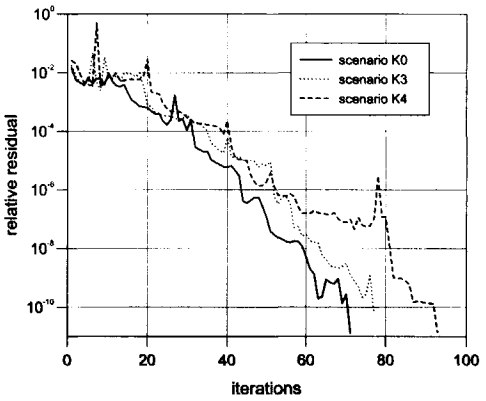

Figure 5.13: Well 3: representative convergence profiles obtained for $\Delta t = 20$ days and different scenarios.

enough into the formation. As a consequence, the length of several spacings does not correspond to the theoretical value of 10.5 m, but is sometimes larger (spacings 1, 2, 8, 10, 13, 22 and 23) or smaller (spacings 19, 20 and 21), as shown in Table 2.3 and Figure 2.3(c);

2. almost all the markers were installed in non-producing layers, owing to a later change in the field production plan. As a result, several spacings span depth intervals with no pore pressure drop and are therefore of no help for the c_M estimate.

The pore pressure variations available from the SBHP values provided for the producing layers by ENI-Divisione Agip are shown in Table 5.7.

The overburden gradient was estimated by ENI-Divisione Agip from a density log analysis. The function provided for well 3 is:

$$obg(\bar{z}) = 18877.801 \times 10^{-6} + 2.329 \times 10^{-6}\bar{z} + 9.112 \times 10^{-10}\bar{z}^2 + 2.206 \times 10^{-13}\bar{z}^3 \\ 2.043 \times 10^{-17}\bar{z}^4 \qquad (5.5)$$

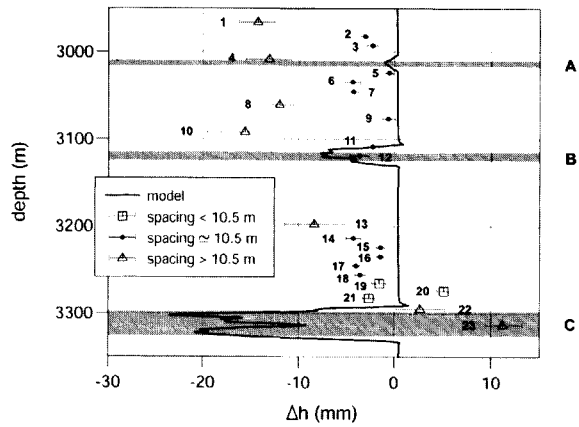

Figure 5.14: Well 3: comparison between the radioactive marker measurements and the model's results for the period 1996-1999.

with $\bar{z}$ and $obg(\bar{z})$ units as specified earlier. Using equation (5.5) gives the total and effective stress for each layer, and hence the corresponding geomechanical parameters given by the constitutive equation (3.13).

As in the previous cases, several simulations were carried out in the attempt to match the marker response recorded over the time interval 1996-1999. Values of r_p between 1 and 10^4 (scenario K0 through K4) and R up to 500 m (scenario R500) were used. In each simulation, the final linear system was solved using Bi-CGSTAB preconditioned with ILUT(ρ, τ) and a preliminary Least Square Log scaling. The optimal values for ρ and τ were 40 and 10^{-3}, respectively, in most simulations. The critical time step was usually less than 20 days, so a minimum Δt of 20 days was used, progressively increasing the value as the simulation proceeded up to a maximum of 91.25 days. The system solution proved to be quite efficient, with a few representative convergence profiles shown in Figure 5.13.

The results obtained with $r_p = 10^4$ and $R = 500$ m are compared with the marker records in Figures 5.14 and 5.15. This scenario was assumed as the most reliable on the basis of the experience gained from simulating wells 1 and 2, and because of the central location of the monitoring well with respect to the producing wells in the real field. Figures 5.14 and 5.15 show that the FE model can satisfactorily reproduce only a few spacings (no. 5, 9, 11 and 12) lying in or near the depleted layers A and B.

Figure 5.15 shows, in particular, the simulated deformation calculated considering the actual spacing length, which may differ from 10.5 m. The model's results reveal that the

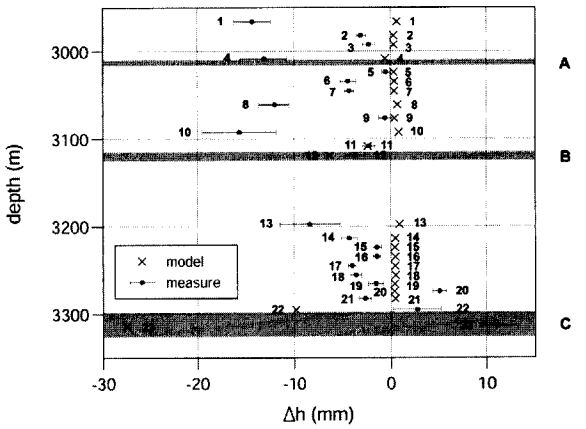

Figure 5.15: Well 3: the same as in Figure 5.14 with the model's results calculated with the effective spacing length.

discrepancy vis-à-vis the marker measurements is greater for spacings larger than 10.5 m. Surprisingly, these spacings recorded significant compactions despite zero pore pressure change, or significant expansions although they are incorporated within a depleted layer. The analysis performed in chapter 4 and the findings for wells 1 and 2 suggest that a small expansion should have occurred in the former case, and a pronounced compaction in the latter.

In conclusion, the results provided by the 1999 marker survey on well 3 are quite unreliable and offer no important contribution towards improving the estimation of the rock's mechanical properties, apart from the spacing 12. This is mainly due to operational problems encountered during the marker installation and to a minor extent to the litho-stratigraphy comprising thin productive units incorporated into a clayey porous matrix. It should be noted, however, that the calculation of c_M from spacing 12 alone provides a value that is in good agreement with the constitutive law (3.13) [Baù *et al.*, 2002].

5.3 Conclusions

The FE poroelastic coupled model developed in the previous chapters is used to interpret the radioactive marker measurements obtained over the last decade by ENI-Divisione Agip in three deep boreholes of the Northern Adriatic basin. The analysis is performed with the aid of high-resolution grids allowing for an accurate representation of the detailed

heterogeneous litho-stratigraphic sequences detected by electrofacies. The comparison between the deformations measured with the radioactive markers and the results from the FE model is drawn for several scenarios for each well, in order to take into account the uncertainty of the major factors affecting the process, such as the hydraulic conductivity of clay confining the depleted units and the possible occurrence of significant horizontal pore pressure gradients around the monitoring borehole.

The main results of the present analysis can be summarized as follows:

- on the whole, radioactive marker measurements appear to be adequately reproduced by a relatively simple (i.e. elastic, single phase, axi-symmetric) coupled FE model. This holds true not only for compacting spacings, but also for the markers indicating an expansion;

- the reproducibility of several measured marker data by the FE simulations is also an evidence of the reliability of the measurements. In particular, records to be effectively used for deriving representative rock compressibility values are more likely obtained in unproductive vertical boreholes where:

  - sandy lithotypes prevail over clayey formations;
  - the spacings monitored are entirely depleted;
  - two consecutive markers are initially about 10.5 m apart.

  The interpretation of marker data from installations that do not meet the above requirements may be uncertain and hence the corresponding measurements should be discarded from the compressibility estimate;

- the FE model used in the present analysis appears to be an efficient and robust tool for representing the actual deformations induced by the depletion of highly heterogeneous reservoirs. It could also be used for a preliminary analysis of expected deformations, and hence for a more effective placement of the radioactive markers.

Finally, calibration of the FE model has allowed for a validation of the constitutive laws (3.13) and (3.14) derived for the Northern Adriatic sediments. The reproduction of actual deformations in 3 boreholes suggests that the virgin loading and unloading-reloading compressibility used in the FE model appears to be quite realistic especially for a depth below 2500 m, while for a depth of about 1000 m c_M could be underestimated. The good reproduction of expansions due to the natural pore pressure recovery after the

field abandonment indicates a ratio between c_M in virgin loading and c_M in unloading-reloading conditions between 2 and 3.

Bibliography

AGIP (1996). Alto Adriatico: rapporto di sintesi. *Technical Report* (in Italian), Agip S.p.A., Milan.

Anelli, L., Mattavelli, L., and Pieri, M. (1996). Structural-stratigraphic evolution of Italy and its petroleum systems. In P. A. Ziegler and F. Horvath (Eds.), *Peri-Tethys Memoir 2: Structure and Prospects of Alpine Basins and Forelands*, vol. 170, pp. 455–483. Edition du Museum National d'Histoire Naturelle.

Baù, D., Gambolati, G., and Teatini, P. (1999). Statistical analysis of in-situ compaction measurements for anthropogenic land subsidence prediction in the Northern Adriatic basin. In A. Næss et al. (Eds.), *Proc. 5th Conf. Int. Ass. of Mathematical Geology*, vol. 1, Trondheim, pp. 299–304. Tapir Publ.

Baù, D., Gambolati, G., and Teatini, P. (2000a). Residual land subsidence near abandoned gas fields raises concern over Northern Adriatic coastland. *EOS, Trans. Am. Geophys. Union 81*, 245–249.

Baù, D., Gambolati, G., and Teatini, P. (2000b). Waterdrive dynamics and enhanced land subsidence over productive gas fields: application to Dosso degli Angeli reservoir, Ravenna, Italy. In D. Zhang, & C. L. Winter (Eds.), *Theory, Modeling, and Field Investigation in Hydrogeology: A Special Volume in Honor of Shlomo P. Neuman's 60th Birthday*, Boulder (CO), pp. 129–149. Geological Society of America Special Paper 348.

Baù, D., Ferronato, M., Gambolati, G., and Teatini, P. (2001). Local rock expansion in non-homogeneous productive gas/oil fields. In C. S. Desai et al. (Eds.), *Proc. 10th Conf. Int. Ass. of Computer Methods and Advances in Geomechanics*, vol. 2, Rotterdam, pp. 1295–1299. A. A. Balkema.

Baù, D., Ferronato, M., Gambolati, G., and Teatini, P. (2002). Basin-scale compressibility

of the Northern Adriatic by the radioactive marker technique. *Géotechnique 52*, 605–616.

Baù, D., Ferronato, M., Gambolati, G., and Teatini, P. (2003). Surface flow boundary conditions in modelling land subsidence due to fluid withdrawal. *Ground Water*. Submitted.

Bertoni, W., Brighenti, G., Gambolati, G., Ricceri, G., and Vuillermin, F. (1995). Land subsidence due to gas production in the off-shore natural gas fields of the Ravenna area, Italy. In F. B. J. Barends et al. (Eds.), *Land Subsidence (Proc. of the 5th Int. Symp. on Land Subsidence)*, Wallingford (UK), pp. 13–20. IAHS Publ. No. 234.

Bevilacqua, N., Cassiani, G., Macini, P., and Mesini, E. (1999). Compaction monitoring in Adriatic gas fields. In *Proc. 10th Int. Conf. on New Methods and Technologies in Petroleum Geology*, Krakow (Poland), pp. 103–112.

Biot, M. A. (1941). General theory of three-dimensional consolidation. *J. Appl. Phys. 12*, 155–164.

Bitelli, G., Bonsignore, F., and Unguendoli, M. (2000). Levelling and GPS networks to monitor ground subsidence in the Southern Po Valley. *J. Geodyn. 30*, 355–369.

Bondesan, M., Gatti, M., and Russo, P. (1997). Movimenti verticali del suolo della Pianura Padana orientale desumibili dai dati I.G.M. fino a tutto il 1990. *Boll. Geodesia e Scienze Affini 56*, 141-172 (in Italian).

Booker, J. R. and Small, J. C. (1975). An investigation of the stability of numerical solutions of Biot's equations of consolidation. *Int. J. Solids Struct. 11*, 907–917.

Brighenti, G., Macini, P., and Mesini, E. (2000). Reservoir compaction: a parametric study on in-situ measurements. In L. Carbognin et al. (Eds.), *Land Subsidence (Proc. 6th Int. Symp. on Land Subsidence)*, vol. 2, Padova, pp. 17–29. La Garangola.

Brignoli, M., and Figoni, A. (1995). Compattazione in Alto Adriatico: esame critico dei dati edometrici presenti in Agip. *Technical Report* (in Italian), Agip S.p.A., Milan.

Cassiani, G., and Zoccatelli, C. (2000). Towards a reconciliation between laboratory and in-situ measurements of soil and rock compressibility. In L. Carbognin et al. (Eds.), *Land Subsidence (Proc. 6th Int. Symp. on Land Subsidence)*, vol. 2, Padova, pp. 3–15. La Garangola.

Chan, S. K., Phoon, K. K., and Lee, F. H. (2001). A modified Jacobi preconditioner for solving ill-conditioned Biot's consolidation equations using symmetric quasi-minimal residual method. *Int. J. Numer. Analytic. Methods Geomech. 25*, 1001–1025.

Chierici, G. L., and Long, G. (1953). Compressibilité et masse spécifique des eaux de gisement dans les conditions du gisement: application à quelques problèmes de reservoir engineering. In *Proc. 5th World Petroleum Cong.* (in French), vol. 2, New York, pp. 187–210.

Chierici, G. L. (1989). *Principi di Ingegneria dei Giacimenti Petroliferi* (in Italian). Agip S.p.A., Milan.

Christian, J. T., and Boehmer, J. W. (1970). Plain strain consolidation by finite elements. *J. Soil Mech. and Found. Div. ASCE SM4*, 1435–1457.

Clayton, C. R. I., and Khatrush, S. A. (1986). A new device for measuring local axial strains on triaxial specimens. *Géotechnique 36*, 593–597.

Colazas, X. C., and Strehle, R. W. (1995). Subsidence in the Wilmington oil field, Long Beach, California, USA. In G. V. Chilingarian et al. (Eds.), *Subsidence Due to Fluid Withdrawal*, Developments in Petroleum Science 41, Amsterdam, pp. 285–334. Elsevier Science B.V.

Craig, R. F. (1974). *Soil Mechanics*. Spon, London.

Curtis, A. R., and Reid, J. K. (1972). On the automatic scaling of matrices for Gaussian elimination. *J. Inst. Math. Applic. 10*, 118–124.

De Kock, A. J., Johnson, J., Hagiwara, T., Zea, H. A., and Santa, F. (1998). Gulf of Mexico subsidence monitoring project with a new formation-compaction monitoring tool. *SPE Drill. Completion*, December, 223–230.

De Loos, J. M. (1973). In-situ compaction measurements in Groningen observation wells. *Verhandelingen Kon. Ned. Geol. Mijnbouwk. Gen. 28*, 79–104.

Desai, C. S. (1975). Analysis of consolidation by numerical methods. In *Proc. Symp. Recent Develop. Anal. Soil Behavior Appl. Geotech. Struct.*, Sydney, University of New South Wales.

Dondi, L., Rizzini, A., and Rossi, P. (1985). Recent geological evolution of the Adriatic Sea. In D. J. Stanley and F. C. Wezel (Eds.), *Geological Evolution of the Mediterranean Basin*, Berlin, New York, pp. 196–214. Springer-Verlag.

Doventon, J. H., and Prensky, S. E. (1992). Geological applications of wireline logs: a synopsis of developments and trends. *The Log Analyst 33*, 286–303.

Duff, I. S., Erisman, A. M., and Reid, J. K. (1986). *Direct Methods for Sparse Matrices*. Oxford University Press, Oxford.

Duff, I. S., and Meurant, G. A. (1989). The effect of orderings on preconditioned conjugate gradients. *BIT 29*, 635–659.

Ferronato, M., Gambolati, G., and Teatini, P. (1999). Total stress and pressure gradient formulations in coupled poroelasticity problems. In J. C. Roegiers et al. (Eds.), *Proc. Int. Symp. on Coupled Phenomena in Civil, Mining, and Petroleum Engineering*, vol. 1, Hainan (China), pp. 101–109.

Ferronato, M., Gambolati, G., and Teatini, P. (2001). Ill-conditioning of finite element poroelasticity equations. *Int. J. Solids Struct. 38*, 5995–6014.

Ferronato, M., Gambolati, G., Teatini, P., and Baù, D. (2003a). Radioactive marker measurements in heterogenous reservoirs: a numerical study. *Int. J. Geomech.*. In press.

Ferronato, M., Gambolati, G., Teatini, P., and Baù, D. (2003b). Interpretation of marker measurements of the Northern Adriatic gas fields. *SPE Reserv. Eval. Eng.*. Submitted.

Finol, A., and Sancevic, Z. A. (1995). Subsidence in Venezuela. In G. V. Chilingarian et al. (Eds.), *Subsidence Due to Fluid Withdrawal*, Developments in Petroleum Science 41, Amsterdam, pp. 337–372. Elsevier Science B.V.

Fredrich, J. T., Arguello, J. G., Deitrick, G. L., and de Rouffignac, E. P. (2000). Geomechanical modeling of reservoir compaction, surface subsidence, and casing damage at the Belridge diatomite field. *SPE Reserv. Eval. Eng. 3*, 348–359.

Gambolati, G., and Freeze, R. A. (1973). Mathematical simulation of the subsidence of Venice. 1. Theory. *Water Resour. Res. 9*, 721–733.

Gambolati, G., Gatto, P., and Freeze, R. A. (1974). Mathematical simulation of the subsidence of Venice. 2. Results. *Water Resour. Res. 10*, 563–577.

Gambolati, G., Ricceri, G., Bertoni, W., Brighenti, G., and Vuillermin, E. (1991). Mathematical simulation of the subsidence of Ravenna. *Water Resour. Res. 27*, 2899–2918.

Gambolati, G., Pini, G., and Putti, M. (1995). Conjugate gradient-like methods for the numerical solution of the two site model in sorbing porous media. In S. Atluri et al. (Eds.), *Computational Mechanics '95. Theory and Applications*, Berlin, New York, pp. 748–753. Springer-Verlag.

Gambolati, G., Putti M., and Paniconi, C. (1996). Projection methods for the finite element solution of the dual-porosity model in variably saturated porous media. In M. M. Aral (Ed.), *Advances in Groundwater Pollution Control and Remediation*, vol. 9 of NATO ASI Series 2: Environment, Dordrecht, pp. 97–125. Kluwer Academic.

Gambolati, G., Teatini, P., and Bertoni, W. (1998). Numerical prediction of land subsidence over Dosso degli Angeli gas field, Ravenna, Italy. In J. Borchers (Ed.), *Land Subsidence - current research and case studies. Proc. J. F. Poland Symp. on Land Subsidence*, Belmont (CA), pp. 229–238. Star Publ..

Gambolati, G., Teatini, P., Tomasi, L., and Gonella, M. (1999a). Coastline regression of the Romagna region, Italy, due to sea level rise and natural and anthropogenic land subsidence. *Water Resour. Res. 35*, 163–184.

Gambolati, G., Teatini, P., and Tomasi, L. (1999b). Stress-strain analysis in productive gas/oil reservoirs. *Int. J. Numer. Analytic. Methods Geomech. 23*, 1495–1519.

Gambolati, G., Teatini, P., Baù, D., and Ferronato, M. (2000). Importance of poro-elastic coupling in dynamically active aquifers of the Po river basin, Italy. *Water Resour. Res. 36*, 2443–2459.

Gambolati, G., Ferronato, M., Teatini, P., Deidda, R., and Lecca, G. (2001a). Finite element analysis of land subsidence above depleted reservoirs with pore pressure gradient and total stress formulations. *Int. J. Numer. Analytic. Methods Geomech. 25*, 307–327.

Gambolati, G., Pini, G., and Ferronato, M. (2001b). Numerical performance of projection methods in finite element consolidation models. *Int. J. Numer. Analytic. Methods Geomech. 25*, 1429–1447.

Gambolati, G., Pini, G., and Ferronato, M. (2002). Direct, partitioned and projected solution to finite element consolidation models. *Int. J. Numer. Analytic. Methods Geomech. 26*, 1371–1383.

Geertsma, J. (1966). Problems of rock mechanics in petroleum production engineering. In *Proc. 1st Cong. Int. Soc. of Rock Mechanics*, Lisbon, pp. 585–594.

Geertsma, J. (1973a). A basic theory of subsidence due to reservoir compaction: the homogeneous case. *Verhandelingen Kon. Ned. Geol. Mijnbouwk. Gen. 28*, 43–62.

Geertsma, J. (1973b). Land subsidence above compacting oil and gas reservoirs. *J. Petrol. Technol. 25*, 734–744.

Ghaboussi, J., and Wilson, E. L. (1973). Flow of compressible fluid in porous elastic media. *Int. J. Numer. Meth. Engng. 5*, 419–442.

Gutierrez, M., Lewis, R. W., and Masters, I. (2001). Petroleum reservoir simulation coupling fluid flow and geomechanics. *SPE Reser. Eval. Eng. 6*, 164–172.

Haan, E. A., and Arnott, R. J. (1991). The late Tertiary evolution of the Alpine system of the Mediterranean area. In A. M. Spencer (Ed.), *Generation, Accumulation and Production of Europe's Hydrocarbons*, Special Publication of the European Association of Petroleum Geoscientists No. 1, pp. 341–354. Oxford University Press.

Hald, A. (1952). *Statistical Theory with Engineering Applications*. J. Wiley, New York.

Heywood, C. (1995). Investigation of aquifer-system compaction in the Hueco basin, El Paso, Texas, USA. In F. B. J. Barends et al. (Eds.), *Land Subsidence (Proc. 5th Int. Symp. on Land Subsidence)*, Wallingford, pp. 35–45. IAHS Publ., No. 234.

Hsieh, P. A. (1996). Deformation induced changes in hydraulic head during groundwater withdrawal. *Ground Water 34*, 1082–1089.

HSL Archive (2000). *Aea Technology - Engineering Software*. CLRC.

Hueckel, T., Tao, F., Cassiani, G., and Pellegrino, A. (2000). Sediment compressibility evolving during aging: experiments and reactive plasticity model. In L. Carbognin et al. (Eds.), *Land Subsidence (Proc. 6th Int. Symp. on Land Subsidence)*, vol. 2, Padova, pp. 31–42. La Garangola.

Hueckel, T., Cassiani, G., Tao, F., Pellegrino, A., and Fioravante, V. (2001). Aging of oil/gas bearing sediments, their compressibility and subsidence. *J. Geotech. Geoenv. Eng. 127*, 926–938.

Huyakorn, P. S., and Pinder, G. F. (1983). *Computational Methods in Subsurface Flow*. Academic Press, New York.

Hwang, C. T., Morgenstern, N. R., and Murray, D. W. (1971). On solutions of plane strain consolidation problems by finite element methods. *Can. Geotech. 8*, 109–118.

Jacob, C. E. (1950). Flow of ground water. In *Engineering Hydraulics*, New York, pp. 321–386. J. Wiley.

Jardine, R. J., Symes, M. J., and Burland, J. B. (1984). The measurement of soil stiffness in triaxial apparatus. *Géotechnique 34*, 323–340.

Johnson, J. P., Rhett, D. W., and Slemers, W. T. (1989). Rock mechanics at the Ekofisk reservoir in the evaluation of subsidence. *J. Petrol. Technol. 41*, 717–722.

Kershaw, D. S. (1978). The incomplete Cholesky-conjugate gradient method for the iterative solution of systems of linear equations. *J. Comp. Phys. 26*, 43–65.

Kim, Y., Tatsuoka, F., and Ochi, K. (1994). Deformation characteristics at small strains of sedimentary soft rocks by triaxial compression tests. *Géotechnique 44*, 461–478.

Lanczos, C. (1952). Solution of systems of linear equations by minimized iterations. *J. Res. National Bureau of Standards 49*, 33–53.

Larson, K. J., Başağaoğlu, H., and Mariño, M. A. (2001). Prediction of optimal safe ground water yield and land subsidence in the Los Banos-Kettleman City area, California, using a calibrated numerical simulation model. *J. Hydrol. 242*, 79–102.

Lewis, R. W., and Schrefler, B. A. (1998). *The Finite Element Method in the Static and Dynamic Deformation and Consolidation of Porous Media* (2nd ed.). J. Wiley, Chichester.

Macini, P., and Mesini, E. (1998). Static and dynamic reservoir rock compressibility at high pressure. In *Proc. 8th Abu Dhabi Petroleum Conference*, pp. 813–820.

Macini, P., and Mesini, E. (2000). Compaction monitoring from radioactive marker technique. In L. Carbognin et al. (Eds.), *Land Subsidence (Proc. 6th Int. Symp. on Land Subsidence)*, vol. 2, Padova, pp. 43–55. La Garangola.

Marsala, A. F., Ragazzini, G., Meazza, O., Brignoli, M., and Santarelli, F. J. (1994). Basin scale rock mechanics: logs and core measurements. In *EUROCK '94, Rock Mechanics for Petroleum Engineering*, Rotterdam, pp. 105–112. A. A. Balkema.

Mattavelli, L., Ricchiuto, T., Grignani, D., and Schoell, M. (1983). Geochemistry and habitat of natural gases in Po basin, northern Italy. *Am. Assoc. Petr. Geol. B. 67*, 2239–2254.

Mattavelli, L., and Novelli, L. (1990). Geochemistry and habitat of the oils in Italy. *Am. Assoc. Petr. Geol. B. 74*, 1623–1639.

Mattavelli, L., Novelli, L., and Anelli, L. (1991). Occurrence of hydrocarbons in the Adriatic basin. In A. M. Spencer (Ed.), *Generation, Accumulation and Production of Europe's Hydrocarbons*, Special Publication of the European Association of Petroleum Geoscientists No. 1, pp. 369–380. Oxford University Press.

Meijerink, J. A., and van der Vorst, H. A. (1977). An iterative method for linear systems of which the coefficient matrix is a symmetric M-matrix. *Math. Comp. 31*, 148–162.

Menghini, M. L. (1989). Compaction monitoring in the Ekofisk area chalk fields. *J. Petrol. Technol. 41*, 735–739.

Mindlin, R. D., and Cheng, D. H. (1950). Thermoelastic stress in the semi-infinite solid. *J. Appl. Phys. 21*, 931–939.

Mobach, E., and Gussinklo, H. J. (1994). In-situ reservoir compaction monitoring in the Groningen field. In *EUROCK '94, Rock Mechanics for Petroleum Engineering*, Rotterdam, pp. 535–547. A. A. Balkema.

NAM (1995). Subsidence caused by natural gas production. *Technical Report*, Nam, Assen.

Palozzo, W., Cassiani, G., Brighenti, G., and Zoccatelli, C. (2000). Three-dimensional simulation of subsidence due to the gas production in the Barbara field and comparison with field data. In L. Carbognin et al. (Eds.), *Land Subsidence (Proc. 6th Int. Symp. on Land Subsidence)*, vol. 2, Padova, pp. 397–408. La Garangola.

Pao, W. K. S., Lewis, R. W., and Masters, I. (2001). A fully coupled hydro-thermo-poro-mechanical model for black oil reservoir simulation. *Int. J. Numer. Analytic. Methods Geomech. 25*, 1229–1256.

Papoulis, A. (1965). *Probability, Random Variables and Stochastic Processes.* McGraw-Hill, London.

Park, K. C. (1983). Stabilization for partitioned solution procedure for pore fluid-soil interaction analysis. *Int. J. Numer. Meth. Engng. 19*, 1669–1673.

Park, K. C., and Felippa, C. A. (1983). Partitioned analysis of coupled systems. In T. Belytschko and T. J. R. Hughes (Eds.), *Computational Methods for Transient Analysis*, Amsterdam, pp. 158 219. North-Holland.

Petroconsultants (1996). Petroleum exploration and production database. *Technical Report*, Petroconsultants Inc., Houston (TX).

Pini, G., Gambolati, G., and Ferronato, M. (2002). Direct and iterative methods in Finite Element consolidation models. In K. Kovar and Z. Hrkal (Eds.), *Proc. 4th Int. Conf. Calibration and Reliability in Groundwater Modelling*, vol. 1, Prague, pp. 101–104. Acta Universitatis Carolinae - Geologica 2002, 46 (2/3).

Pottgens, J. J. E., and Browner, F. J. J. (1991). Land subsidence due to gas extraction in the northern part of the Netherlands. In *Land Subsidence (Proc. of Houston Symposium)*, Pub. No. 200, pp. 99–108.

Prevost, J. H. (1998). Partitioned solution procedure for integration of coupled diffusion problems. In J. F. Thimus et al. (Eds.), *Poromechanics*, Rotterdam, pp. 129–133. A. A. Balkema.

Reed, M. B. (1984). An investigation of numerical errors in the analysis of consolidation by finite elements. *Int. J. Numer. Analytic. Methods Geomech. 8*, 243–257.

Ricceri, G., and Butterfield, R. (1974). An analysis of compressibility data from a deep borehole in Venice. *Géotechnique 24*, 175–192.

Ruddy, I., Andersen, M. A., Pattillo, P. D., Bishlawi, M., and Foged, N. (1989). Rock compressibility compaction and subsidence in a high-porosity chalk reservoir: a case study of Valhall Field. *J. Petrol. Technol. 41*, 741–746.

Ruistuen, H., Teufel, L. W., and Rhett, D. W. (1999). Influence of reservoir stress path on deformation and permeability of weakly cemented sandstone reservoirs. *SPE Reserv. Eval. Eng. 2*, 266–272.

Saad, Y. (1994). ILUT: a dual threshold incomplete ILU factorization. *Num. Lin. Alg. Appl. 1*, 387–402.

Saad, Y. (1996). *Iterative Methods for Sparse Linear Systems.* PWS Publishing, Boston.

Sandhu, R. S., and Wilson, E. L. (1969). Finite element analysis of seepage in elastic media. *J. Engng. Mech. ASCE 95*, 641–652.

Schlumberger (1974). Fluid conversion in production log interpretation. *Technical Report*, Schlumberger Inc., Houston (TX).

Schmitt, T. (1996). The measurement of the subsidence of geological formations with position sensitive detectors. Application to the oil fields. In *Proc. 5th European Union Hydrocarbon Symp.*, Edinburgh, pp. 1028–1061.

Serra, O., and Abbott, T. H. (1982) The contribution of logging data to sedimentary sedimentology and stratigraphy. *J. Soc. Petr. Eng. 22*, 117–131.

Sonneveld, P. (1989). CGS, a fast Lanczos-type solver for nonsymmetric linear systems. *SIAM J. Sci. Stat. Comp. 10*, 36–52.

Sloan, S. W., and Abbo, A. J. (1999). Biot consolidation analysis with automatic time stepping and error control. Part 1: theory and implementation. *Int. J. Numer. Analytic. Methods Geomech. 23*, 467–492.

Teatini, P., Baù, D., and Gambolati, G. (2000). Water-gas dynamics and coastal land subsidence over Chioggia Mare field, northern Adriatic Sea. *Hydrogeol. J. 8*, 462–479.

Terzaghi, K. (1925). *Erdbaumechanik auf Bodenphysikalischer Grundlage.* F. Deuticke, Wien.

Terzaghi, K., and Peck, R. B. (1967). *Soil Mechanics in Engineering Practice* (2nd ed.). J. Wiley, New York.

Tosi, L., Carbognin, L., Teatini, P., Rosselli, R., and Gasparetto Stori, G. (2000). The ISES project subsidence monitoring of the catchment basin south of the Venice lagoon. In L. Carbognin et al. (Eds.), *Land Subsidence (Proc. 6th Int. Symp. on Land Subsidence)*, vol. 2, Padova, pp. 113–126. La Garangola.

Van der Knaap, W. (1959). Nonlinear behavior of elastic porous media. *Pet. Trans. AIME 216*, 179–187.

Van der Vorst, H. A. (1992). Bi-CGSTAB: a fast and smoothly converging variant of Bi-CG for the solution of nonsymmetric linear systems. *SIAM J. Sci. Stat. Comput. 13*, 631–644.

Van Hasselt, J. P. (1992). Reservoir compaction and surface subsidence resulting from oil and gas production. *Geol. Mijnbow. 71*, 107–118.

Vermeer, P. A., and Verruijt, A. (1981). An accuracy condition for consolidation by finite elements. *Int. J. Numer. Analytic. Methods Geomech. 5*, 1–14.

Verruijt, A. (1969). Elastic storage of aquifers. In R. De Wiest (Ed.), *Flow Through Porous Media*, New York, pp. 331–376. Academic Press.

Verruijt, A. (1977). Generation and dissipation of pore water pressure. In G. Gudehus (Ed.), *Finite Elements in Geomechanics*, London, pp. 293–317. J. Wiley.

Verruijt, A., and Brinkgreve, R. B. J. (2000). Structural damage by uniform subsidence. In L. Carbognin et al. (Eds.), *Land Subsidence (Proc. 6th Int. Symp. on Land Subsidence)*, vol. 1, Padova, pp. 167–175. La Garangola.

Westlake, J. R. (1968). *Numerical Matrix Inversion and Solution of Linear Equations*. J. Wiley, New York.

Wolff, M., and Pelissier-Combescure, J. (1982). FACIOLOG: Automated electrofacies determination. In *Proc. 23rd Annual Logging Symp. Trans. Soc. Professional Well Log Analysts.*

Zaman, M. M., Abdulraheem, A., and Roegiers, J. C. (1995). Reservoir compaction and surface subsidence in the North Sea Ekofisk field. In G. V. Chilingarian et al. (Eds.), *Subsidence Due to Fluid Withdrawal*, Developments in Petroleum Science 41, Amsterdam, pp. 373–423. Elsevier Science B.V.

Zienkiewicz, O. C. (1971). *The Finite Element Method in Engineering Science*. Mc-Graw Hill, London.

Zienkiewicz, O. C., Gallagher, R. H., Oden, J. T., and Taylor, C. (1975). *Finite Elements in Fluids. Vol. I - Viscous Flow and Hydrodynamics*. J. Wiley, New York.

Zienkiewicz, O. C., Paul, D. K., and Chan, A. H. C. (1988). Unconditionally stable staggered solution procedure for soil-pore fluid interaction problems. *Int. J. Numer. Meth. Engng. 26*, 1039–1055.

Zienkiewicz, O. C., and Taylor, R. L. (1989). *The Finite Element Method* (4th ed.). McGraw Hill, London.

Zienkiewicz, O. C. (1991). *The Finite Element Method in Engineering Geoscience*. McGraw Hill, London.

Samenvatting (Summary in Dutch)

Een van de grootste moeilijkheden bij de nauwkeurige voorspelling van bodemdaling bij de onttrekking van vloeistoffen aan de ondergrond is de kwaliteit en de betrouwbaarheid van de geomechanische gegevens die gebruikt worden om het veld te beschrijven. Een fundamentele parameter voor de simulatie van de vervorming van het poreuze medium is de uniaxiale verticale compressibiliteit van het gesteente, die kan worden bepaald uit metingen van de compactie in situ, met behulp van de techniek van zwak radio-actieve meetpunten (kogels). Deze techniek wordt met succes gebruikt in diverse gasvelden over de gehele wereld, en is recent ook gebruikt door ENI-Divisione Agip, de Italiaanse nationale oliemaatschappij, met als doel een betrouwbare bepaling van de mechanische eigenschappen van het gesteente in het Noord-Adriatische bekken. De gebruikelijke interpretatie van de meetresultaten in dit gebied leidt echter soms tot moeilijkheden, vanwege onverwachte verschijnselen, zoals expansie in plaats van compactie, of deformaties op plaatsen waar geen drukverandering is geconstateerd.

In deze studie worden de deformaties van het gesteente bestudeerd op de schaal van de meetpunten, bij de onttrekking van gas aan reservoirs in heterogene poreuze media, om daaruit aanwijzingen te verkrijgen voor een betere interpretatie van de resultaten van de metingen van de deformaties van de meetpunten. Bij de studie is gebruik gemaakt van een nieuw ontwikkeld model voor de gekoppelde consolidatie, dat is de deformatie van het gesteente, gekoppeld met de stroming door het poreuze medium.

Hoofdstuk 1 bevat enige nieuwe resultaten betreffende de numerieke aspecten van de ontwikkeling van een snel, nauwkeurig en robuust wiskundig model. Bijzondere aandacht wordt besteed aan de mogelijke slechte conditionering van het stelsel van vergelijkingen na de integratie in de tijd, en aan de toepasbaarheid van efficiente iteratieve oplosmethodes van het probleem.

De methode der eindige elementen is gebruikt om de te verwachten respons van de meetpunten te simuleren, voor het geval van de geologische en geomechanische omgeving van het Noord-Adriatische bekken. De techniek van het gebruik van radio-actieve

meetpunten wordt in Hoofdstuk 2 in detail beschreven. Daarbij worden ook enige van de onverwachte meetgegevens in verschillende boorgaten in dit gebied gepresenteerd. Met behulp van analytische oplossingen kan in dat stadium al enig inzicht worden verkregen in de mechanismen van vervorming in het reservoir en het omringende medium.

In Hoofdstuk 3 wordt een gedetailleerde beschrijving gegeven van de belangrijkste geologische, mechanische en hydraulische eigenschappen van het gesteente in het Noord-Adriatische bekken. Daarbij wordt ook een constitutief model gepresenteerd voor de uniaxiale compressie, zowel voor maagdelijke belasting als voor ontlasten en herbelasten.

De numerieke studie wordt gepresenteerd in Hoofdstuk 4 en 5. Het eindige-elementen-model wordt eerst gebruikt voor de simulatie van de verticale vervormingen geregistreerd door een ideaal paar van meetpunten in een realistisch homogeen medium. Dit deel van de studie geeft aanwijzingen over de belangrijkste factoren die de respons van het meetsysteem bepalen, de vormen van gelaagdheid die de meest geschikte gegevens opleveren, en de betrouwbaarheid van de uit de meetgegevens afgeleide waarden van de compressibiliteit. Vervolgens worden de meetresultaten gevonden bij drie diepe boorgaten in het Noord-Adriatische bekken numeriek gesimuleerd. Het blijkt dat het model diverse metingen bevredigend kan simuleren, en dat er nuttige suggesties worden verkregen voor een efficientere installatie van de meetpunten. De uitkomsten ondersteunen ook de toepasbaarheid van het voorgestelde constitutieve model voor de samendrukking van het gesteente.

M. Ferronato, Rock Expansion and Compaction at the Marker Scale in Gas Producing Reservoirs, PhD Thesis, Delft University of Technology, 2003.

Sommario (Summary in Italian)

Una delle maggiori difficoltà nella stima della subsidenza antropica dovuta all'estrazione di fluidi dal sottosuolo è legata al grado di affidabilità dei parametri geomeccanici utilizzati per la caratterizzazione dell'area di studio. Una proprietà del mezzo poroso di fondamentale importanza è la compressibilità verticale a deformazione laterale impedita, che può essere valutata mediante il monitoraggio con la tecnica dei marker radioattivi della compattazione in sito di giacimenti in fase di sviluppo. Utilizzata con successo in numerosi campi a gas nel mondo, la tecnica dei marker radioattivi è stata recentemente applicata da ENI-Divisione Agip, la compagnia petrolifera nazionale italiana, nel bacino dell'Alto Adriatico, per ottenere una stima più attendibile delle proprietà meccaniche delle rocce nel sottosuolo. Il risultato delle campagne di misura effettuate in Alto Adriatico, tuttavia, non ha consentito in diverse occasioni un'interpretazione immediata del dato, a causa dell'inatteso comportamento di alcuni marker che hanno rilevato espansioni anziché compattazioni, oppure delle deformazioni nonostante non fosse stata misurata alcuna variazione di pressione.

Il presente lavoro intende studiare le deformazioni locali delle rocce del sottosuolo indotte dal depletamento di giacimenti a gas situati in mezzi porosi eterogenei, al fine di consentire una più corretta interpretazione delle misure fornite dai marker radioattivi. L'analisi viene svolta utilizzando un modello ad elementi finiti sviluppato "ad hoc" per la simulazione della consolidazione accoppiata in mezzi porosi.

Il Capitolo 1 descrive alcuni risultati innovativi ottenuti in relazione agli aspetti numerici del problema, con l'obietttivo di sviluppare uno strumento matematico computazionalmente veloce, accurato e robusto. Particolare attenzione è stata rivolta allo studio del mal-condizionamento generato dall'integrazione nel tempo delle equazioni differenziali della consolidazione, e all'applicazione di schemi iterativi per la soluzione del sistema lineare risultante.

Il modello ad elementi finiti è stato adottato per simulare le misure di deformazione attese dai marker radioattivi nella configurazione geologica e geomeccanica tipica del bacino

dell'Alto Adriatico. Il Capitolo 2 analizza nel dettaglio la tecnologia dei marker radioattivi e l'uso delle deformazioni da essi fornite per la stima delle proprietà meccaniche del sottosuolo, presentando anche diverse misure inattese ottenute in alcuni pozzi di monitoraggio perforati in Alto Adriatico. In questo stadio preliminare sono state utilizzate soluzioni analitiche classiche per ricavare una prima indicazione sui principali meccanismi di deformazione che si sviluppano in giacimenti in fase di produzione e nel mezzo poroso circostante. Il Capitolo 3 offre una descrizione dettagliata ed aggiornata delle principali caratteristiche geologiche, meccaniche ed idrauliche del bacino dell'Alto Adriatico. In particolare è stata derivata una legge costitutiva originale per la compressibilità verticale su scala di bacino, in condizioni sia di primo che di secondo ciclo di carico.

Lo studio numerico è sviluppato nei Capitoli 4 e 5. Il modello ad elementi finiti viene prima utilizzato per simulare la deformazione verticale registrata da un'ideale coppia di marker radioattivi installati in una successione litologica realistica. Questa analisi fornisce indicazioni sui principali fattori in grado di condizionare la rilevazione dei marker, sulle configurazioni geologiche più favorevoli alla produzione di dati attendibili e sull'affidabilità teorica delle deformazioni misurate dai marker per la stima della compressibilità verticale. In seguito, viene simulato numericamente il comportamento registrato dai marker radioattivi collocati in tre pozzi di monitoraggio in Alto Adriatico. Si dimostra che il modello risulta in grado di riprodurre in modo soddisfacente diverse misurazioni, fornendo quindi indicazioni utili per una più efficiente installazione dei marker e confermando l'attendibilità della legge costitutiva su scala di bacino elaborata per l'area di interesse.

M. Ferronato, Rock Expansion and Compaction at the Marker Scale in Gas Producing Reservoirs, PhD Thesis, Delft University of Technology, 2003.

Curriculum Vitae

September 15, 1973 :	Born in Camposampiero (PD), Italy
1992 :	Secondary school diploma (Maturità scientifica) at the Liceo Scientifico "Tito Lucrezio Caro", Cittadella (PD), Italy
1998 :	Degree in Civil Engineering (Laurea) at the Università degli Studi di Padova, Italy
1998 - 2000 :	Consultant at MED Ingegneria Srl, Ferrara, Italy, and scholarship at the Department of Mathematical Methods and Models for Scientific Applications of the University of Padova
2000 - 2003 :	PhD student at Delft University of Technology

ISBN 90-407-2392-3